

UNIVERSITÀ DEGLI STUDI DI GENOVA

SCUOLA POLITECNICA

DIME

Dipartimento di Ingegneria Meccanica, Energetica,
Gestionale e dei Trasporti



MASTER OF SCIENCE THESIS
IN
MECHANICAL ENGINEERING

**Homogenization of the mass transport across thin
porous membranes: from small to large Péclet
numbers**

Supervisors:

Prof. Ing. Alessandro Bottaro

Dr. Giuseppe Antonio Zampogna

Prof. François Gallaire

Candidate:

Alberto Ponte

March 2023

Acknowledgments

Ringrazio il Prof. Bottaro per avermi permesso di fare questa magnifica esperienza, per avermi aiutato ogni volta che ne avevo bisogno e per avermi trasmesso la passione della fluidodinamica. Ringrazio il Dr. Zampogna per avermi seguito quotidianamente nel progetto con infinita pazienza, nonostante i suoi numerosi impegni, trasmettendomi l'interesse per l'argomento. Ringrazio il Prof. Gallaire, che mi ha dato la possibilità di lavorare nel suo laboratorio con grande cortesia e disponibilità. Un ringraziamento a tutti i membri del laboratorio, che mi hanno accolto amichevolmente e mi hanno sempre parlato in amicizia, sempre disponibili ad aiutare nonostante i miei silenzi. In particolare ringrazio Kevin, che mi ha supportato ogni volta che ne avevo bisogno. La sua amicizia mi ha aiutato a superare le parti più difficili del progetto. Ringrazio Simeon, che è riuscito a strapparmi un sorriso anche nei momenti più duri. Spero che senza di me a distrarlo possa lavorare tranquillo.

Ringrazio i miei genitori Marco e Flavia e mia sorella Alessandra. Ringrazio mio cugino Emilio, mia cugina Clara, mia zia Roberta e mio nonno Dino. Ringrazio i miei amici più stretti, Emanuele, Samuele e Lorenzo, che sono venuti a trovarmi. Spero di non perderli mai di vista.

Ringrazio i miei amici e coinquilini Giacomo e Edoardo. Vivere con loro è stato bellissimo e ha alleviato le fatiche della vita.

Ringrazio i membri della famiglia che non ci sono più, ma che sono stati indispensabili per quello che sono oggi e che sono sicuro mi sarebbero stati vicini. Ringrazio lo zio Gino, la zia Livia, la nonna Angela e la nonna Tina.

Omogeneizzazione del trasporto di massa attraverso membrane porose sottili: da piccoli a grandi numeri di Péclet

Sommario

Il trasporto di specie chimiche attraverso membrane porose a numeri di Péclet finiti è essenziale in molti fenomeni naturali e applicazioni industriali. In questo lavoro è stato sviluppato un modello basato sull'omogeneizzazione per descrivere il trasporto passivo di soluti attraverso membrane sottili microstrutturate nel caso di numeri di Péclet non trascurabili. L'accoppiamento asintotico tra il campo di concentrazione microscopico e macroscopico porta a un modello che afferma l'esistenza di un salto nel flusso di soluto attraverso la membrana, quantificato via dei coefficienti effettivi ottenuti dalla soluzione di problemi convettivi microscopici linearizzati. Tre diverse strategie di linearizzazione sono state confrontate. Nella strategia A, viene eseguita una approssimazione di Oseen della velocità avveviva. Nella strategia B, viene costruito un campo avvevivo microscopico partendo dagli sforzi del solvente alla membrana macroscopica. Nel terzo approccio (strategia C) la strategia B viene semplificata conservando solo alcune componenti degli sforzi del solvente. Queste strategie sono state testate per diverse configurazioni macroscopiche di flusso, portando alla conclusione che le strategie B e C riproducono in modo realistico la fisica, mentre il termine di Oseen usato nella strategia A produce un'approssimazione grossolana del campo di concentrazione del soluto alla membrana.

Homogenization of the mass transport across thin porous membranes: from small to large Péclet numbers

Abstract

The transport of chemical species through porous membranes at finite Péclet numbers is essential in many natural and industrial situations. In the present work, we develop a homogenization-based model to describe the passive transport of solutes across thin micro-structured membranes in the case of non-negligible Péclet numbers. The asymptotic matching between the microscopic and macroscopic solute concentration fields leads to a solute flux jump across the membrane, quantified through effective coefficients retrieved from the solution of linearised advection-diffusion problems at the microscale. Three different linearisation strategies are compared. In strategy A, we exploit an Oseen approximation of the advective velocity. In strategy B, we build a microscopic advective field starting from the solvent stresses at the macroscopic membrane. In the third approach (strategy C) we simplify strategy B by retaining only a few solvent stress components. These strategies are tested under different macroscopic flow conditions, leading to the conclusion that strategies B and C well reproduce the full-scale physics while the Oseen term exploited in strategy A produces a poor approximation of the solute concentration field at the membrane.

Contents

1	Introduction	1
2	Homogenization-Based Mathematical Model	4
2.1	Homogenization Procedure	5
2.1.1	Outer Problem	6
2.1.2	Inner Problem	7
2.1.3	Matching Conditions	7
2.1.4	Multiple Scale Expansion	8
2.2	Microscopic Problem	10
2.3	Macroscopic Problem	11
2.3.1	Strategy A: advection via an Oseen linearization	12
2.3.2	Strategy B: advection via a microscopic velocity retrieved from the macroscopic stresses along the membrane.	12
2.3.3	Strategy C: advection via a simplified velocity field	12
3	Flow past a planar membrane	14
3.1	Solution of the Microscopic Problems	14
3.1.1	Effective diffusion vectors T and Y : strategy A	16
3.1.2	Effective diffusion vectors T and Y : strategy B	16
3.1.3	Effective diffusion vectors T and Y : strategy C	18
3.1.4	Comparison between the strategies	19
3.2	Solution of the macroscopic configuration	21
3.2.1	Diffusive case	24
3.2.2	Case $Pe^{\text{O}} = \frac{1}{\varepsilon}$	25
3.2.3	Case $Pe^{\text{O}} = \frac{1}{\varepsilon^2}$	26
3.2.4	Case $Pe^{\text{O}} = \frac{2.5}{\varepsilon^2}$ case	27
3.2.5	Case $Pe^{\text{O}} = \frac{5}{\varepsilon^2}$	28
3.2.6	Case $Pe^{\text{O}} = \frac{10}{\varepsilon^2}$	29
3.2.7	Further insights on Pe^{I}	30
3.3	Testing other values of the separation of scales parameter	33
3.3.1	Case $\varepsilon = 0.1$	33
3.3.2	Case $\varepsilon = 0.01$	36
3.3.3	Effect of Re^{O} on Pe^{I}	38
4	Flow past a cylindrical membrane	41
4.1	Accounting for discontinuities at the membrane	41
4.2	Microscopic solution	42
4.2.1	Effective diffusion vectors	44
4.3	Solution of the Macroscopic Problem	45
4.3.1	Diffusive Case	49
4.3.2	Case $Pe^{\text{O}} = \frac{1}{\varepsilon^2}$	50
4.3.3	Case $Pe^{\text{O}} = \frac{1}{\varepsilon^3}$	51
4.3.4	$Pe = 1000$ case	52

4.3.5	Case $Pe^{\text{0}} = 2000$	53
4.3.6	Case $Pe^{\text{0}} = \frac{1}{\varepsilon^4}$	54
4.3.7	Variations of Pe^{I} with Pe^{0}	55
5	Conclusions	56
	References	57
A	Numerical solution	59
B	Numerical convergence	59

1 Introduction

Mass transport across porous membranes is massively exploited in industry [1]. These flows are involved in a wide range of industrial processes, like filtration, desalinization, drug delivery, and fog harvesting for clean water production [2, 3, 4]. Separation processes constitute the 10-15% of the world energy consumption and their accurate modelling is fundamental [5, 6].

The complexity of fluid porous structure interactions resides in the presence of two different length scales at play: the microscopic size of the membrane pores and the macroscopic size of the membrane itself. A multi-scale approach is necessary to analyse these phenomena, where the two length scales are treated in an unified framework. An example of multiscale approaches are volume averaging [7, 8] and homogenization methods [9, 10], where global membrane properties are obtained from the microscopic behaviour, and then used in a macroscopic model which provide an upscaled description of the full-scale physics.

A model to describe the transport of chemical species dissolved in an incompressible flow across thin permeable membranes for small Péclet numbers has been developed via homogenization in [11].

In this work, the full-scale membrane is replaced by an equivalent smooth surface, where the solvent velocity and the solute concentration are imposed via a solvent stress and solute flux jump condition. The model is validated via comparisons against direct numerical simulations of the full-scale flow. The model is developed under the assumption of negligible advection within the membrane pores.

Among the others, advection is important in the mixing of chemical species in microchannels (cf. figure 1.1 for an example).

In [12] it has been shown that the minimal mixing length to obtain a well-mixed solution for a mixture of water (20%), glycerol (80%) and fluorescein, is of the order of several centimeters and, hence, prohibitive for microfluidics channels. Two non dimensional parameters are defined to describe the solvent and solute behaviour. The Reynolds number represents the ratio of inertial to viscous solvent forces

$$Re = \frac{\rho U l}{\mu} , \tag{1.1}$$

where ρ , μ , U are respectively the solvent density, dynamic viscosity and velocity. The quantity denoted by l is the characteristic length of the problem considered, i.e. the channel height.

The other parameter is the Péclet number. It defines how chemical species are transported by the solvent. The Péclet number is defined as the ratio of the rate of advection to the rate of diffusion, i.e.

$$Pe = \frac{U l}{D} . \tag{1.2}$$

In microfluidics applications this parameter is usually large. In [12] the Reynolds number is relatively low ($Re < 100$). This leads to a laminar and uniaxial flow, where the diffusion between the streamlines is slow. The Péclet number is instead quite large ($Pe \gg 100$). The mixing length is defined as the distance from the inlet of the channel where the solution is mixed at the 90%. The degree of mixing is defined as the standard deviation of the solute concentration as

$$\sigma = \langle (c_1 - \langle c_1 \rangle)^2 \rangle^{\frac{1}{2}} . \quad (1.3)$$

A value $\sigma = 0$ corresponds to full mixing (cf. inset (C) in figure 1.1), while $\sigma = 0.5$ to a sharp separation between solute and solvent (cf. inset (A) in figure 1.1). In [12] the authors have shown that in the case of smooth channel walls, the mixing length grows linearly with Péclet, while if the wall of the channel is modified introducing some microscopic roughness the mixing length is reduced.

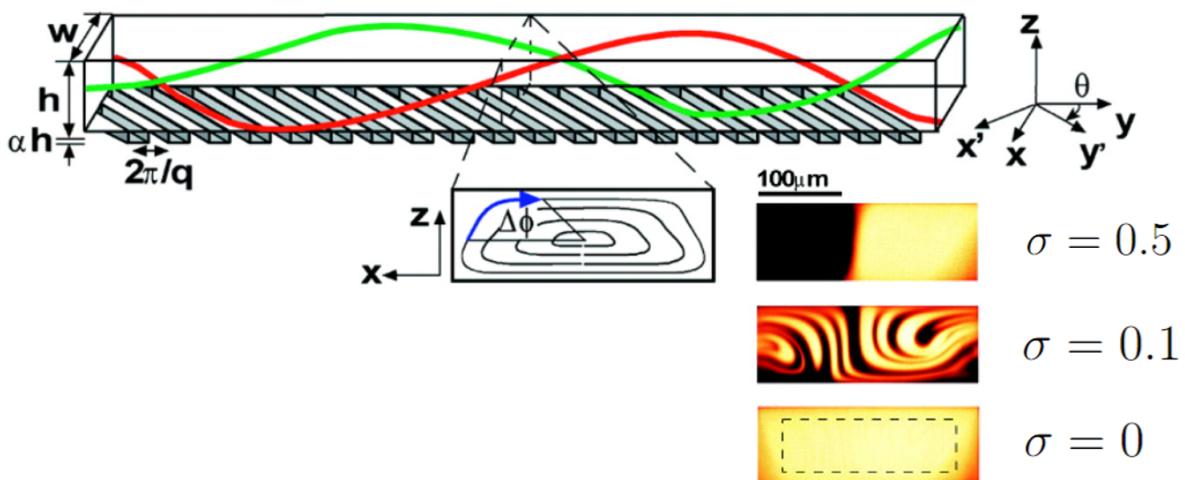


Fig. 1.1: Microchannel with microstructured pattern [12].

In figure 1.1 the microchannel is represented with a possible microstructured pattern on its lower wall. When the rough wall is introduced, the flow resistance along x' is larger than along y' . This leads to a non-zero transverse flow component which produces a helicoidal flow, represented by the green and red streamlines. The stretching and folding of the fluid volumes along the channel decrease the mixing length.

The interaction between solute transport and thin membranes at large Péclet numbers is also relevant in biology. Many sea sponges have a perforated structure such as, for instance, the deep-sea glass sponge *Euplectella aspergillum* shown in figure 1.2. This sponge has been studied for its mechanical properties such as the high flexibility and resilience, delaying crack propagation and resisting to buckling phenomena [13].

The *E. aspergillum* lives mostly in the Pacific ocean and near Antarctica, at depths below 500 metres. From a hydrodynamic point of view, the skeleton structure allows a recirculation region inside the body cavity, with a swirling motion at low flow velocity, as we can see in figure 1.3. This is particularly useful to trap nutrients like plankton which are then used by shrimps which live inside the sponge. Moreover, it

performs the mixing for their sperm and eggs.



Fig. 1.2: Euplectella auspergillum.

A model to describe the mass transport across thin permeable membranes at large Péclet numbers is still missing in the present literature.

The objective of the present thesis is to extend the model developed by Zampogna et al. in [11] to the case of non-negligible advection within the pores.

The thesis is structured as follows. In section 2 we introduce the governing equations and the mathematical model developed via homogenization. In section 3 we validate the model defined in the previous section. The pore geometry is defined, and the microscopic problem is solved with three different strategies. Then, the macroscopic solution is computed for a specific flow condition. The concentration predicted by the model is validated by comparisons with the solution of direct numerical simulations. In section 4 a new spatial average is defined to take into account for jumps in the concentration field across the membrane and the new model is validated following the same procedure. In section 5 we conclude with a summary of the results and future perspectives.

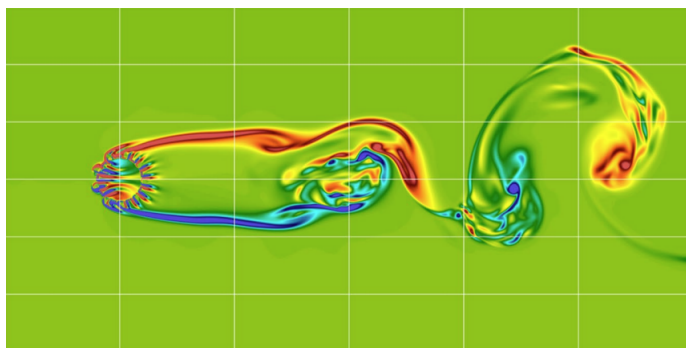


Fig. 1.3: Vorticity field in a cross section of the sponge [13].

2 Homogenization-Based Mathematical Model

The objective of the project is to develop a macroscopic model to describe flows through thin porous membranes at non-negligible Péclet numbers within the pores. In the present chapter we introduce the equations governing the physical phenomenon. We then apply homogenization to the considered set of equations to develop an interface condition to be imposed on a fictitious macroscopic membrane (the grey smooth surface in figure 2.1 *a*).

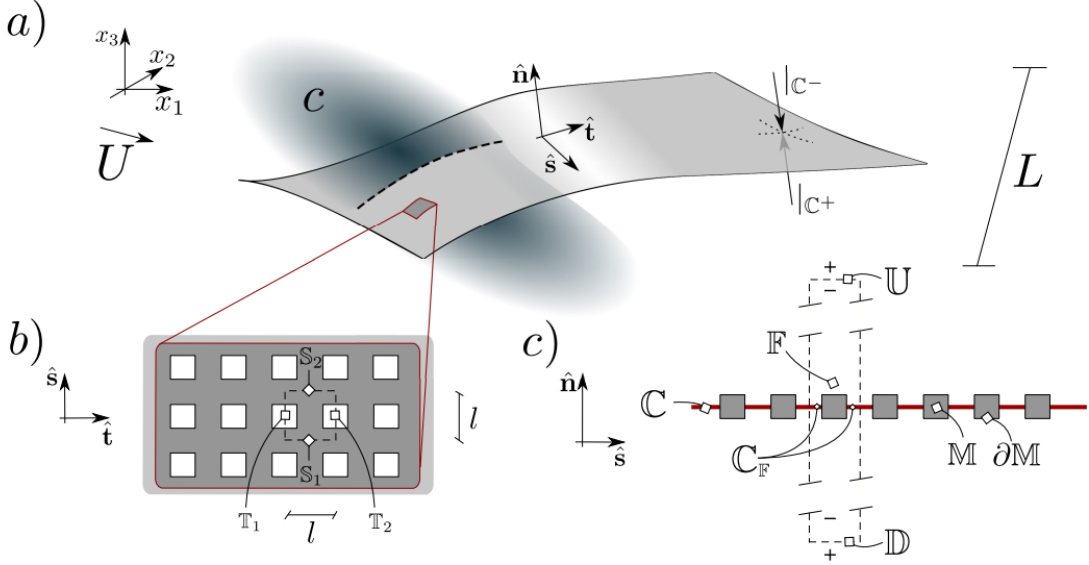


Fig. 2.1: Frame *a*): macroscopic membrane invested by a fluid with velocity U containing a solute with concentration c . The membrane is denoted by \mathbb{C} . Frame *b*) and *c*): zoom on the planes $(\hat{\mathbf{t}}, \hat{\mathbf{s}})$ and $(\hat{\mathbf{s}}, \hat{\mathbf{n}})$. The dashed lines represent the microscopic elementary cell, which is periodic along $\mathbb{T}_1, \mathbb{T}_2, \mathbb{S}_1, \mathbb{S}_2$. \mathbb{U} and \mathbb{D} are the sides of the microscopic cell placed in the far-field, where unperturbed flow conditions are valid.

We consider a solute of molecular diffusivity D transported by an incompressible Newtonian fluid, the solvent, of constant density ρ and viscosity μ . The solute-solvent couple encounters a porous membrane \mathbb{M} , sketched in figure 2.1. The variations of the solvent properties due to the concentration of the solute are neglected, i.e. we are in the diluted limit. The solvent velocity \hat{u}_i and pressure \hat{p} are governed by the Navier-Stokes equations:

$$\begin{cases} \hat{\partial}_i \hat{u}_i = 0 \\ \rho \hat{\partial}_t \hat{u}_i + \rho \hat{u}_j \hat{\partial}_j \hat{u}_i = -\hat{\partial}_i \hat{p} + \mu \hat{\partial}_{ll}^2 \hat{u}_i . \end{cases} \quad (2.1)$$

The solute concentration \hat{c} is governed by the advection–diffusion equation:

$$\hat{\partial}_i \hat{c} + \hat{\partial}_i \hat{F}_i = 0 , \quad (2.2)$$

where the concentration flux is defined as

$$\hat{F}_i = \hat{u}_i \hat{c} - D \hat{\partial}_i \hat{c} . \quad (2.3)$$

We can identify two different characteristic lengths, the macroscale L associated with the large-scale flow structures and the microscale l , characterizing the pores and the thickness of the membrane. The ratio between l and L defines a separation of scales parameter ε , i.e.

$$\varepsilon = \frac{l}{L} . \quad (2.4)$$

The membrane is formed by the periodic repetition of the microscopic elementary cell along the tangential-to-the-surface directions. The flow field is supposed to be periodic along $\hat{\mathbf{t}}$ and $\hat{\mathbf{s}}$.

2.1 Homogenization Procedure

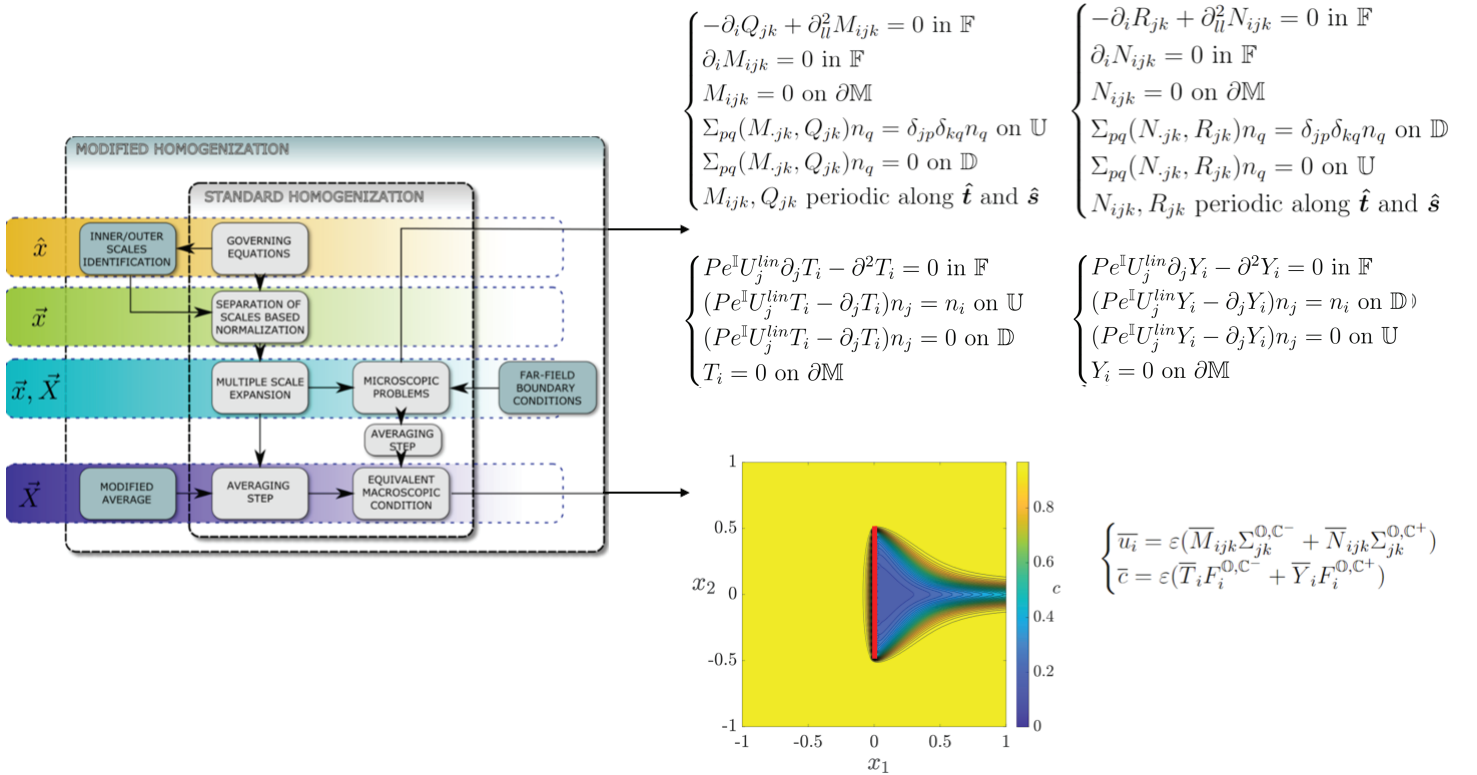


Fig. 2.2: Sketch of the homogenization procedure. On the left the spatial variables used for each step are highlighted. $\hat{\mathbf{x}}$ is the dimensional spatial variable, $\tilde{\mathbf{x}}$ and $\tilde{\mathbf{X}}$ are respectively the microscopic and macroscopic non-dimensional spatial variables. On the bottom right a sample macroscopic solution is sketched with the interface conditions for the macroscopic velocity \bar{u}_i and the concentration \bar{c} . On the top right the microscopic problems to find the tensors \mathbf{M} , \mathbf{N} , \mathbf{T} and \mathbf{Y} present in the macroscopic condition are listed.

The homogenization procedure follows the steps shown in figure 2.2. The relevant scales of the phenomenon are identified, allowing one to distinguish between inner and outer problems. The inner problem is defined within the microscopic elementary

cell, while the outer one far from the membrane. The governing equations are then normalized with these length scales.

A multiple scale decomposition of the inner solution is performed, including the asymptotic matching with the solution in the far field. To obtain the macroscopic conditions on the membrane, a spatial averaging step of the microscopic quantities is finally implemented.

2.1.1 Outer Problem

For the outer problem we introduce the following dimensionless variables

$$\begin{aligned}\hat{\mathbf{x}} &= L\mathbf{x}^\circ, & \hat{p} &= \Delta P p^\circ, & \hat{\mathbf{u}} &= U^\circ \mathbf{u}^\circ = \frac{L\Delta P}{\mu} \mathbf{u}^\circ, \\ \hat{c} &= \Delta C^\circ c^\circ, & \hat{t} &= Tt^\circ = \frac{L^2}{D} t^\circ.\end{aligned}\quad (2.5)$$

Substituting (2.5) within (2.1) and (2.2) we obtain:

$$\begin{cases} \frac{\partial}{\partial x_i^\circ} \left(\frac{l\Delta p}{l\mu} u_i^\circ \right) = 0 \\ \rho \frac{\partial}{\partial t} \left(\frac{U^\circ}{T} u_i^\circ \right) + \rho U^\circ u_j^\circ \frac{\partial}{\partial x_j^\circ} \left(\frac{L\Delta}{L\mu} u_i^\circ \right) = -\frac{\partial}{\partial x_i^\circ} \left(\frac{p^\circ \Delta p}{l} \right) + \mu \frac{\partial^2}{l^2} \left(\frac{l\Delta p}{\mu} \right) u_i^\circ. \\ \partial_t \frac{D}{L^2} \Delta c^\circ c^\circ + \frac{\partial_i}{L} \left(U^\circ u_i^\circ \Delta c^\circ c^\circ - D \partial_i \frac{\Delta c^\circ}{L} c^\circ \right) = \partial_t c^\circ + \frac{L^2}{D} \frac{1}{L} \left(U^\circ u_i^\circ c^\circ - D \partial_i \frac{c^\circ}{L} \right) = \\ = \partial_t c^\circ + \partial_i \left(\frac{L u_i^\circ}{D} u_i^\circ c^\circ - \partial_i c^\circ \right) = 0. \end{cases}$$

The outer problem can be rewritten as

$$\begin{cases} \partial_i u_i^\circ = 0 \\ Re^\circ (u_j^\circ \partial_j u_i^\circ) = -\partial_i p^\circ + \partial_{ll}^2 u_i^\circ \\ \partial_t c^\circ + \partial_i F_i^\circ = 0, \end{cases}\quad (2.6)$$

where

$$Re^\circ = \frac{\rho U^\circ L}{\mu}, \text{ and} \quad (2.7)$$

$$F_i^\circ = Pe^\circ u_i^\circ c^\circ - \partial_i c^\circ, \text{ with} \quad (2.8)$$

$$Pe^\circ = \frac{LU^\circ}{D}. \quad (2.9)$$

2.1.2 Inner Problem

We introduce the dimensionless variables for the inner problem

$$\begin{aligned}\hat{\mathbf{x}} &= l\mathbf{x}^{\mathbb{I}}, & \hat{p} &= \Delta P p^{\mathbb{I}}, & \hat{\mathbf{u}} &= U^{\mathbb{I}}\mathbf{u}^{\mathbb{I}} = \frac{l\Delta P}{\mu}\mathbf{u}^{\mathbb{I}}, \\ \hat{c} &= \Delta C^{\mathbb{I}}c^{\mathbb{I}} = \varepsilon\Delta C^{\mathbb{O}}c^{\mathbb{I}}, & \hat{t} &= Tt^{\mathbb{I}} = \frac{L^2}{D}t^{\mathbb{I}},\end{aligned}\quad (2.10)$$

where the pressure jump across the membrane is balanced by the local microscopic viscous stresses

$$\frac{\Delta p}{l} = \frac{\mu U}{l^2}. \quad (2.11)$$

Normalizing (2.1) with (2.10), we obtain

$$\begin{cases} \partial_i \left(\frac{l\Delta P}{\mu} u_i^{\mathbb{I}} \right) = 0 \\ Re^{\mathbb{I}} (u_j^{\mathbb{I}} \partial_j u_i^{\mathbb{I}}) = -\partial_i p^{\mathbb{I}} + \partial_{ll}^2 u_i^{\mathbb{I}}, \end{cases} \quad (2.12)$$

with $Re^{\mathbb{I}} = \frac{U^{\mathbb{I}}\rho l}{\mu}$. Substituting (2.10) in (2.2), we obtain

$$\begin{aligned}\partial_t \frac{D}{L^2} \varepsilon \Delta C^{\mathbb{O}} c^{\mathbb{I}} + \partial_i \left(U^{\mathbb{I}} u_i^{\mathbb{I}} \frac{\varepsilon \Delta C^{\mathbb{O}}}{l} c^{\mathbb{I}} - \frac{D \partial_i \Delta C^{\mathbb{O}} c^{\mathbb{I}}}{lL} \right) &= \varepsilon \partial_t c^{\mathbb{I}} + \partial_i \left(\varepsilon \frac{L}{l} \frac{LU^{\mathbb{I}}}{D} u_i^{\mathbb{I}} c^{\mathbb{I}} - \frac{L}{l} \partial_i c^{\mathbb{I}} \right) = \\ &= \varepsilon^2 \partial_t c^{\mathbb{I}} + \partial_i (Pe^{\mathbb{I}} u_i^{\mathbb{I}} c^{\mathbb{I}} - \partial_i c^{\mathbb{I}}) = 0,\end{aligned}\quad (2.13)$$

with $Pe^{\mathbb{I}} = \frac{U^{\mathbb{I}} l}{D}$. Assuming $Re^{\mathbb{I}} = \mathcal{O}(\varepsilon)$, the normalized governing equations are

$$\begin{cases} \partial_i u_i^{\mathbb{I}} = 0 \\ -\partial_i p^{\mathbb{I}} + \partial_{ll}^2 u_i^{\mathbb{I}} = 0 \\ \varepsilon^2 \partial_t c^{\mathbb{I}} + \partial_i F_i^{\mathbb{I}} = 0, \end{cases} \quad (2.14)$$

where $F_i^{\mathbb{I}} = Pe^{\mathbb{I}} u_i^{\mathbb{I}} c^{\mathbb{I}} - \partial_i c^{\mathbb{I}}$.

2.1.3 Matching Conditions

The matching conditions between the inner and the outer problems provide the boundary conditions on \mathbb{U} and \mathbb{D} . These conditions are

$$\hat{u}_i^- = \hat{u}_i^+, \quad (2.15)$$

$$\hat{c}^- = \hat{c}^+, \quad (2.16)$$

$$\hat{\Sigma}_{jk}^- n_k = \hat{\Sigma}_{jk}^+ n_k, \quad (2.17)$$

$$\hat{F}_i^- n_i = \hat{F}_i^+ n_i, \quad (2.18)$$

where the stress tensor is defined as

$$\hat{\Sigma}_{jk} = \hat{p} \delta_{jk} + 2\mu \hat{\epsilon}_{jk}(\hat{\mathbf{u}}), \quad (2.19)$$

and the strain $\hat{\epsilon}_{jk}$ is

$$\hat{\epsilon}_{jk} = \frac{1}{2}(\hat{\partial}_j \hat{u}_k + \hat{\partial}_k \hat{u}_j) . \quad (2.20)$$

The superscripts \cdot^- , \cdot^+ define the outer and the inner sides of \mathbb{U} and \mathbb{D} , as sketched in figure 2.1, frame c .

(2.15) and (2.16) state the continuity of velocity and concentration. (2.18) imposes the continuity of the normal-to-the-surface concentration flux while (2.17) the solvent stresses continuity.

The stress continuity (2.17) is normalized using (2.10) and (2.5)

$$\begin{aligned} (-\Delta P p^\mathbb{I} \delta_{jk} + 2\mu \frac{\Delta P}{\mu} \epsilon_{jk}(\mathbf{u}^\mathbb{I})) n_k &= (-\Delta P^\mathbb{O} p^\mathbb{O} \delta_{jk} + 2 \frac{U^\mathbb{O}}{L} \mu \epsilon_{jk}(\mathbf{u}^\mathbb{O})) n_k \Rightarrow \\ (-p^\mathbb{I} \delta_{jk} + 2\epsilon_{jk}(\mathbf{u}^\mathbb{I})) n_k &= (-\frac{\Delta P^\mathbb{O}}{\Delta P} p^\mathbb{O} \delta_{ij} + 2\mu \frac{U^\mathbb{O}}{L \Delta P} \epsilon_{jk}(\mathbf{u}^\mathbb{O})) n_k \Rightarrow \\ \Sigma_{jk}^\mathbb{I} n_k &= \Sigma_{jk}^\mathbb{O} n_k , \end{aligned} \quad (2.21)$$

with

$$\begin{aligned} \Sigma_{jk}^\mathbb{I} &= -p^\mathbb{I} \sigma_{jk} + 2\epsilon_{jk}(\mathbf{u}^\mathbb{I}) , \\ \Sigma_{jk}^\mathbb{O} &= -\frac{\Delta P^\mathbb{O}}{\Delta P} p^\mathbb{O} \delta_{ij} + 2\mu \frac{U^\mathbb{O}}{L \Delta P} \epsilon_{jk}(\mathbf{u}^\mathbb{O}) . \end{aligned} \quad (2.22)$$

The normalization of (2.18) gives

$$\begin{aligned} \left(\frac{U^\mathbb{I} u_i^\mathbb{I}}{D} \varepsilon \Delta c^\mathbb{O} c^\mathbb{I} - \partial_i \frac{\Delta c^\mathbb{O}}{L} c^\mathbb{I} \right) n_i &= \left(\frac{U^\mathbb{O} u_i^\mathbb{O} \Delta c^\mathbb{O} c^\mathbb{O}}{D} - \partial_i \frac{\Delta c^\mathbb{O}}{L} c^\mathbb{O} \right) n_i \Rightarrow \\ \left(P e^\mathbb{O} \frac{U^\mathbb{I}}{U^\mathbb{O}} \varepsilon u_i^\mathbb{I} c^\mathbb{I} - \partial_i c^\mathbb{I} \right) n_i &= (P e^\mathbb{O} u_i^\mathbb{O} c^\mathbb{O} - \partial_i c^\mathbb{O}) n_i . \end{aligned} \quad (2.23)$$

Since the continuity of the advective part of the flux is guaranteed by the continuity of concentration and velocity, using normalizations (2.15) and (2.16) in (2.23) we obtain

$$\partial_i c^\mathbb{I} n_i = \partial_i c^\mathbb{O} n_i . \quad (2.24)$$

2.1.4 Multiple Scale Expansion

We decompose the inner fields with a multiple scale expansion introducing the fast (microscopic) and slow (macroscopic) variables $\mathbf{x} = (x_1, x_2, x_3)$ and $\mathbf{X} = \varepsilon(x_1, x_2, x_3)$.

The following expansions are introduced

$$\mathbf{u}^\mathbb{I} = \sum_{n=0}^{+\infty} \varepsilon^n \mathbf{u}^{\mathbb{I},(n)}(\mathbf{x}, \mathbf{X}, t), \quad p^\mathbb{I} = \sum_{n=0}^{+\infty} \varepsilon^n p^{\mathbb{I},(n)}(\mathbf{x}, \mathbf{X}, t), \quad c^\mathbb{I} = \sum_{n=0}^{+\infty} \varepsilon^n c^{\mathbb{I},(n)}(\mathbf{x}, \mathbf{X}, t) . \quad (2.25)$$

The spatial derivatives are transformed following the rule:

$$\partial_i = \partial_i + \varepsilon \partial_I , \quad (2.26)$$

where the capital indices denote derivation with respect to \mathbf{X} . Substituting equation (2.25) and (2.26) in the Stokes equations and the advection-diffusion equation defined in the inner problem (2.14), we obtain:

$$\left\{ \begin{array}{l} \partial_i(u_i^{\mathbb{I},(0)} + \varepsilon u_i^{\mathbb{I},(1)}) + \varepsilon \partial_I(u_i^{\mathbb{I},(0)} + \varepsilon u_i^{\mathbb{I},(1)}) = 0 \\ -\partial_i(p^{\mathbb{I},(0)} + \varepsilon p^{\mathbb{I},(1)}) - \varepsilon \partial_I(p^{\mathbb{I},(0)} + \varepsilon p^{\mathbb{I},(1)}) + \partial_{ll}^2(u_i^{\mathbb{I},(0)} + \varepsilon u_i^{\mathbb{I},(1)}) + 2\varepsilon \partial_{lL}(u_i^{\mathbb{I},(0)} + \varepsilon u_i^{\mathbb{I},(1)}) + \\ + \varepsilon^2 \partial_{LL}^2(u_i^{\mathbb{I},(0)} + \varepsilon u_i^{\mathbb{I},(1)}) = 0 \\ \varepsilon^2 [\partial_t(c^{\mathbb{I},(0)} + \varepsilon c^{\mathbb{I},(1)}) + \varepsilon \partial_T(c^{\mathbb{I},(0)} + \varepsilon c^{\mathbb{I},(1)})] + \partial_i [Pe^{\mathbb{I}}(u_i^{\mathbb{I},(0)} + \varepsilon u_i^{\mathbb{I},(1)})(c^{\mathbb{I},(0)} + \varepsilon c^{\mathbb{I},(1)}) + \\ - \partial_i(c^{\mathbb{I},(0)} + \varepsilon c^{\mathbb{I},(1)}) - \varepsilon \partial_I(c^{\mathbb{I},(0)} + c^{\mathbb{I},(1)})] + \varepsilon \partial_I [Pe^{\mathbb{I}}(u_i^{\mathbb{I},(0)} + \varepsilon u_i^{\mathbb{I},(1)})(c^{\mathbb{I},(0)} + \varepsilon c^{\mathbb{I},(1)}) + \\ - \partial_i(c^{\mathbb{I},(0)} + \varepsilon c^{\mathbb{I},(1)}) - \varepsilon \partial_I(c^{\mathbb{I},(0)} + c^{\mathbb{I},(1)})] = 0 . \end{array} \right. \quad (2.27)$$

The advection–diffusion equation for $c^{\mathbb{I}}$ becomes

$$\begin{aligned} & \varepsilon^2 [\partial_t(c^{\mathbb{I},(0)} + \varepsilon c^{\mathbb{I},(1)}) + \varepsilon \partial_T(c^{\mathbb{I},(0)} + \varepsilon c^{\mathbb{I},(1)})] + \partial_i [Pe^{\mathbb{I}}(u_i^{\mathbb{I},(0)} c^{\mathbb{I},(0)} + \varepsilon u_i^{\mathbb{I},(0)} c^{\mathbb{I},(1)} + \varepsilon u_i^{\mathbb{I},(1)} c^{\mathbb{I},(0)} + \\ & + \varepsilon^2 u_i^{\mathbb{I},(1)} c^{\mathbb{I},(1)}) - \partial_i(c^{\mathbb{I},(0)} + c^{\mathbb{I},(1)}) - \varepsilon \partial_I(c^{\mathbb{I},(0)} + \varepsilon c^{\mathbb{I},(1)})] + \varepsilon \partial_I [Pe^{\mathbb{I}}(u_i^{\mathbb{I},(0)} c^{\mathbb{I},(0)} + \varepsilon u_i^{\mathbb{I},(0)} c^{\mathbb{I},(1)} + \\ & + \varepsilon u_i^{\mathbb{I},(1)} c^{\mathbb{I},(0)} + \varepsilon^2 u_i^{\mathbb{I},(1)} c^{\mathbb{I},(1)}) - \partial_i(c^{\mathbb{I},(0)} + \varepsilon c^{\mathbb{I},(1)}) - \varepsilon \partial_I(c^{\mathbb{I},(0)} + \varepsilon c^{\mathbb{I},(1)})] = 0 . \end{aligned} \quad (2.28)$$

Retaining the terms up to an order ε we obtain

$$\left\{ \begin{array}{l} \partial u_i^{\mathbb{I},(0)} + \varepsilon (\partial_i u_i^{\mathbb{I},(1)} + \partial_I u_i^{\mathbb{I},(0)}) = 0 \\ -\partial_i p^{\mathbb{I},(0)} + \partial_{ll}^2 u_i^{\mathbb{I},(0)} + \varepsilon (-\partial_i p^{\mathbb{I},(1)} - \partial_I p^{\mathbb{I},(0)} + \partial_{ll}^2 u_i^{\mathbb{I},(1)} + 2\partial_{lL} u_i^{\mathbb{I},(0)}) = 0 \\ \partial_i (Pe^{\mathbb{I}} u_i^{\mathbb{I},(0)} c^{\mathbb{I},(0)} - \partial_i c^{\mathbb{I},(0)}) + \varepsilon (\partial_i [Pe^{\mathbb{I}}(u_i^{\mathbb{I},(0)} c^{\mathbb{I},(1)} + u_i^{\mathbb{I},(1)} c^{\mathbb{I},(0)} - \partial_c^{\mathbb{I},(1)} - \partial_I c^{\mathbb{I},(0)}] + \\ + \partial_I (Pe^{\mathbb{I}} u_i^{\mathbb{I},(0)} c^{\mathbb{I},(0)} - \partial_i c^{\mathbb{I},(0)}) = 0 . \end{array} \right. \quad (2.29)$$

Collecting the leading order terms, the leading order equations are derived

$$\left\{ \begin{array}{l} \partial_i u_i^{\mathbb{I},(0)} = 0 \\ -\partial_i p^{\mathbb{I},(0)} + \partial_{ll}^2 u_i^{\mathbb{I},(0)} = 0 \\ \partial_i F_i^{\mathbb{I},(0)} = 0 , \end{array} \right. \quad (2.30)$$

with

$$F_i^{\mathbb{I},(0)} = Pe^{\mathbb{I}} u_i^{\mathbb{I},(0)} c^{\mathbb{I},(0)} - \partial_i c^{\mathbb{I},(0)} . \quad (2.31)$$

2.2 Microscopic Problem

The Cauchy problem within the microscopic elementary cell for the solvent and solute fields is

$$\left\{ \begin{array}{l} \partial_i u_i^{\mathbb{I},(0)} = 0 \\ -\partial_i p^{\mathbb{I},(0)} + \partial_{ll}^2 u_i^{\mathbb{I},(0)} = 0 \\ \Sigma_{ij}(u_i^{\mathbb{I},(0)}, p^{\mathbb{I},(0)})n_j = \Sigma_{ij}^{\mathbb{O},\mathbb{U}} n_j \text{ on } \mathbb{U} \\ \Sigma_{ij}(u_i^{\mathbb{I},(0)}, p^{\mathbb{I},(0)})n_j = \Sigma_{ij}^{\mathbb{O},\mathbb{D}} n_j \text{ on } \mathbb{D} \\ u_i^{\mathbb{I},(0)} = 0 \text{ on } \partial\mathbb{M} \\ \partial_i Pe^{\mathbb{I}} u_i^{\mathbb{I},(0)} c^{\mathbb{I},(0)} - \partial_i c^{\mathbb{I},(0)} = 0 \\ F_i^{\mathbb{I},(0)} n_i = F_i^{\mathbb{O},\mathbb{U}} n_i \text{ on } \mathbb{U} \\ F_i^{\mathbb{I},(0)} n_i = F_i^{\mathbb{O},\mathbb{D}} n_i \text{ on } \mathbb{D} \\ c^{\mathbb{I},(0)} = 0 \text{ on } \partial\mathbb{M} . \end{array} \right. \quad (2.32)$$

To formally write the solution of (2.32) the advection-diffusion equation is linearized using $u_i^{\mathbb{I},(0)} = U_i^{lin}$, where U_i^{lin} will be specified later on. The solution of (2.32) can be finally written as

$$\left\{ \begin{array}{l} u_i^{\mathbb{I},(0)} = M_{ijk} \Sigma_{jk}^{\mathbb{O},\mathbb{U}} + N_{ijk} \Sigma_{jk}^{\mathbb{O},\mathbb{D}} \\ p^{\mathbb{I},(0)} = Q_{jk} \Sigma_{jk}^{\mathbb{O},\mathbb{U}} + R_{jk} \Sigma_{jk}^{\mathbb{O},\mathbb{D}} \\ c^{\mathbb{I},(0)} = T_i F_i^{\mathbb{O},\mathbb{U}} + Y_i F_i^{\mathbb{O},\mathbb{D}} . \end{array} \right. \quad (2.33)$$

Substituting equations (2.33) in (2.32) we obtain

$$\left\{ \begin{array}{l} \partial_i M_{ijk} \Sigma_{jk}^{\mathbb{O},\mathbb{U}} + \partial_i N_{ijk} \Sigma_{jk}^{\mathbb{O},\mathbb{D}} = 0 \\ -\partial_i Q_{jk} \Sigma_{jk}^{\mathbb{O},\mathbb{U}} - \partial_i R_{jk} \Sigma_{jk}^{\mathbb{O},\mathbb{D}} + \partial_{ll}^2 M_{ijk} \Sigma_{jk}^{\mathbb{O},\mathbb{U}} + \partial_{ll}^2 N_{ijk} \Sigma_{jk}^{\mathbb{O},\mathbb{D}} = 0 \\ (-Q_{jk} \Sigma_{jk}^{\mathbb{O},\mathbb{U}} - R_{jk} \Sigma_{jk}^{\mathbb{O},\mathbb{D}} + 2\epsilon_{jk} M_{ijk} \Sigma_{jk}^{\mathbb{O},\mathbb{U}} + 2\epsilon_{jk} N_{ijk} \Sigma_{jk}^{\mathbb{O},\mathbb{D}})n_j = \Sigma_{jk}^{\mathbb{O},\mathbb{U}} \delta_{jp} \delta_{kq} n_j \text{ on } \mathbb{U} \\ (-Q_{jk} \Sigma_{jk}^{\mathbb{O},\mathbb{U}} - R_{jk} \Sigma_{jk}^{\mathbb{O},\mathbb{D}} + 2\epsilon_{jk} M_{ijk} \Sigma_{jk}^{\mathbb{O},\mathbb{U}} + 2\epsilon_{jk} N_{ijk} \Sigma_{jk}^{\mathbb{O},\mathbb{D}})n_j = \Sigma_{jk}^{\mathbb{O},\mathbb{D}} \delta_{jp} \delta_{kq} n_j \text{ on } \mathbb{D} \\ M_{ijk} \Sigma_{jk}^{\mathbb{O},\mathbb{U}} + N_{ijk} \Sigma_{jk}^{\mathbb{O},\mathbb{D}} = 0 \text{ on } \partial\mathbb{M} \\ \partial_i Pe^{\mathbb{I}} U_i^{lin} T_i F_i^{\mathbb{O},\mathbb{U}} + \partial_i Pe^{\mathbb{I}} U_i^{lin} Y_i F_i^{\mathbb{O},\mathbb{D}} - \partial_i^2 T_i F_i^{\mathbb{O},\mathbb{U}} - \partial_i^2 Y_i F_i^{\mathbb{O},\mathbb{D}} = 0 \\ (Pe^{\mathbb{I}} U_i^{lin} T_i F_i^{\mathbb{O},\mathbb{U}} + Pe^{\mathbb{I}} U_i^{lin} Y_i F_i^{\mathbb{O},\mathbb{D}} - \partial_i T_i F_i^{\mathbb{O},\mathbb{U}} - \partial_i Y_i F_i^{\mathbb{O},\mathbb{D}})n_i = F_i^{\mathbb{O},\mathbb{U}} n_i \text{ on } \mathbb{U} \\ (Pe^{\mathbb{I}} U_i^{lin} T_i F_i^{\mathbb{O},\mathbb{U}} + Pe^{\mathbb{I}} U_i^{lin} Y_i F_i^{\mathbb{O},\mathbb{D}} - \partial_i T_i F_i^{\mathbb{O},\mathbb{U}} - \partial_i Y_i F_i^{\mathbb{O},\mathbb{D}})n_i = F_i^{\mathbb{O},\mathbb{D}} n_i \text{ on } \mathbb{D} \\ T_i F_i^{\mathbb{O},\mathbb{U}} + Y_i F_i^{\mathbb{O},\mathbb{D}} = 0 \text{ on } \partial\mathbb{M} . \end{array} \right. \quad (2.34)$$

Separating the variables \mathbf{x} and \mathbf{X} , and defining

$$\begin{aligned} \Sigma_{pq}(M_{.jk}, Q_{jk}) &:= -Q_{jk} \delta_{pq} + 2\epsilon_{pq} M_{ijk} \\ \Sigma_{pq}(N_{.jk}, R_{jk}) &:= -R_{jk} \delta_{pq} + 2\epsilon_{pq} N_{ijk} , \end{aligned} \quad (2.35)$$

the following microscopic problems are found

$$\left\{ \begin{array}{l} -\partial_i Q_{jk} + \partial_{ll}^2 M_{ijk} = 0 \text{ in } \mathbb{F} \\ \partial_i M_{ijk} = 0 \text{ in } \mathbb{F} \\ M_{ijk} = 0 \text{ on } \partial\mathbb{M} \\ \Sigma_{pq}(M_{.jk}, Q_{jk})n_q = \delta_{jp}\delta_{kq}n_q \text{ on } \mathbb{U} \\ \Sigma_{pq}(M_{.jk}, Q_{jk})n_q = 0 \text{ on } \mathbb{D} \\ M_{ijk}, Q_{jk} \text{ periodic along } \hat{\mathbf{t}} \text{ and } \hat{\mathbf{s}} \end{array} \right. \quad \left\{ \begin{array}{l} -\partial_i R_{jk} + \partial_{ll}^2 N_{ijk} = 0 \text{ in } \mathbb{F} \\ \partial_i N_{ijk} = 0 \text{ in } \mathbb{F} \\ N_{ijk} = 0 \text{ on } \partial\mathbb{M} \\ \Sigma_{pq}(N_{.jk}, R_{jk})n_q = \delta_{jp}\delta_{kq}n_q \text{ on } \mathbb{D} \\ \Sigma_{pq}(N_{.jk}, R_{jk})n_q = 0 \text{ on } \mathbb{U} \\ N_{ijk}, R_{jk} \text{ periodic along } \hat{\mathbf{t}} \text{ and } \hat{\mathbf{s}} \end{array} \right. \quad (2.36)$$

$$\left\{ \begin{array}{l} Pe^{\mathbb{I}} U_j^{lin} \partial_j T_i - \partial^2 T_i = 0 \text{ in } \mathbb{F} \\ (Pe^{\mathbb{I}} U_j^{lin} T_i - \partial_j T_i)n_j = n_i \text{ on } \mathbb{U} \\ (Pe^{\mathbb{I}} U_j^{lin} T_i - \partial_j T_i)n_j = 0 \text{ on } \mathbb{D} \\ T_i = 0 \text{ on } \partial\mathbb{M} \end{array} \right. \quad \left\{ \begin{array}{l} Pe^{\mathbb{I}} U_j^{lin} \partial_j Y_i - \partial^2 Y_i = 0 \text{ in } \mathbb{F} \\ (Pe^{\mathbb{I}} U_j^{lin} Y_i - \partial_j Y_i)n_j = n_i \text{ on } \mathbb{D} \\ (Pe^{\mathbb{I}} U_j^{lin} Y_i - \partial_j Y_i)n_j = 0 \text{ on } \mathbb{U} \\ Y_i = 0 \text{ on } \partial\mathbb{M} . \end{array} \right. \quad (2.37)$$

The microscopic problems (2.36) and (2.37) allow one to find the values of the tensors and vectors \mathbf{M} , \mathbf{N} , \mathbf{T} and \mathbf{Y} . The solution of problem (2.37) is computed upon choice of a closure for U_i^{lin} . Three different closures are specified in sections 2.3.1, 2.3.2, and 2.3.3.

2.3 Macroscopic Problem

Once the microscopic quantities \mathbf{M} , \mathbf{N} , \mathbf{Q} , \mathbf{R} , \mathbf{T} , \mathbf{Y} are found, equation (2.33) is upscaled via the introduction of a surface average within the microscopic domain

$$\bar{\cdot} = \frac{1}{\mathbb{C}_{\mathbb{F}} \cup \mathbb{C}_{\mathbb{M}}} \int_{\mathbb{C}_{\mathbb{F}}} \cdot dV \quad (2.38)$$

where $\mathbb{C}_{\mathbb{F}}$ and $\mathbb{C}_{\mathbb{M}}$ are respectively the portion of the volume occupied by the fluid and by the solid over \mathbb{C} .

Applying the average (2.38) and dimensionalizing (2.33) with the macroscopic scales (2.5) we obtain

$$\begin{aligned} \hat{u} \frac{\mu}{l\Delta P} &= \bar{M}_{ijk} \left(-\frac{\hat{p}}{\Delta P} \delta_{jk} + 2\frac{\mu}{\Delta P} \epsilon_{jk}(\hat{\mathbf{u}}) \right) + \bar{N}_{ijk} \left(-\frac{\hat{p}}{\Delta P} \delta_{jk} + 2\frac{\mu}{\Delta P} \epsilon_{jk}(\hat{\mathbf{u}}) \right) \Rightarrow \\ \bar{u}_i \frac{L\Delta P}{\mu} &= \bar{M}_{ijk} \left(-\Delta P p^{\circ} \frac{l}{\mu} \delta_{jk} + 2l \frac{\Delta P}{\mu} \epsilon_{jk}(\hat{\mathbf{u}}^{\circ}) \right) + \bar{N}_{ijk} \left(-\Delta P p^{\circ} \frac{l}{\mu} \delta_{jk} + 2l \frac{\Delta P}{\mu} \epsilon_{jk}(\hat{\mathbf{u}}^{\circ}) \right) \Rightarrow \\ \bar{u}_i &= \bar{M}_{ijk} \epsilon(-p^{\circ} \delta_{jk} + 2\epsilon_{jk}(\hat{\mathbf{u}}^{\circ})) + \bar{N}_{ijk} \epsilon(-p^{\circ} \delta_{jk} + 2\epsilon_{jk}(\hat{\mathbf{u}}^{\circ})) \end{aligned} \quad (2.39)$$

$$\begin{aligned} \frac{\hat{c}}{\Delta c^{\mathbb{I}}} &= \bar{T}_n \left(Pe^{\circ} \frac{\hat{u}\hat{c}}{U^{\circ}\Delta c^{\circ}} + \frac{L}{\Delta c^{\circ}} \hat{\partial}_i \hat{c} \right) + \bar{Y}_n \left(Pe^{\circ} \frac{\hat{u}\hat{c}}{U^{\circ}\Delta c^{\circ}} + \frac{L}{\Delta c^{\circ}} \hat{\partial}_i \hat{c} \right) \Rightarrow \\ \bar{c} \frac{\Delta c^{\circ}}{\Delta c^{\mathbb{I}}} &= \bar{T}_n (Pe^{\circ} u^{\circ} c^{\circ} - \partial_i c^{\circ}) + \bar{Y}_n (Pe^{\circ} u^{\circ} c^{\circ} - \partial_i c^{\circ}) \end{aligned} \quad (2.40)$$

which can be finally simplified to

$$\begin{cases} \bar{u}_i = \varepsilon(\bar{M}_{ijk}\Sigma_{jk}^{\mathbb{O},\mathbb{C}^-} + \bar{N}_{ijk}\Sigma_{jk}^{\mathbb{O},\mathbb{C}^+}) \\ \bar{c} = \varepsilon(\bar{T}_i F_i^{\mathbb{O},\mathbb{C}^-} + \bar{Y}_i F_i^{\mathbb{O},\mathbb{C}^+}) \end{cases} \quad (2.41)$$

where superscripts \mathbb{C}^+ and \mathbb{C}^- mean that stresses and fluxes are evaluated on the upward and downward sides of the membrane. The equations state a stress and concentration flux jump across the membrane, weighted by the tensors obtained from the microscopic problems.

2.3.1 Strategy A: advection via an Oseen linearization

The first closure strategy for U_i^{lin} consists of an Oseen linearization of the advective velocity, where U_i^{lin} is assumed constant within the microscopic domain. U_i^{lin} is evaluated from the macroscopic solution of the hydrodynamic part of the model, i.e.

$$U_i^{lin} = \overline{u_i^{\mathbb{I},(0)}} , \quad (2.42)$$

for each unit cell forming the membrane.

2.3.2 Strategy B: advection via a microscopic velocity retrieved from the macroscopic stresses along the membrane.

The second closure strategy consists of replacing U_i^{lin} with the hydrodynamic solution itself (cf. equation 2.33), i.e.

$$U_i^{lin} = M_{ijk}\Sigma_{jk}^{\mathbb{O},\mathbb{U}} + N_{ijk}\Sigma_{jk}^{\mathbb{O},\mathbb{D}} \quad (2.43)$$

where $\Sigma_{jk}^{\mathbb{O},\mathbb{U}}$ and $\Sigma_{jk}^{\mathbb{O},\mathbb{D}}$ are evaluated from the macroscopic solution and vary along the macroscopic membrane.

2.3.3 Strategy C: advection via a simplified velocity field

A simplified advective velocity is built. The microscopic field M_{nin} , associated to the normal part of the fluid tractions, renormalized by the average normal velocity at the membrane, defines U_i^{lin} , i.e.

$$U_i^{lin} = \frac{\bar{u}_n^{\mathbb{O}}}{\bar{M}_{nnn}} M_{nin} \quad (2.44)$$

The use of this last approach will *a posteriori* reveal that the tangential-to-the-membrane velocity, i.e. the tangential part of the fluid tractions, does not contribute to modifications of the effective diffusion vectors \mathbf{T} and \mathbf{Y} .

The three strategies are summarized in figure 2.3.

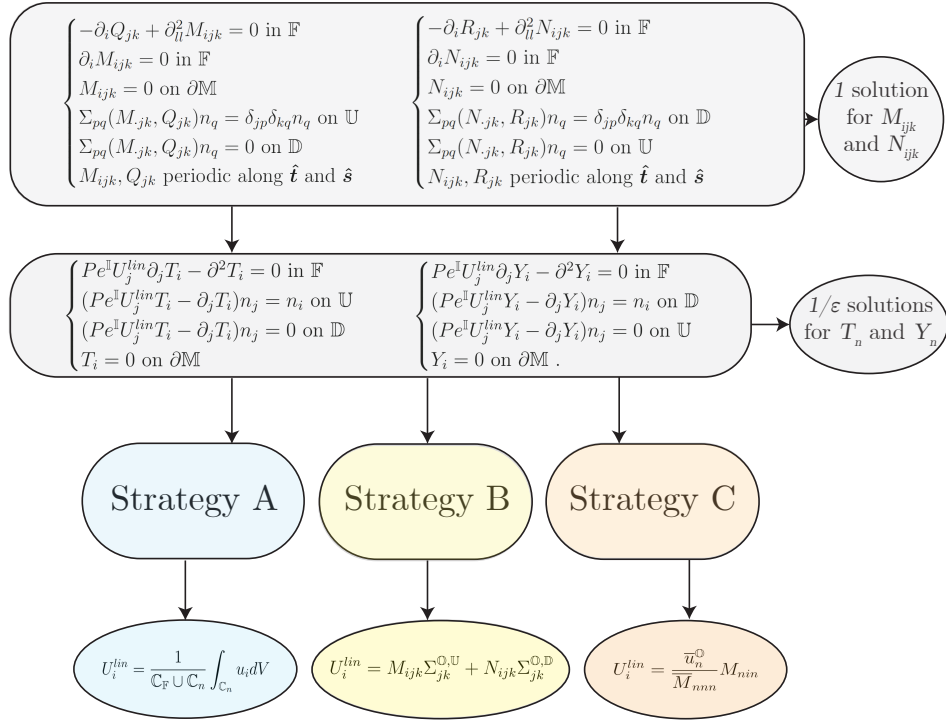


Fig. 2.3: Representation of the steps for the three strategies.

3 Flow past a planar membrane

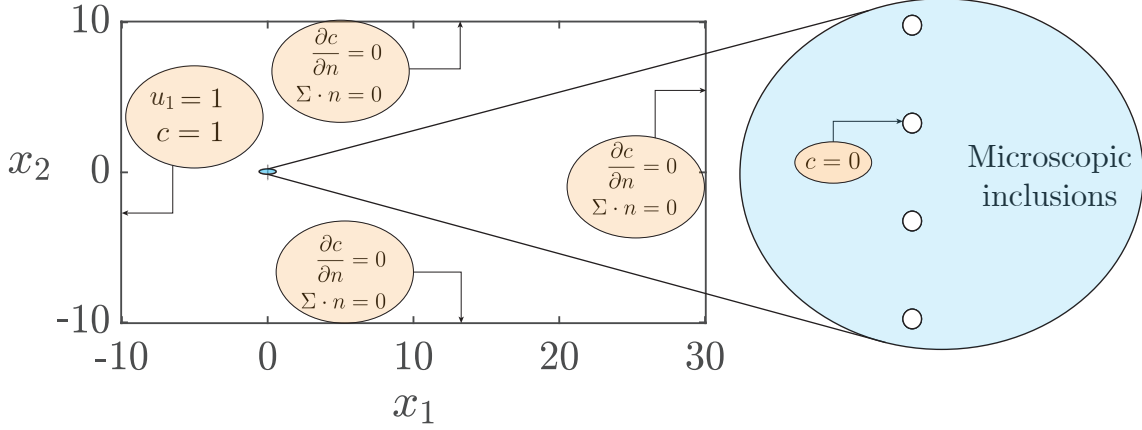


Fig. 3.1: Macroscopic computational domain and microscopic geometry. In orange we can see the conditions employed at the boundaries of the computational domain.

In this chapter we present a first flow configuration (cf. figure 3.1). The macroscopic geometry is a 2D flat plate, whose length is equal to 1. Each inclusion has a circular geometry with a radius equal to 0.005. Twenty inclusions are placed on the plate and the distance between them is 0.05. The value of ε is $\frac{0.05L}{L} = 0.05$. The numerical results present in this section are carried out using the software Comsol Multiphysics. We refer to appendix A and B for further details on the numerics.

3.1 Solution of the Microscopic Problems

Problems (2.36) and (2.37) have been solved within the microscopic domain. The isocontours of the microscopic tensors \mathbf{M} and \mathbf{N} are represented in figure 3.2 and figure 3.3. Only the entries of \mathbf{M} and \mathbf{N} whose average is different from zero are shown. M_{nnn} and N_{nnn} are called permeability, since they represent the ability of the fluid to flow along the normal-to-the-membrane direction. M_{ttn} and N_{ttn} are called slip since they represent the ability of the fluid to flow along the tangential-to-the-membrane direction. The values integrated on \mathbb{C} satisfy the correlations $\overline{M}_{nnn} = -\overline{N}_{nnn}$ and $\overline{M}_{ttn} = -\overline{N}_{ttn}$.

Integrating along the mean line, the values in table 3.1 are obtained.

Component	Value
\overline{M}_{nnn}	0.079348
\overline{N}_{nnn}	-0.079348
\overline{M}_{ttn}	0.027575
\overline{N}_{ttn}	-0.027575

Tab. 3.1: Non-zero averaged values of the tensors \mathbf{M} and \mathbf{N} .

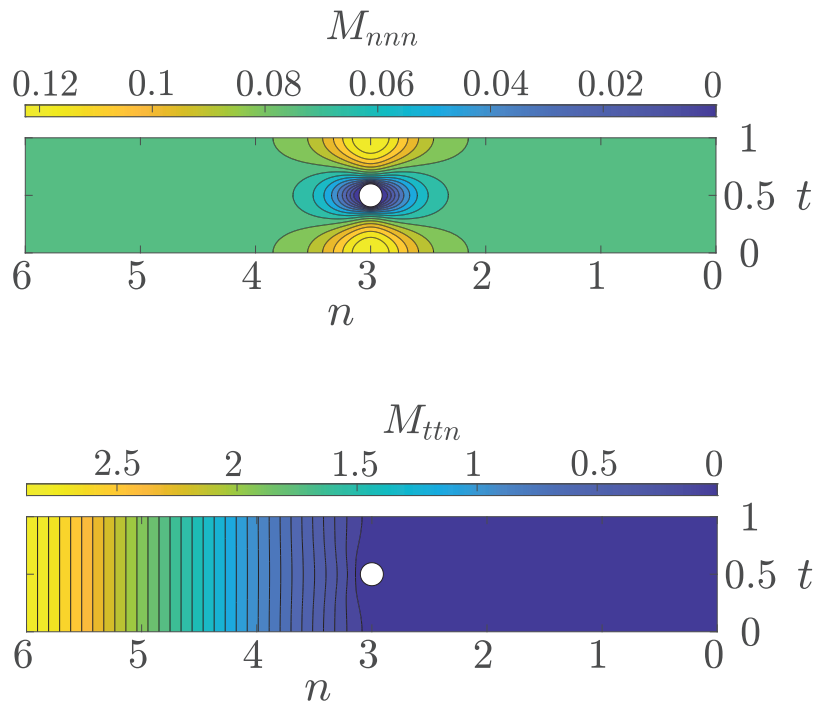


Fig. 3.2: Top frame: isocontours of M_{nnn} . Bottom frame: isocontours of M_{ttn} .

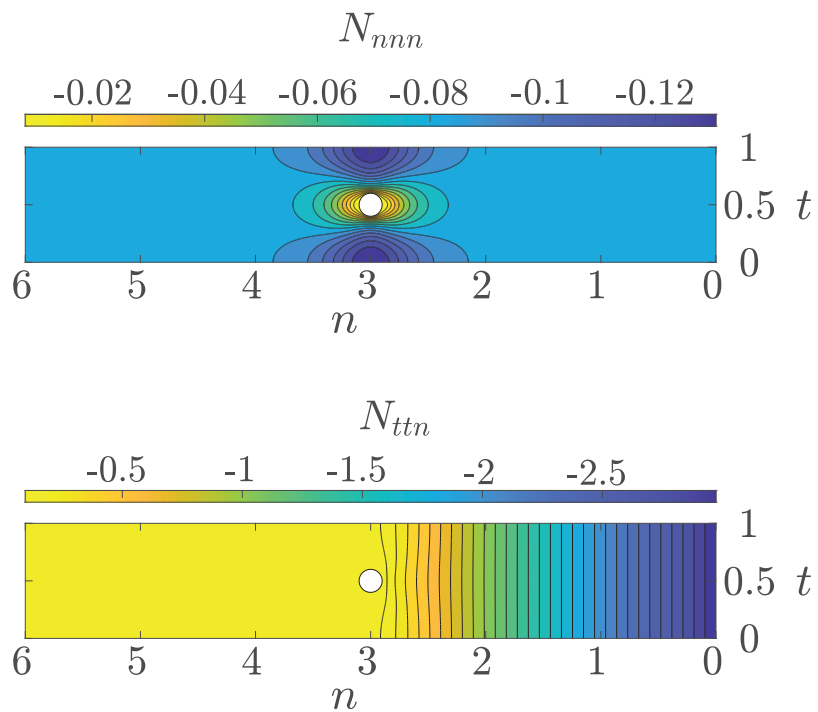


Fig. 3.3: Top frame: isocontours of N_{nnn} . Bottom frame: isocontours of N_{ttn} .

3.1.1 Effective diffusion vectors \mathbf{T} and \mathbf{Y} : strategy A

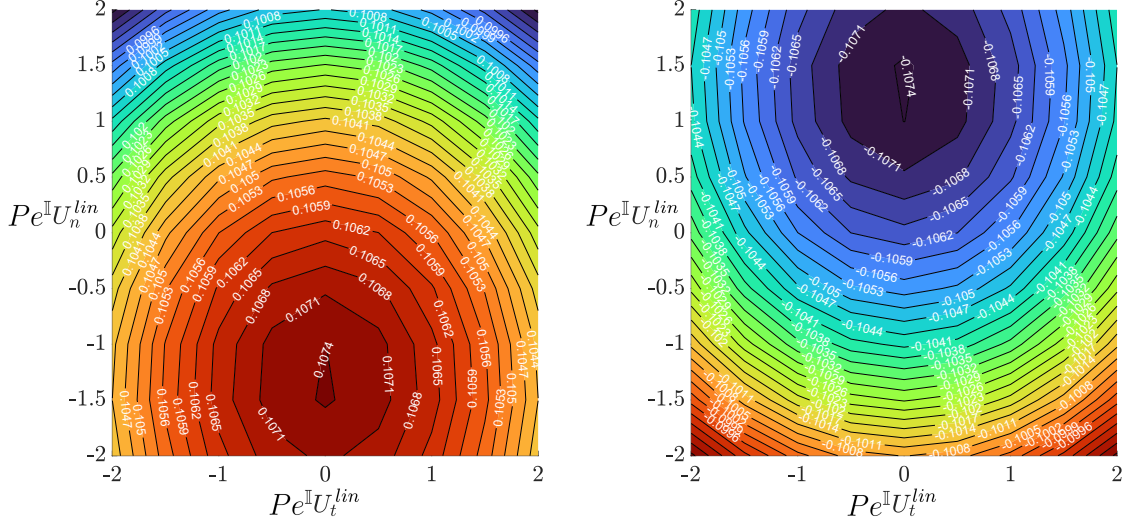


Fig. 3.4: Variations of \bar{T}_n (left) and \bar{Y}_n (right) with $Pe^{\text{II}}U_i^{\text{lin}}$.

A parametric study is performed to show the variations of \mathbf{T} and \mathbf{Y} with U_i^{lin} , defined for strategy A, in equation (2.42). Different values of U_i^{lin} lead to different values of T_n and Y_n , since it represent a constant advective field within the microscopic cell. The two vector components measure the modifications of the diffusion normal to the membrane for the presence of the pores, and can be written as

$$\begin{aligned}\bar{T}_n &= \bar{T}_n(U_t^{\text{lin}}, U_n^{\text{lin}}) \\ \bar{Y}_n &= \bar{Y}_n(U_t^{\text{lin}}, U_n^{\text{lin}})\end{aligned}\quad (3.1)$$

The obtained function has a maximum for \bar{T}_n in $U_n^{\text{lin}} = -1.4$ and $U_t^{\text{lin}} = 0$. Instead, \bar{Y}_n has a minimum in $-U_n^{\text{lin}}$ and U_t^{lin} .

The relation $\bar{T}_n(U_t^{\text{lin}}, U_n^{\text{lin}}) = -\bar{Y}_n(-U_t^{\text{lin}}, -U_n^{\text{lin}})$ holds.

3.1.2 Effective diffusion vectors \mathbf{T} and \mathbf{Y} : strategy B

Strategy B consists of rebuilding the microscopic advective velocity from the values of the normal and tangential tractions components on the upper and bottom sides of the microscopic domain \mathbb{U} and \mathbb{D} . The variations of \mathbf{T} and \mathbf{Y} are then analyzed for variations of the stress components S_n and S_t .

$$\begin{aligned}S_n^{\mathbb{U}, \mathbb{D}} &= n_i \Sigma_{ij} n_j \big|_{\mathbb{U}, \mathbb{D}} \\ S_t^{\mathbb{U}, \mathbb{D}} &= t_i \Sigma_{ij} n_j \big|_{\mathbb{U}, \mathbb{D}}.\end{aligned}\quad (3.2)$$

The superscripts \mathbb{U} and \mathbb{D} indicate that the stresses are evaluated on the upward or downward side of the microscopic domain. The variations of \bar{T}_n and \bar{Y}_n are represented in figure 3.5, 3.6, 3.7.

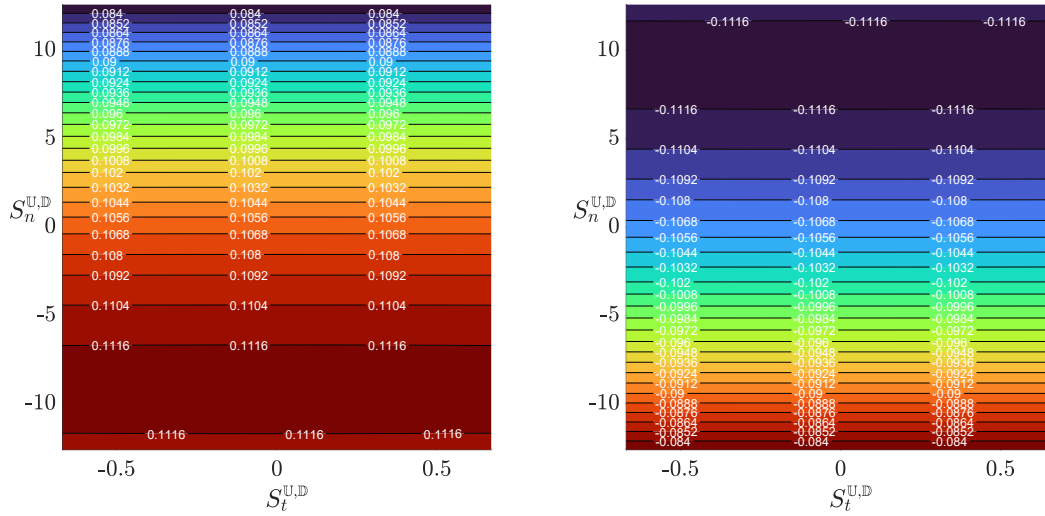


Fig. 3.5: Variations of \bar{T}_n (left) and \bar{Y}_n (right) with S_i . The maps are obtained for $S_n^U = S_n^D$ and $S_t^U = S_t^D$.

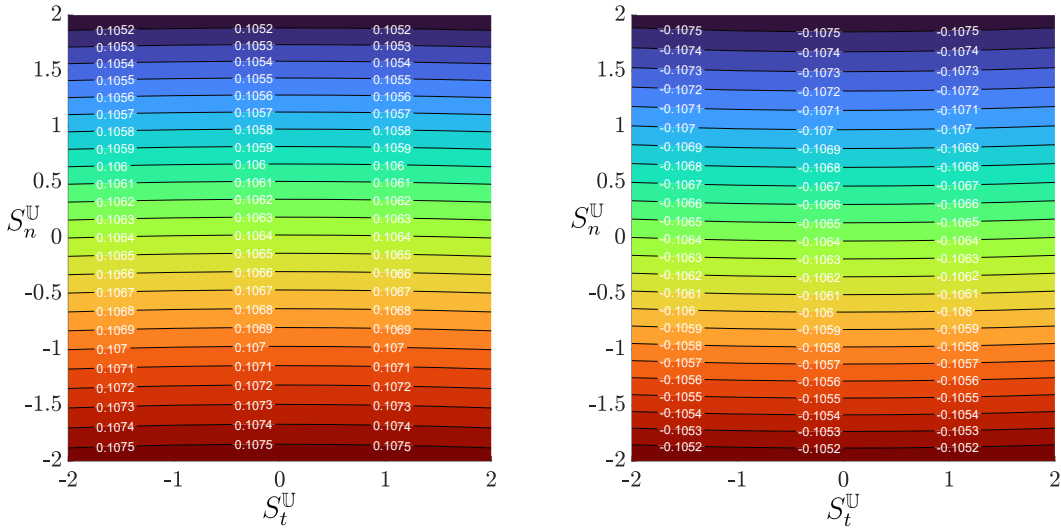


Fig. 3.6: Variations of \bar{T}_n (left) and \bar{Y}_n (right) with S_i . The maps are obtained for $S_n^D = S_t^D = 0$.

From these figures we notice that large variations of \bar{T}_n and \bar{Y}_n are given by the normal component of the stress tensor S_n , while S_t has a minor, negligible, effect on the vectors components. This behaviour is confirmed by figure 3.8. The variations of \bar{T}_n and \bar{Y}_n with respect to S_t^U and S_t^D are below 3%.

From this analysis we can conclude that the tangential part of the normal stresses, defining the tangential velocity U_t^{lin} , can be neglected when calculating the vectors \bar{T}_n and \bar{Y}_n , and this leads to the third strategy to close the problems for \bar{T}_n and \bar{Y}_n . The relations between \bar{T}_n and \bar{Y}_n listed in section 3.1.1 are valid also in this case.

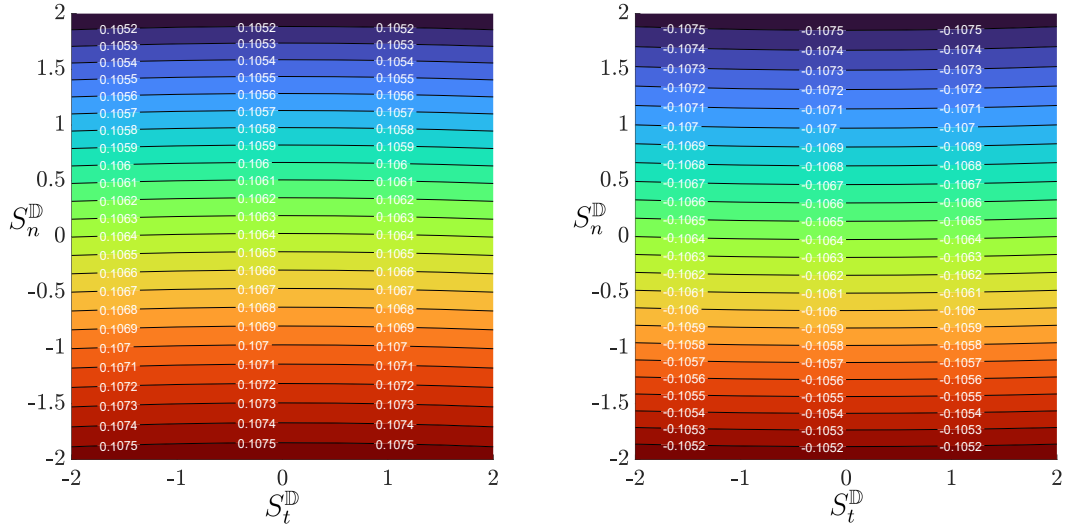


Fig. 3.7: Variations of \bar{T}_n (left) and \bar{Y}_n (right) with S_i . The maps are obtained for $S_n^U = S_t^U = 0$.

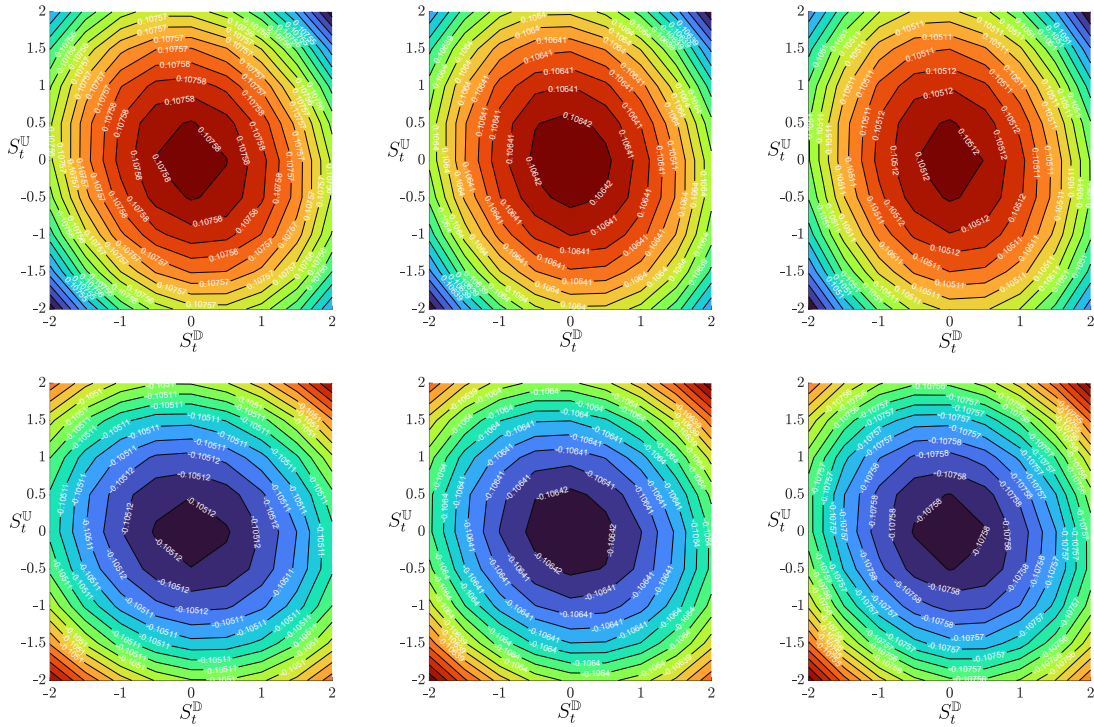


Fig. 3.8: Top frames: maps of \bar{T}_n . Bottom frames: maps of \bar{Y}_n . Each column corresponds to a different value of $S_n^U = S_n^D$; -2, 0, 2 from left to right.

3.1.3 Effective diffusion vectors \mathbf{T} and \mathbf{Y} : strategy C

The objective of strategy C is to provide a minimal model to retrieve the microscopic advective velocity.

To simplify the calculation, only the velocity component arising from the normal-to-the-membrane fluid tractions is extracted from the macroscopic solution and imposed

as advective velocity field, since the tangential one has a negligible effect on \bar{T}_n and \bar{Y}_n , as observed in figure 3.8. In figure 3.9 we can see the values of \bar{T}_n and \bar{Y}_n computed using this strategy (cf. the definition of U_i^{lin} in 2.44). The relations between \bar{T}_n and \bar{Y}_n listed in section 3.1.1 are valid also in this case.

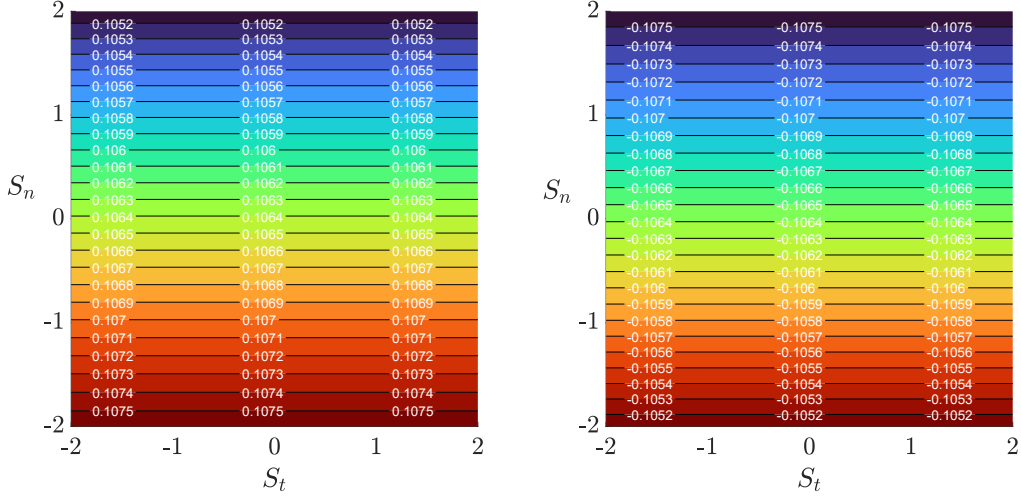


Fig. 3.9: Variations of \bar{T}_n (left) and \bar{Y}_n (right) with S_i . The maps are obtained in the case of strategy C.

3.1.4 Comparison between the strategies

The three strategies provide the same values of \bar{T}_n and \bar{Y}_n for small Pe^{II} . If $Pe^{\text{II}} > 10^{-2}$ the values of the effective vectors differ (cf. figure 3.10 where the average values of T_n and Y_n are shown for strategy A and C). Strategy B and C provide similar values of \bar{T}_n and \bar{Y}_n and the comparison is not shown here.

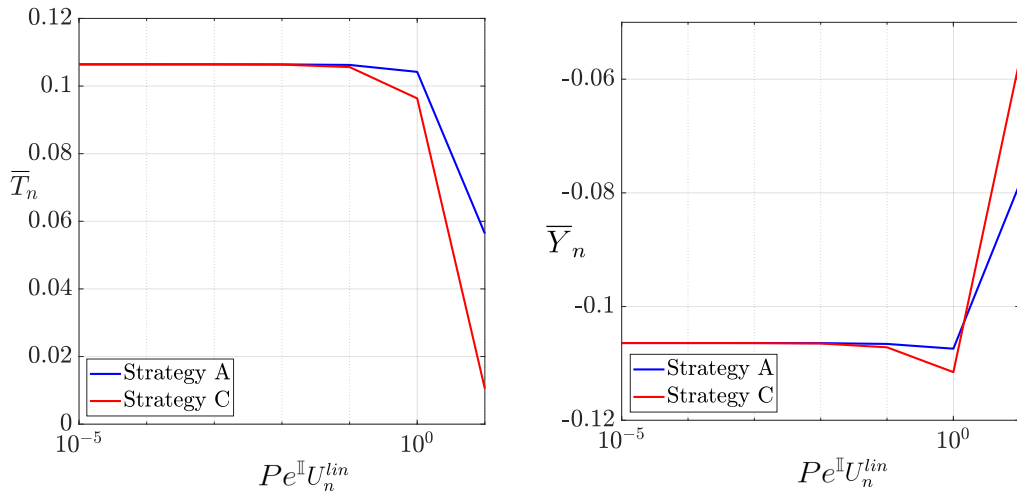


Fig. 3.10: \bar{T}_n and \bar{Y}_n with $Pe^{\text{II}}U_n^{lin}$ and for $U_t^{lin} = 0$, using strategies A and B.

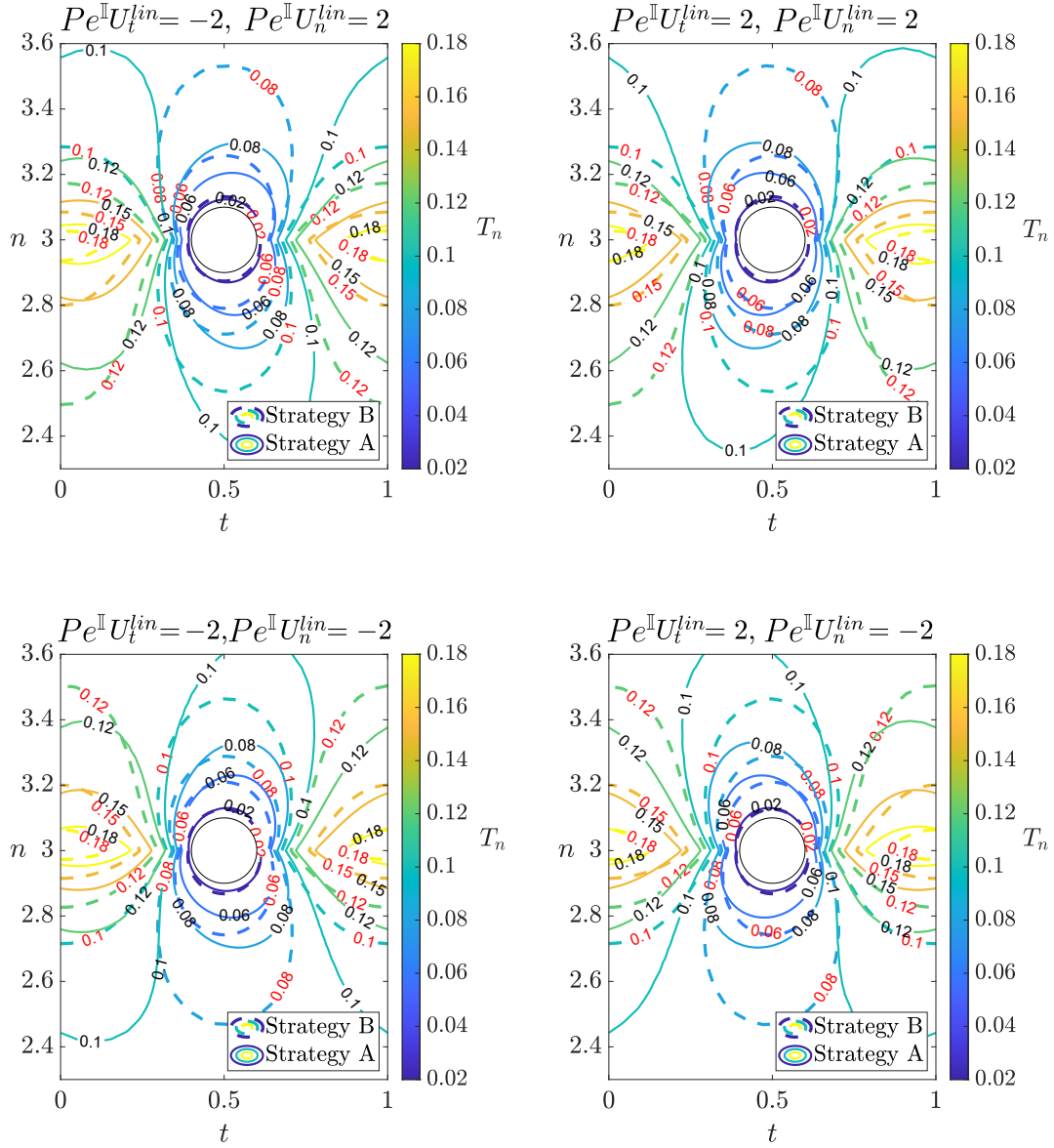


Fig. 3.11: Contours of T_n for $(U_t, U_n) = (\pm 2, \pm 2)$. The red numbers refer to the contours of T_n deduced via strategy B while the black numbers to those deduced from strategy A.

In figure 3.11 the isocontours of T_n within the microscopic elementary cell are represented. We can see the comparison between strategy A and B for $Pe^I U_n = \pm 2$ and $Pe^I U_t = \pm 2$.

3.2 Solution of the macroscopic configuration

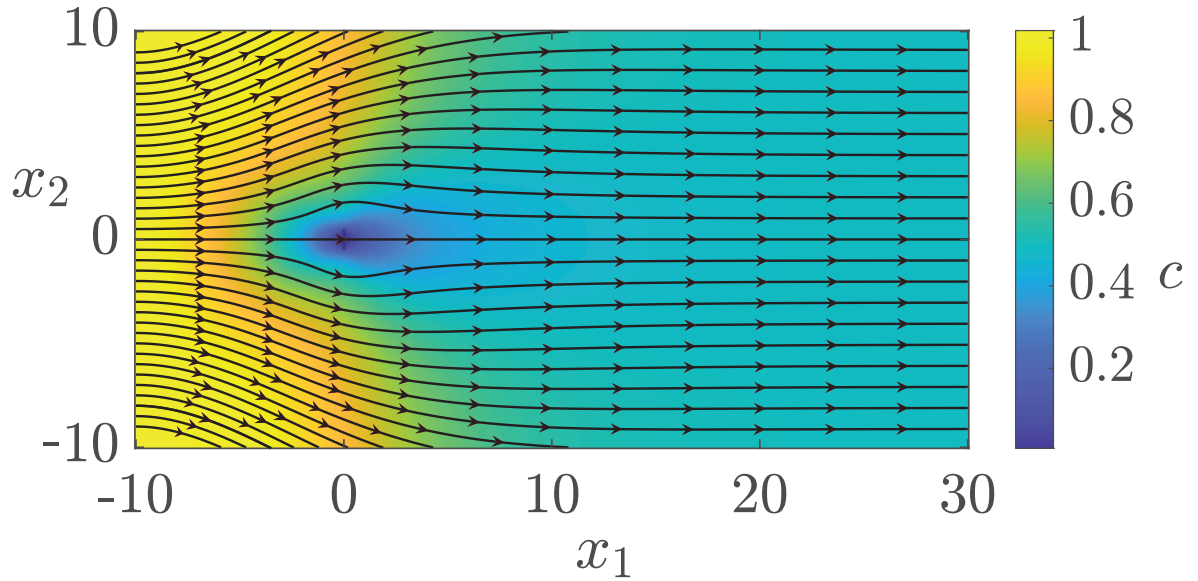


Fig. 3.12: Isocontours of c with flow streamlines (in black) for the diffusive case.

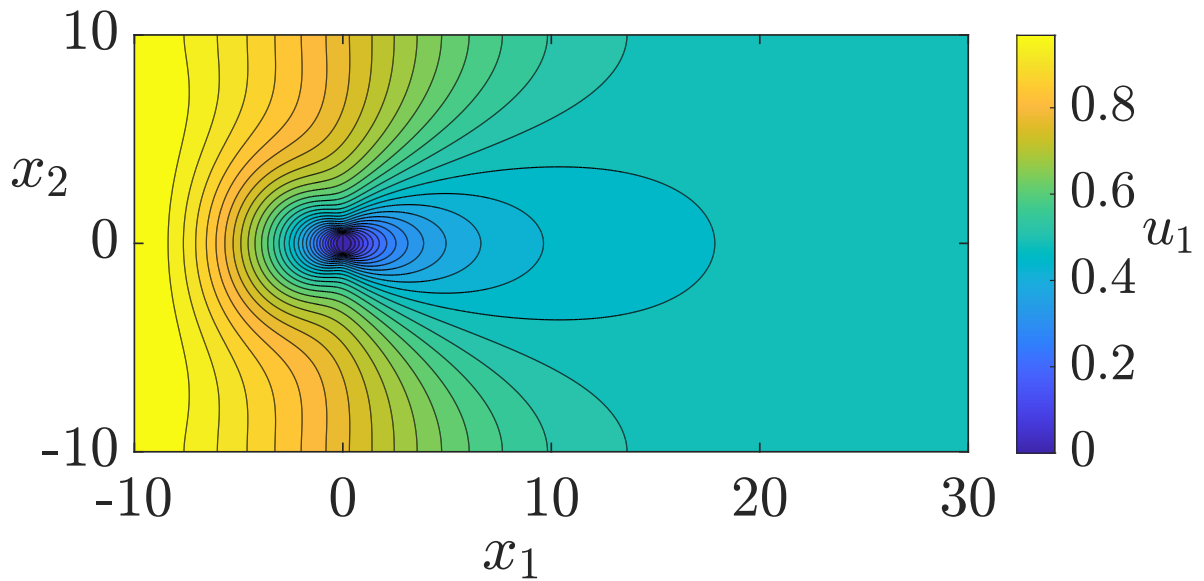


Fig. 3.13: Isocontours of u_1 .

The macroscopic model (2.41) is used to solve for the specific configuration sketched in figure 3.1. The flow fields are sketched within the computational domain in figure 3.12 and 3.13. The results of the macroscopic model (2.41) are compared to the solution of direct numerical simulations (DNS) which provide full-scale flow fields.

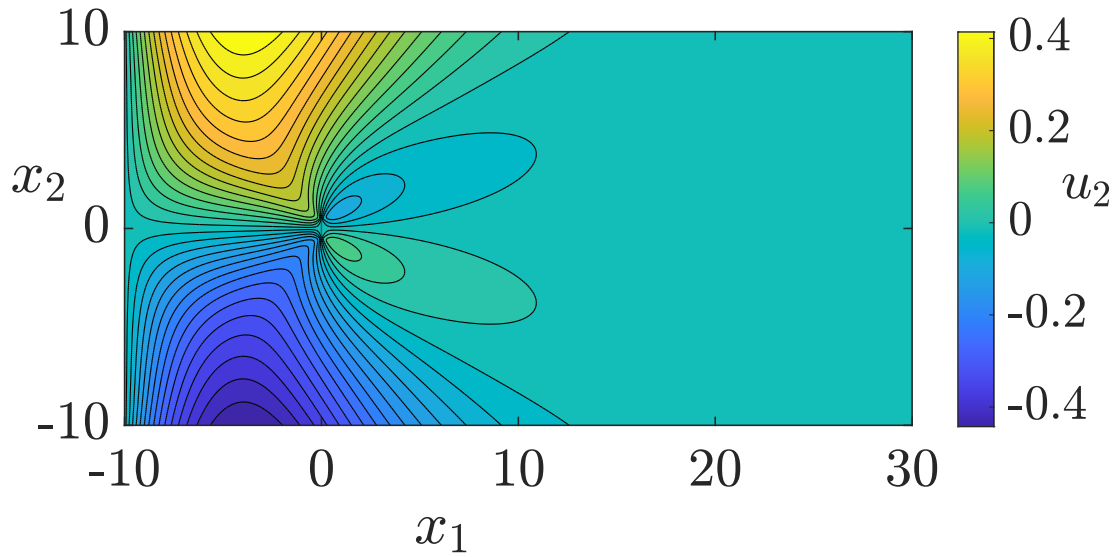


Fig. 3.14: Isocontours of u_2 .

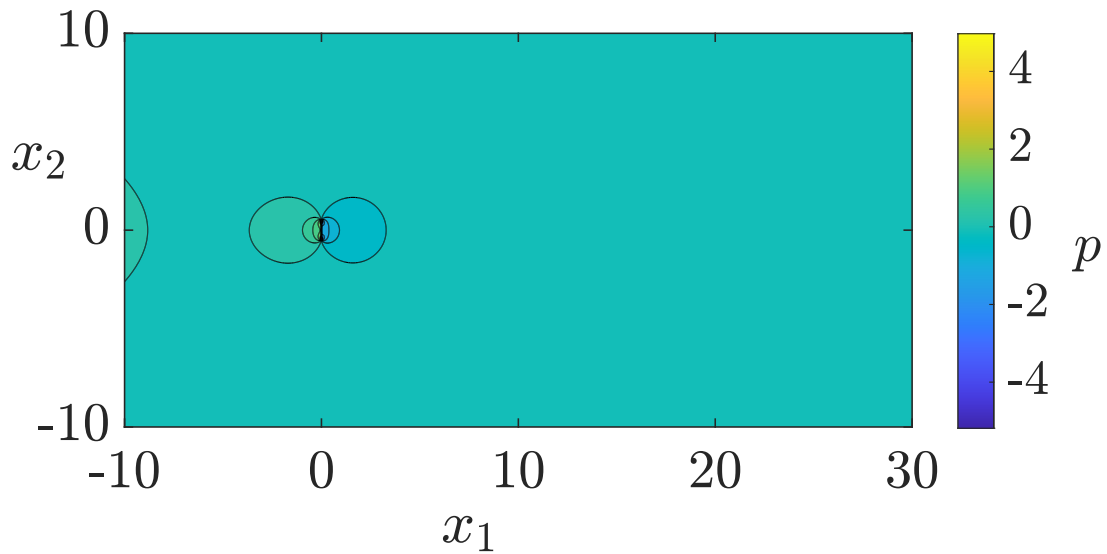


Fig. 3.15: Isocontours of p .

Figures 3.16 and 3.17 depict the horizontal velocity u_1 , the vertical velocity u_2 and the pressure p on the axis $x_2 = 0$ and $x_1 = 0$ respectively. The velocities predicted by the model on the membrane shown in the second line of figure 3.17 are exploited to advect the quantities T_n and Y_n in microscopic problems (2.37). It is important that these quantities match the DNS to predict well the concentration along the membrane. In the following section we show the comparisons regarding the concentration field for $Pe^0 \in \{0, 1/\varepsilon, 1/\varepsilon^2, 2.5/\varepsilon^2, 5/\varepsilon^2, 10/\varepsilon^2, 1/\varepsilon^3\}$.

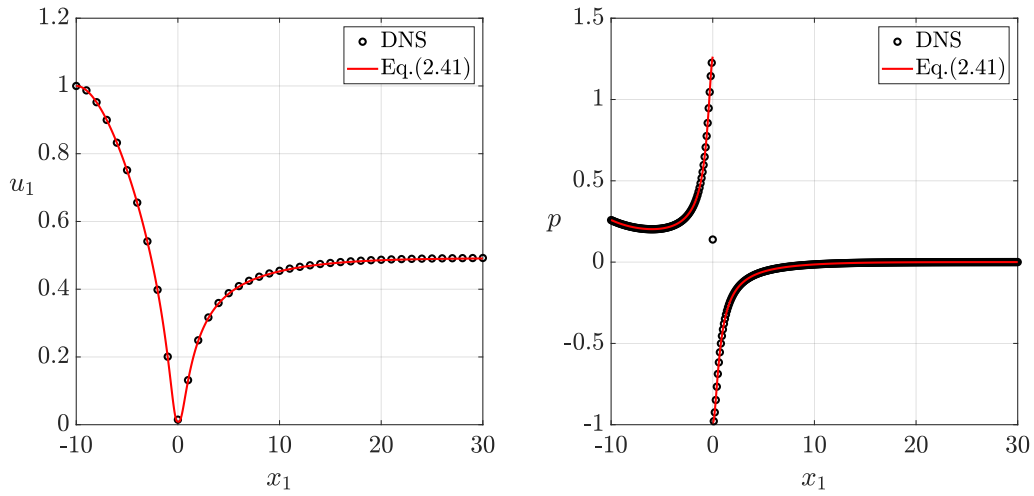


Fig. 3.16: u_1 and p along a horizontal line passing through the center of the membrane, $x_2 = 0$.

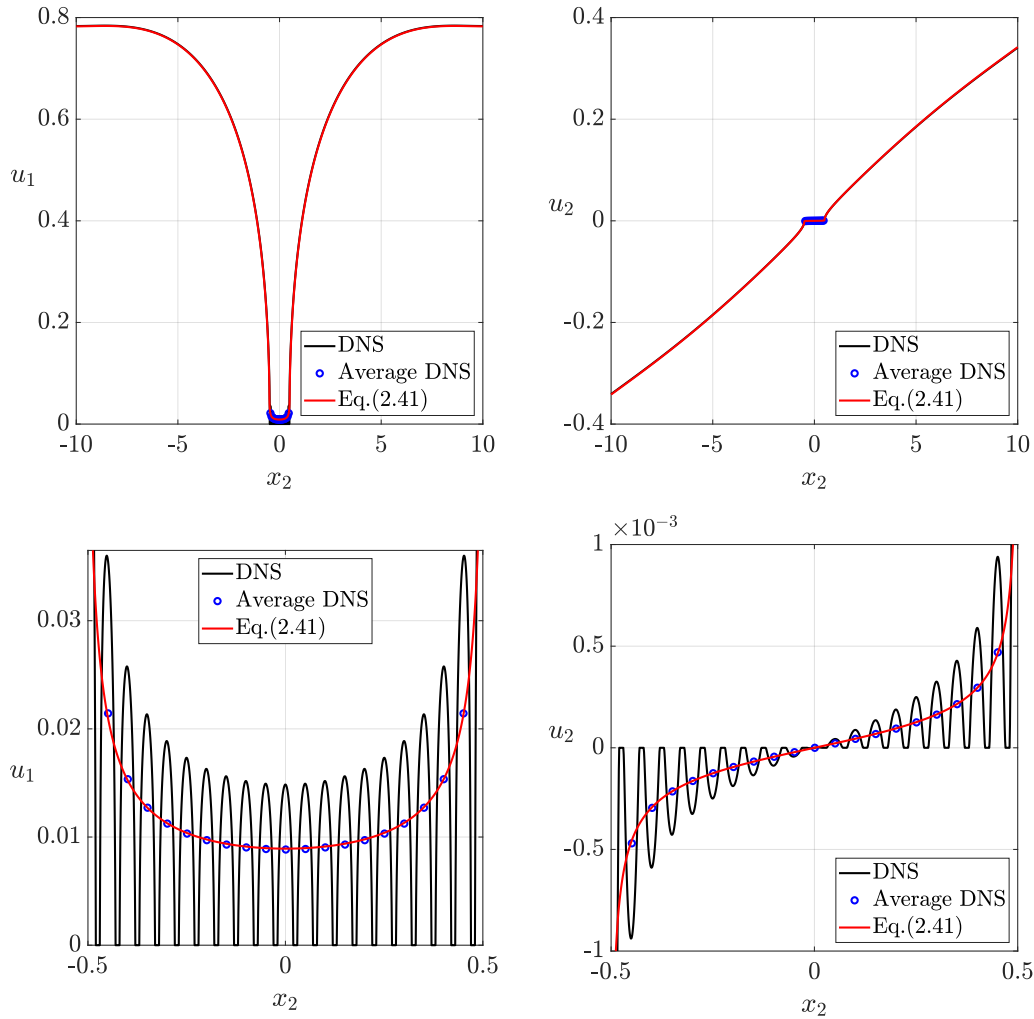


Fig. 3.17: u_1 and u_2 along a vertical line passing through the membrane, $x_1 = 0$. Bottom row: zoom in on the membrane.

3.2.1 Diffusive case

Figure 3.18 shows the values of concentration on the lines $x_2 = 0$ and $x_1 = 0$, while figure 3.19 the values on the membrane \mathbb{C} . In this case $Pe^0 = 0$. The microscopic problem for T_n and Y_n are diffusion problems and the values of the effective diffusion vectors are not affected by the velocity at the membrane.

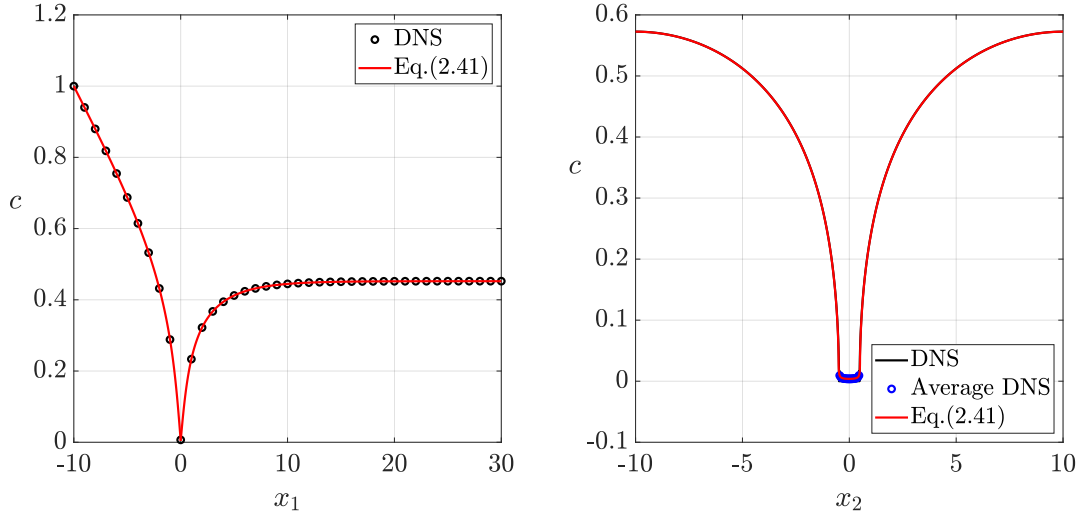


Fig. 3.18: Concentration c sampled on $x_2 = 0$ (left) and $x_1 = 0$ (right).

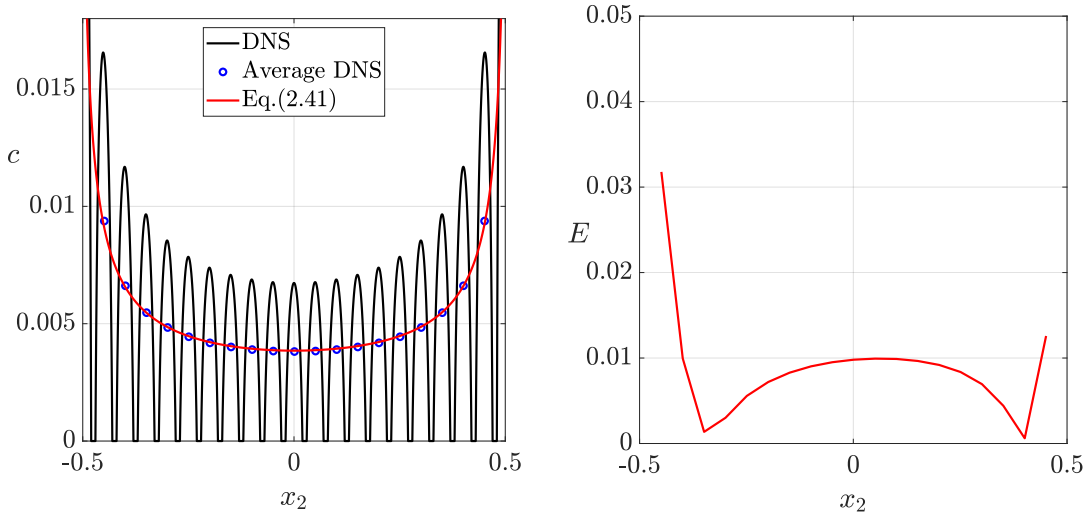


Fig. 3.19: Left frame: concentration c evaluated on \mathbb{C} . Right frame: relative error E along \mathbb{C} .

The model is able to well predict the concentration field in the whole computational domain. The homogenization-based model predict the full-scale field with an error E which is below ε , and is evinced by figure 3.19, right. The error increases at the edges of the membrane. This is due to the fact that the membrane microstructure is not periodic at the edges. The relative error on the membrane is defined as

$$E = \frac{|c_{model} - \bar{c}_{DNS}|}{\frac{c_{model} + \bar{c}_{DNS}}{2}} \quad (3.3)$$

3.2.2 Case $Pe^0 = \frac{1}{\varepsilon}$

The same configuration as in section 3.2.1 is analyzed, with $Pe^0 = \frac{1}{\varepsilon}$. The values of the tensors \mathbf{T} and \mathbf{Y} are obtained along the membrane via the microscopic problems developed in strategy A (section 2.3.1) and strategy C (section 2.3.3).

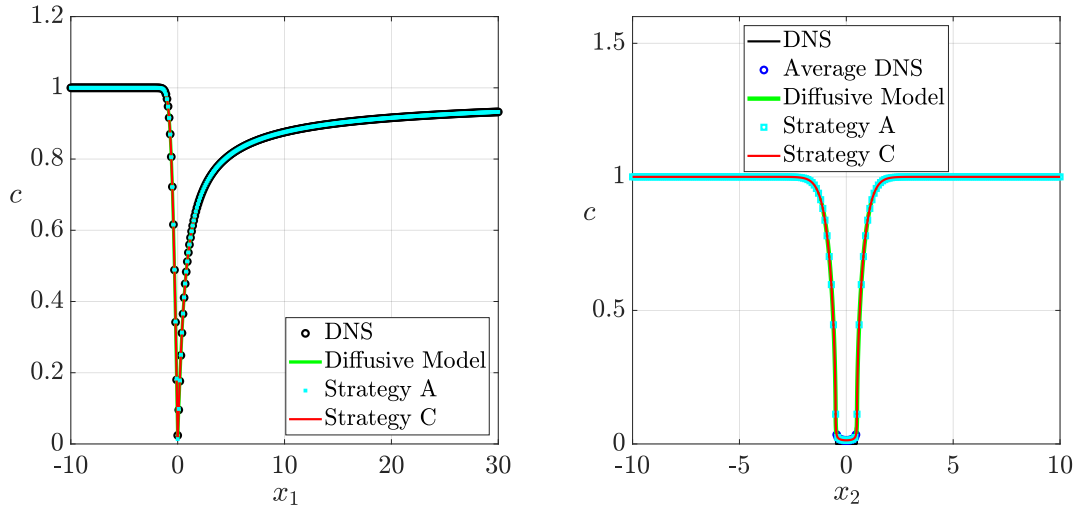


Fig. 3.20: Concentration c sampled on $x_2 = 0$ (left) and $x_1 = 0$ (right).

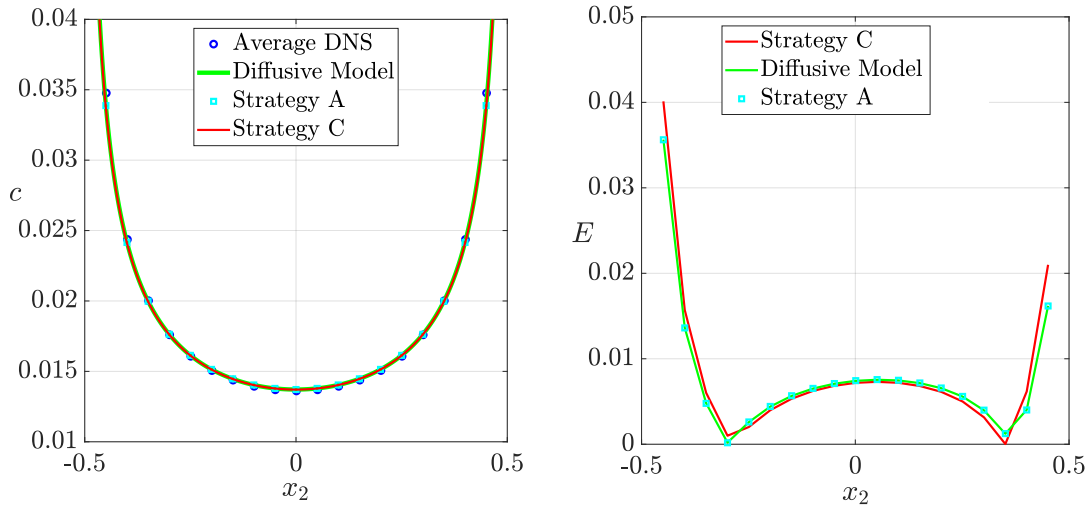


Fig. 3.21: Left frame: concentration c evaluated on \mathbb{C} . Right frame: relative error E along \mathbb{C} .

From now on we name diffusive model, the macroscopic model (2.41) where the tensors \bar{T}_n and \bar{Y}_n are computed using diffusion problems at the microscale and,

hence, assuming $Pe^{\text{I}} = 0$. Despite a $Pe^{\text{O}} = 1/\varepsilon$, Pe^{I} is still small ($\approx 10^{-2}$) and the diffusive model still predicts well the average of the full scale concentration field. All curves are superimposed and the error is within the threshold predicted by the homogenization theory. The results of strategy B are not shown since identical to those of strategy C.

3.2.3 Casel $Pe^{\text{O}} = \frac{1}{\varepsilon^2}$

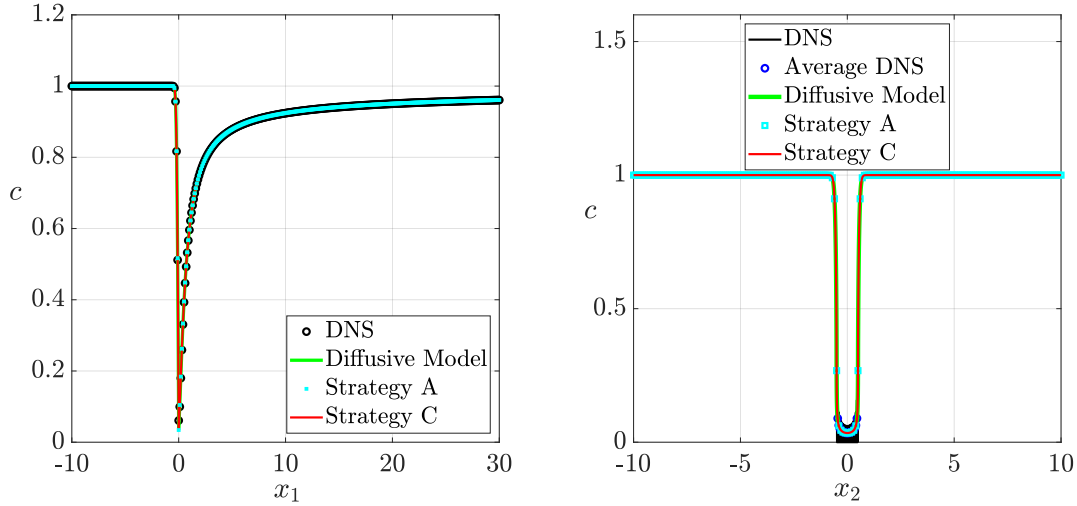


Fig. 3.22: Concentration c sampled on $x_2 = 0$ (left) and $x_1 = 0$ (right).

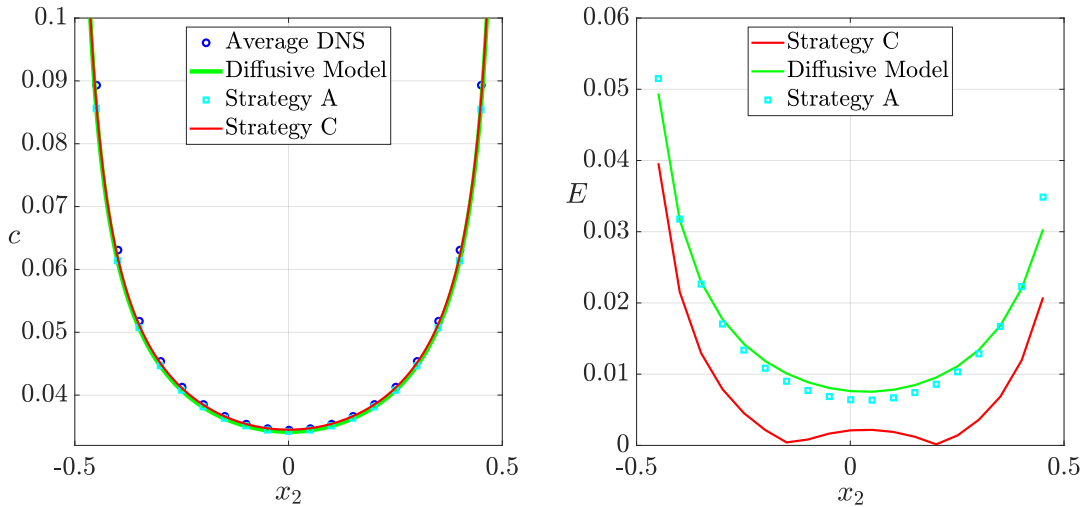


Fig. 3.23: Left frame: concentration c evaluated on \mathbb{C} . Right frame: relative error E along \mathbb{C} .

For this value of the outer Péclet number, $Pe^{\text{I}} \approx 0.2$. The diffusive model predicts the full-scale concentration profile with an acceptable error. Strategy C predicts

the full scale concentration better than strategy A, which behaves similarly to the diffusive case. The results of strategy B are not shown since identical to those of strategy C.

3.2.4 Case $Pe^0 = \frac{2.5}{\varepsilon^2}$ case

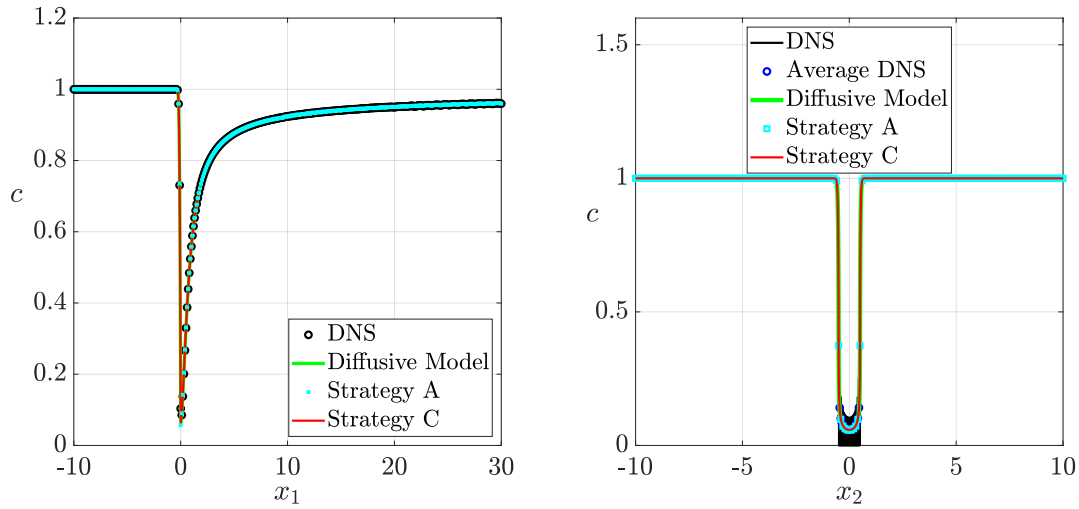


Fig. 3.24: Concentration c sampled on $x_2 = 0$ (left) and $x_1 = 0$ (right).

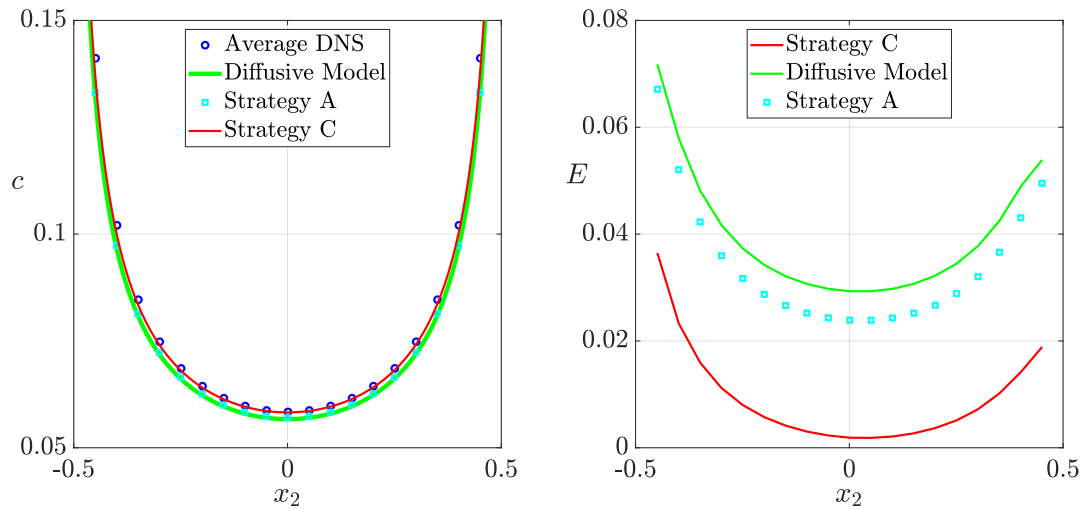


Fig. 3.25: Left frame: concentration c evaluated on \mathbb{C} . Right frame: relative error E along \mathbb{C} .

In this case the inner Péclet number is about 0.5. Strategy C predict very well the concentration along the membrane with an error that is lower than 0.01, while the diffusive model and strategy A have a larger error. The results of strategy B are not shown since identical to those of strategy C.

3.2.5 Case $Pe^0 = \frac{5}{\varepsilon^2}$

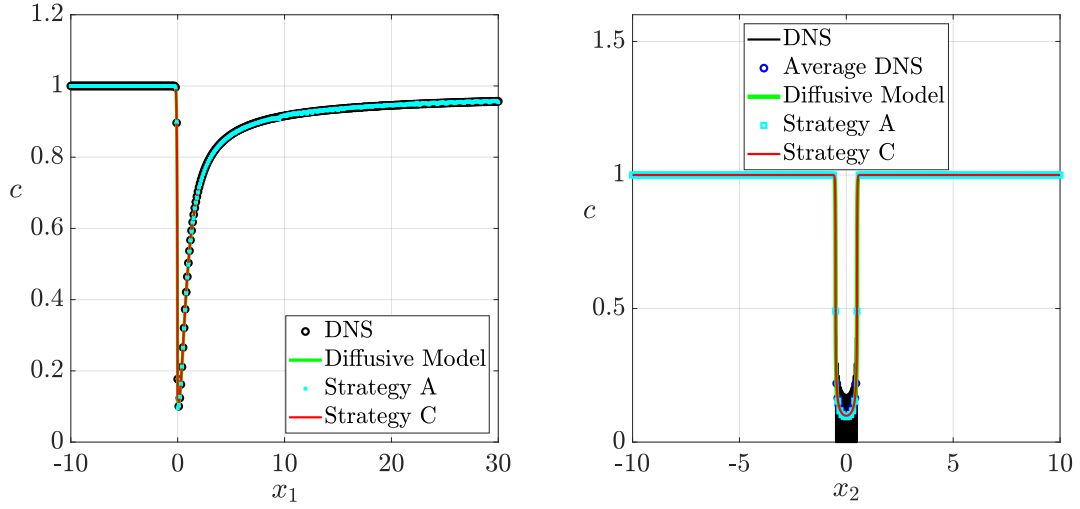


Fig. 3.26: Concentration c sampled on $x_2 = 0$ (left) and $x_1 = 0$ (right).

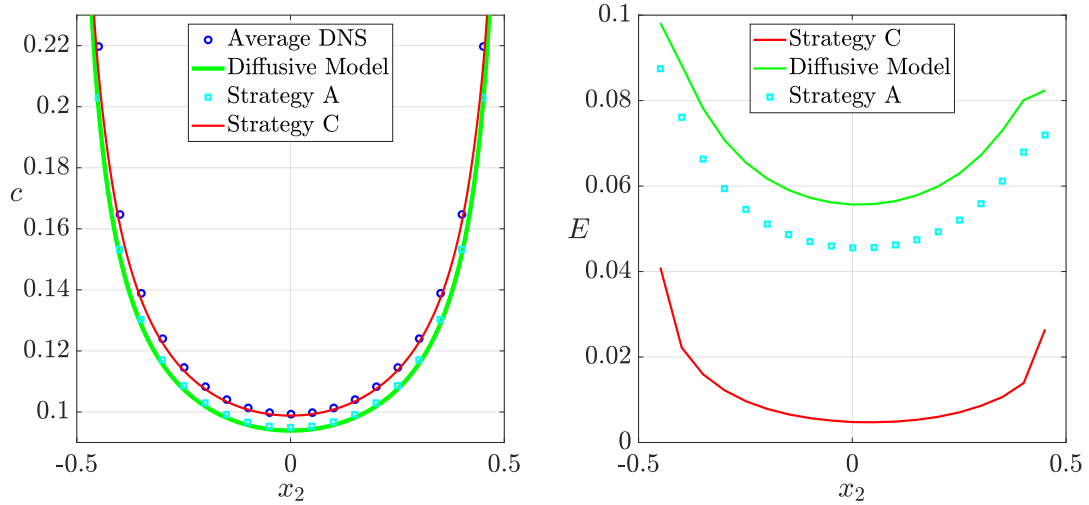


Fig. 3.27: Left frame: concentration c evaluated on \mathbb{C} . Right frame: relative error E along \mathbb{C} .

For this case ($Pe^0 = 2000$, $Pe^I \approx 1$) the diffusion model and strategy A fail to predict the value of c along the membrane. Strategy C instead perform well. The results of strategy B are not shown since identical to those of strategy C.

3.2.6 Case $Pe^{\text{O}} = \frac{10}{\varepsilon^2}$

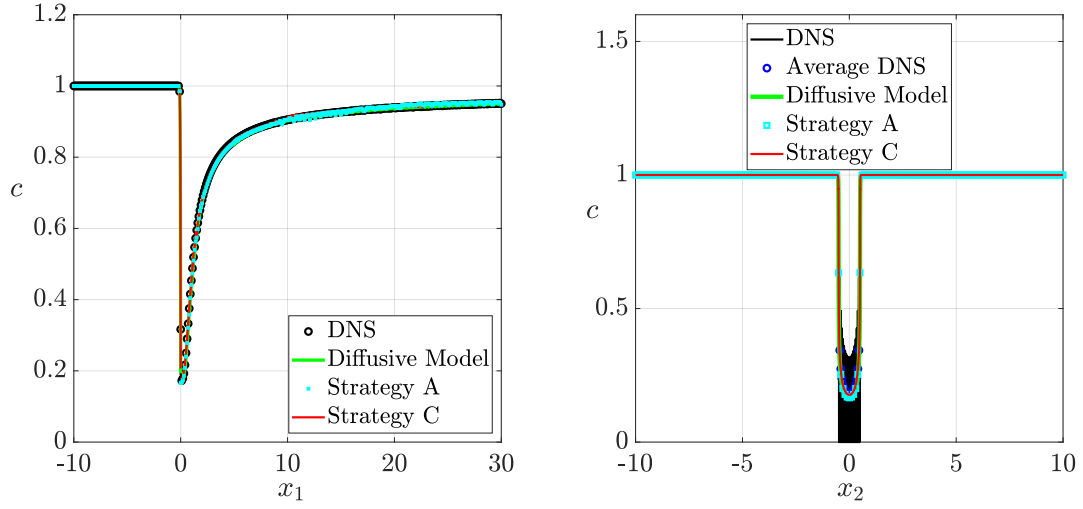


Fig. 3.28: Concentration c sampled on $x_2 = 0$ (left) and $x_1 = 0$ (right).

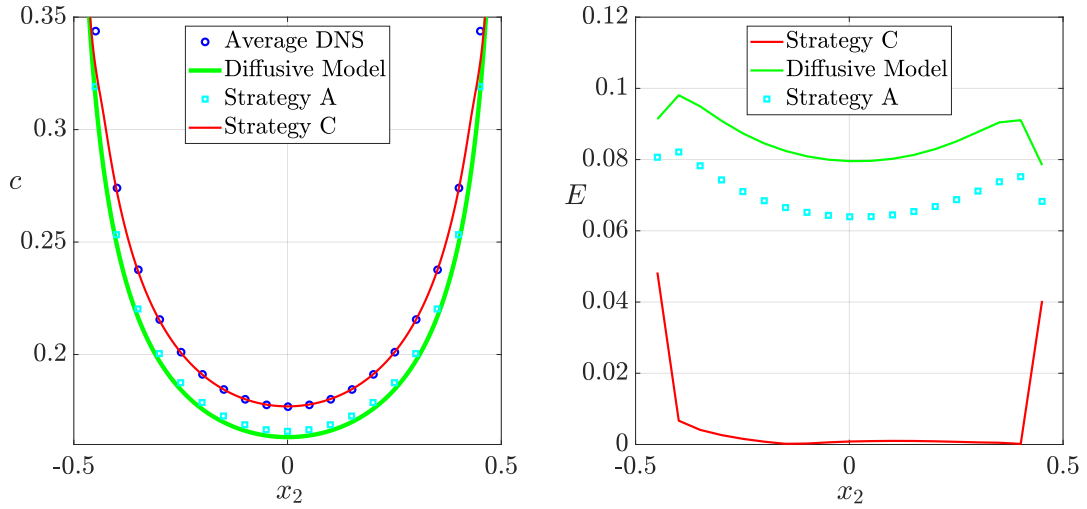


Fig. 3.29: Left frame: concentration c evaluated on \mathbb{C} . Right frame: relative error E along \mathbb{C} .

In this case $Pe^{\text{O}} = 4000$, and $Pe^{\text{I}} \approx 2$. The results show the same trend observed in the previous section. The case of $Pe^{\text{O}} = \frac{1}{\varepsilon^3} = 8000$ and $Pe^{\text{I}} = 5$ is not shown since it follows the same trend. The results of strategy B are not shown since identical to those of strategy C.

3.2.7 Further insights on Pe^{I}

The values of the local Pe^{I} along the membrane are shown here for the cases analyzed before. In figure 3.30 we can see the results for the cases previously studied.

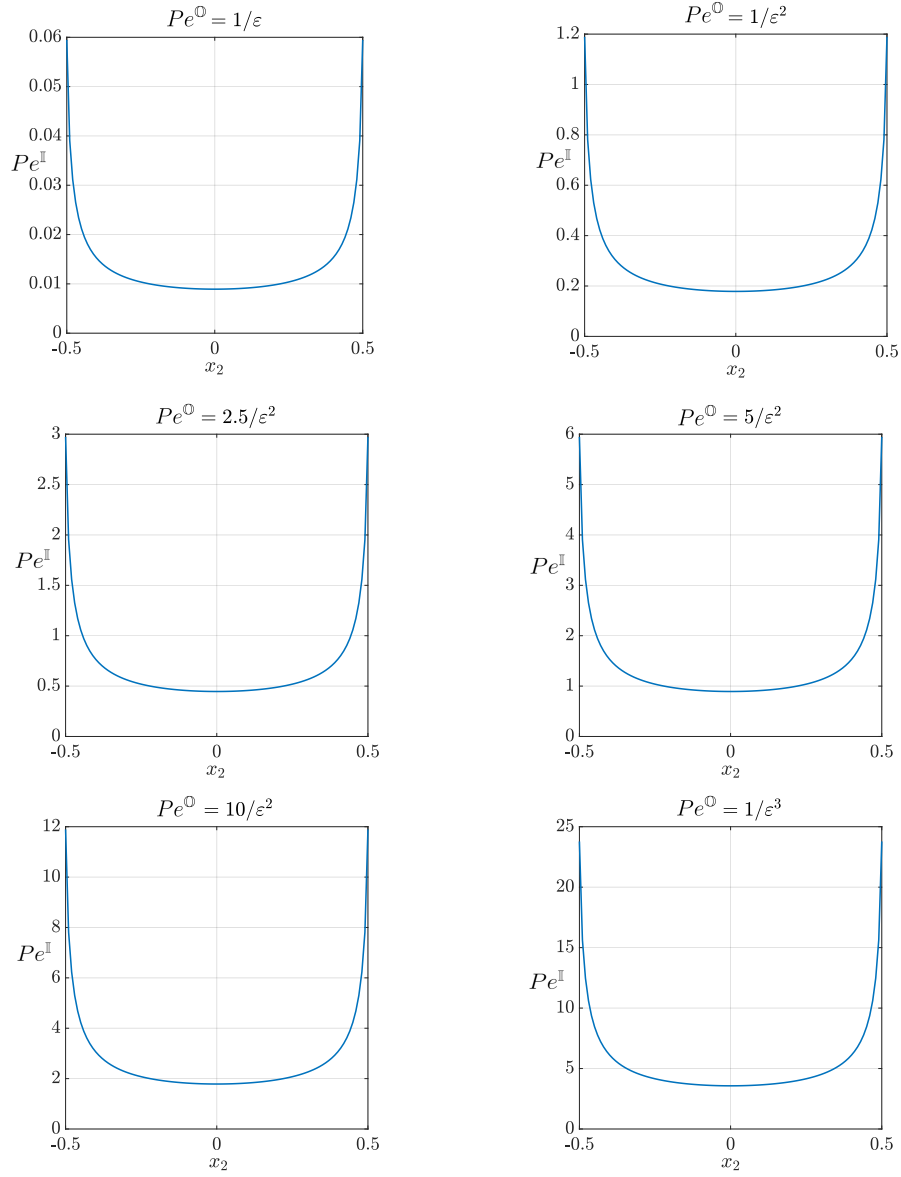


Fig. 3.30: Values of Pe^{I} on the membrane for several values of Pe^{O} .

To better understand how the concentration field is modified by Péclet, a sample of c across four solid inclusions in the middle of the full scale membrane is shown in figure 3.31.

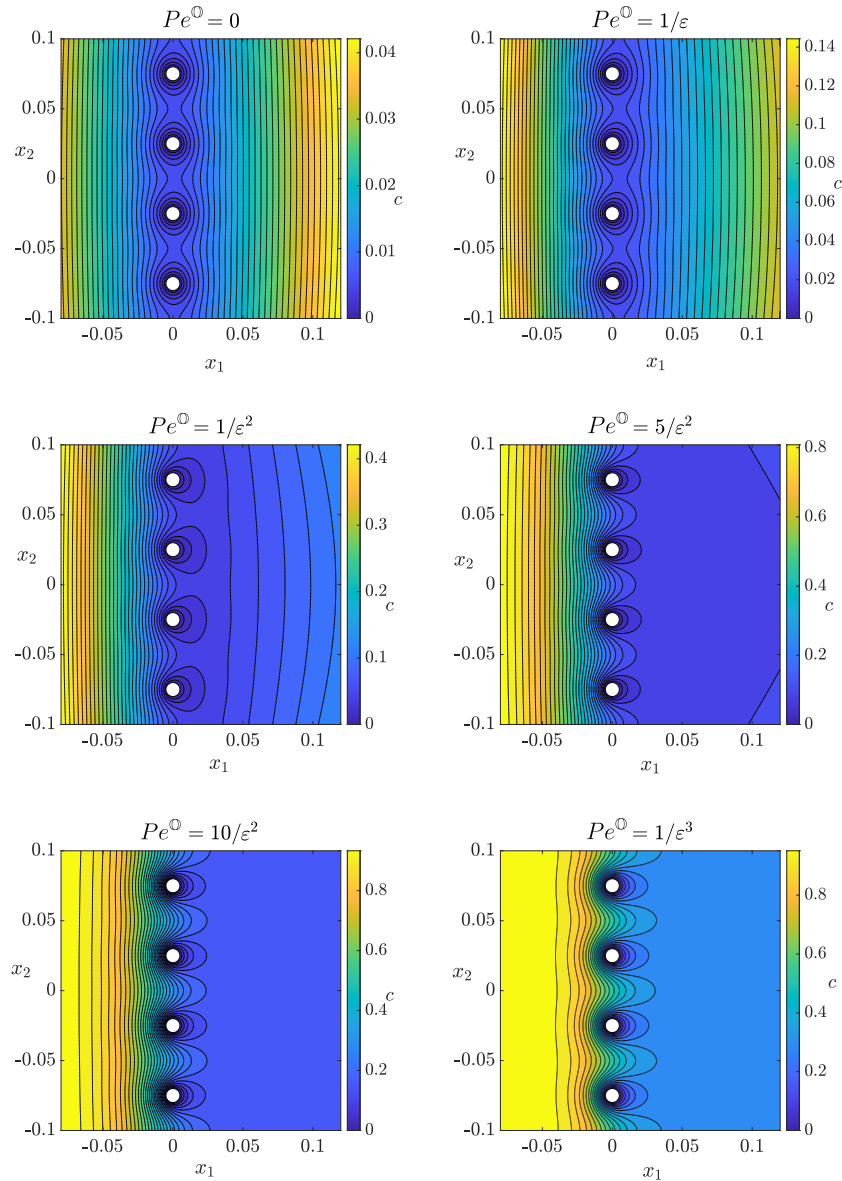


Fig. 3.31: Concentration field within four pores at the center of the full scale membrane.

As the Péclet number is increased, a wake region in the concentration field is generated behind each inclusion, together with an increase of c downstream the membrane. In the upstream region we notice an increase of the gradients approaching the membrane.

To globally quantify the improvement of the approximation developed in strategies B and C, we calculated the root mean square error of c for every Péclet number previously considered.

$$RMS = \sqrt{\frac{\sum_{i=1}^T E_i^2}{T}}, \quad (3.4)$$

where T is the number of inclusions along the membrane and E_i denotes the relative error (3.3) associated to the i^{th} cell forming the membrane. The RMS error is shown in figure 3.32.

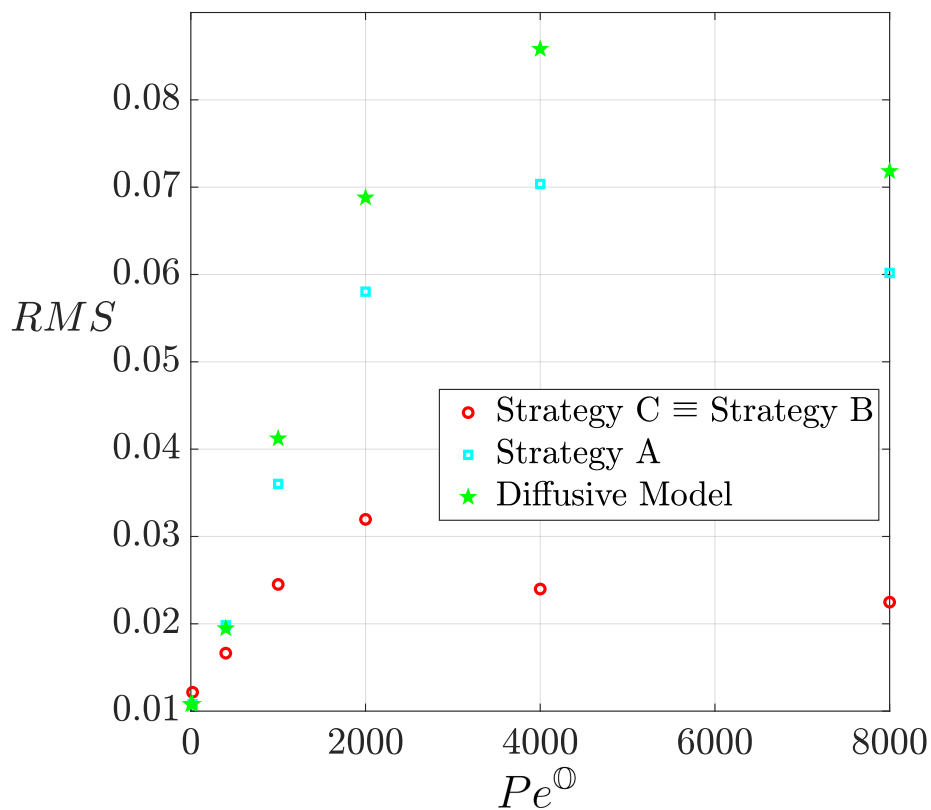


Fig. 3.32: Root mean square error for the the different strategies tested and for several Péclet numbers.

According to the previous analysis, strategy C show a very low error for large Péclet, always below 3.5%.

3.3 Testing other values of the separation of scales parameter

Two different values of ε are chosen to verify the robustness of the model in terms of the geometry of the membrane. Only strategy C is exploited to carry out the macroscopic solution. The geometry of the pores is the same as in the previous solution.

3.3.1 Case $\varepsilon = 0.1$

The membrane is formed by 10 solid inclusions, i.e. $\varepsilon = 0.1$. A larger error is accepted by the homogenization-based model (≈ 0.1).

In figure 3.33 the normal-to-the-membrane velocity u_1 and the tangential one u_2 are represented.

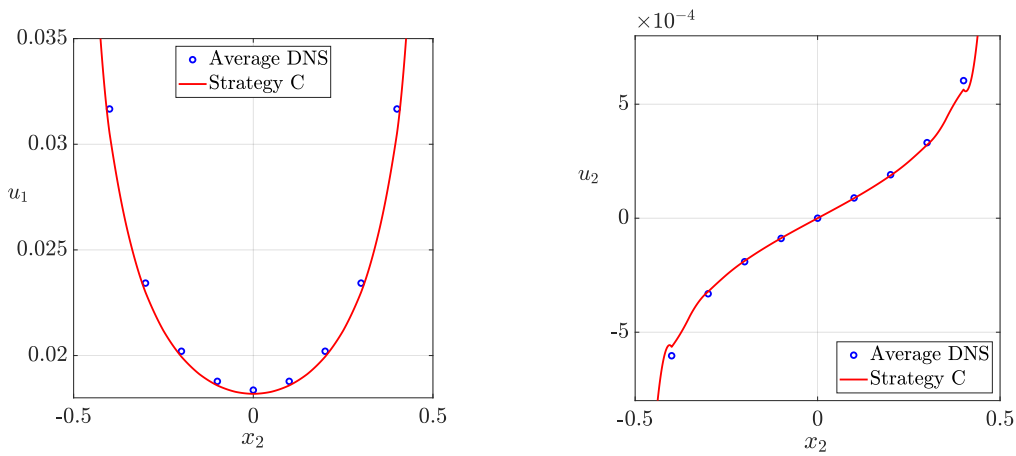


Fig. 3.33: u_1 and u_2 along the membrane \mathbb{C}

The model predicts well the velocities. This is important for the concentration's estimation as previously explained.

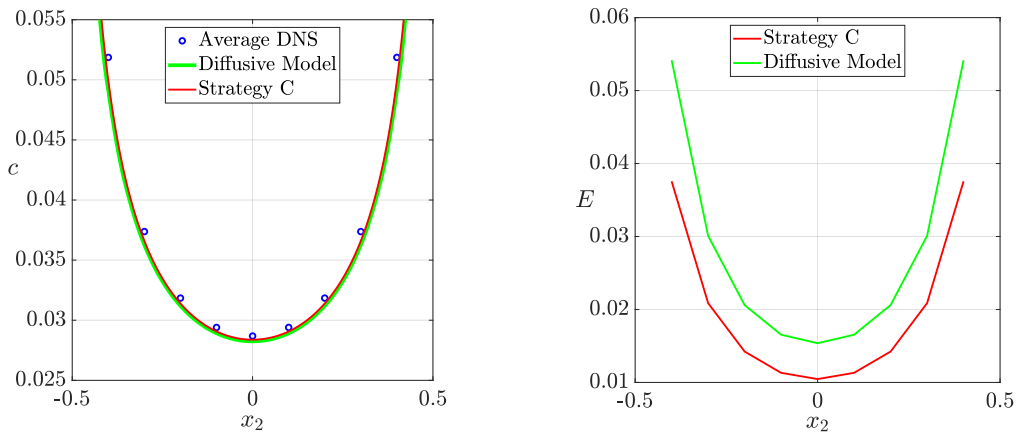


Fig. 3.34: Concentration c (left) and relative error (3.3) (right) along the membrane \mathbb{C} for $Pe^{\circ} = 2/\varepsilon$.

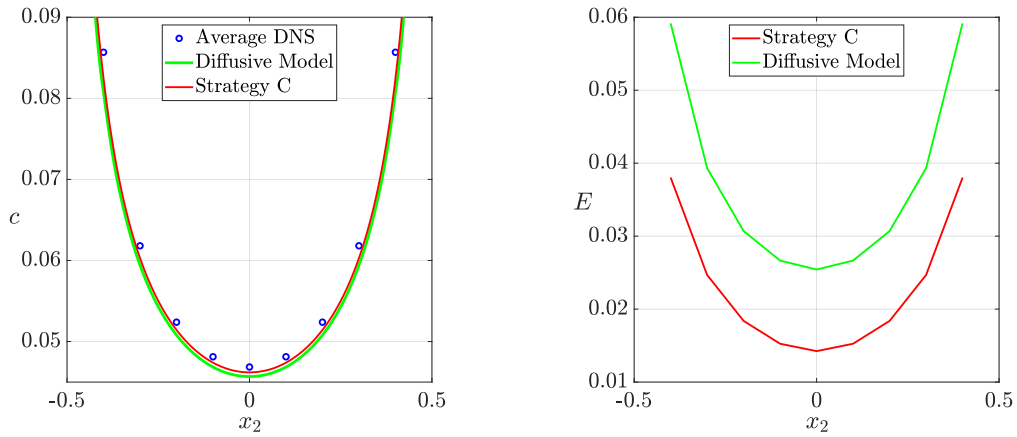


Fig. 3.35: Concentration c (left) and relative error (3.3) (right) along the membrane \mathbb{C} for $Pe^0 = 1/\varepsilon^2$.

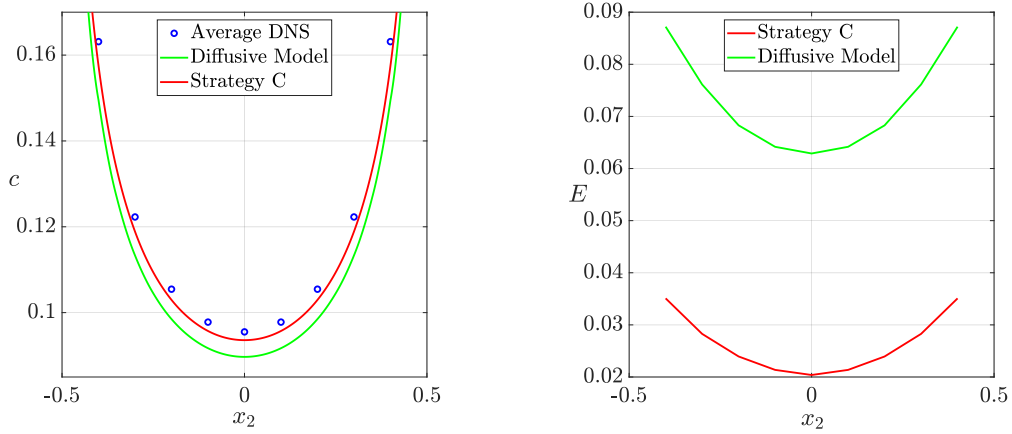


Fig. 3.36: Concentration c (left) and relative error (3.3) (right) along the membrane \mathbb{C} for $Pe^0 = 4/\varepsilon^2$.

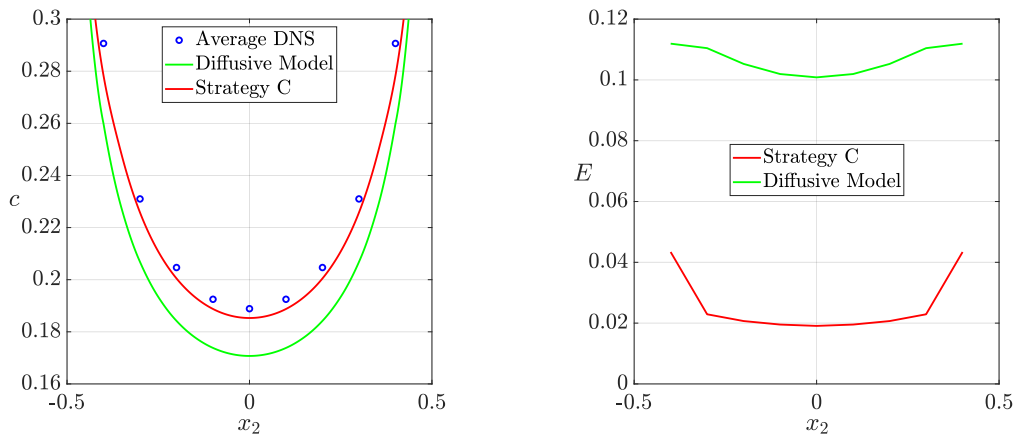


Fig. 3.37: Concentration c (left) and relative error (3.3) (right) along the membrane \mathbb{C} for $Pe^0 = 1/\varepsilon^3$.

The model predicts well the values of concentration for the Pe^0 considered.

The local Pe^{II} values are represented in figure 3.38.

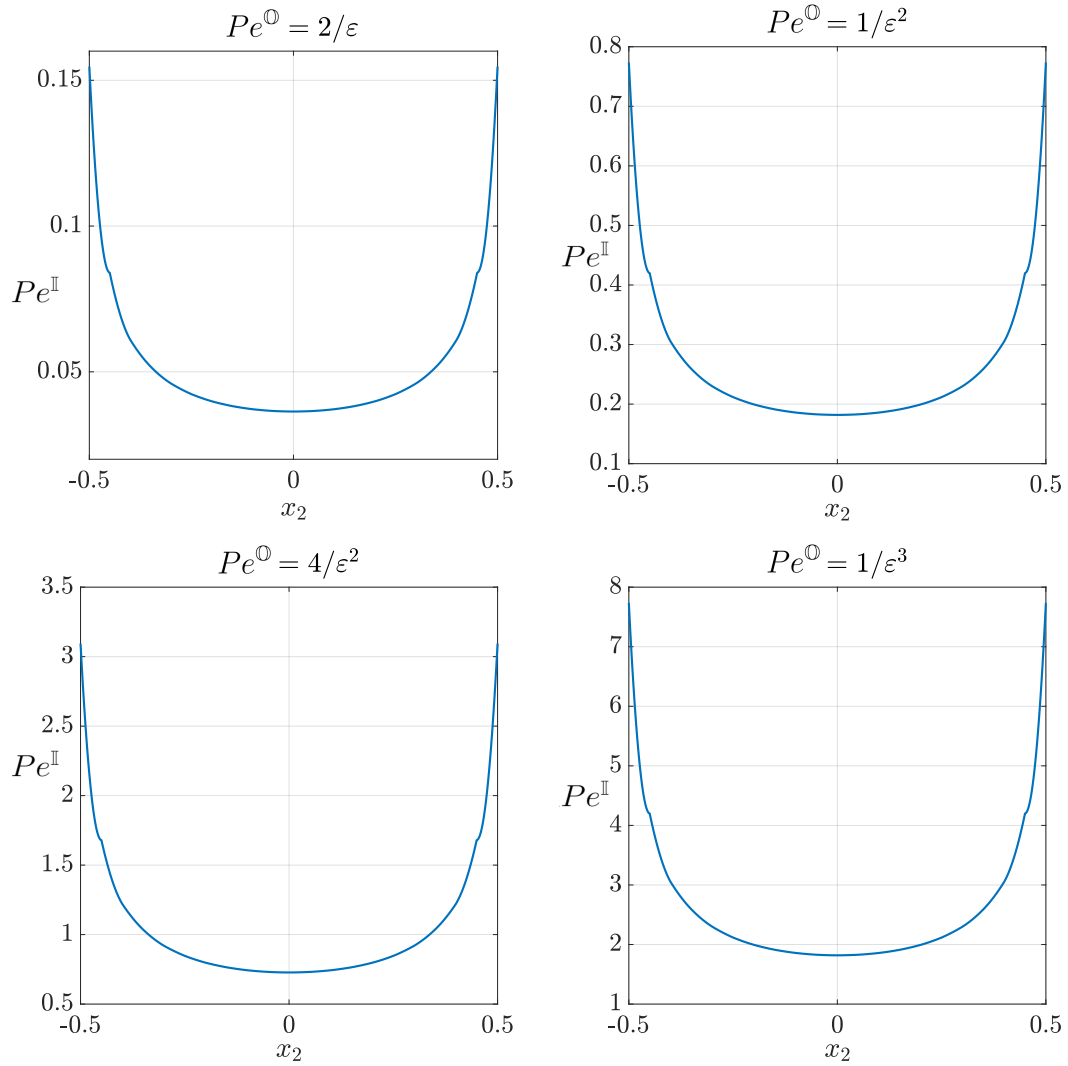


Fig. 3.38: Values of Pe^{II} along the membrane for the Pe^{0} analyzed in the present section.

3.3.2 Case $\varepsilon = 0.01$

We consider a smaller value of $\varepsilon = 0.01$. The full scale simulations have a large computational cost, since the number of pores is increased, while the computational cost for the macroscopic model remain unchanged.

In figure 3.39 the normal and tangential to the membrane velocities u_1 and u_2 are shown.

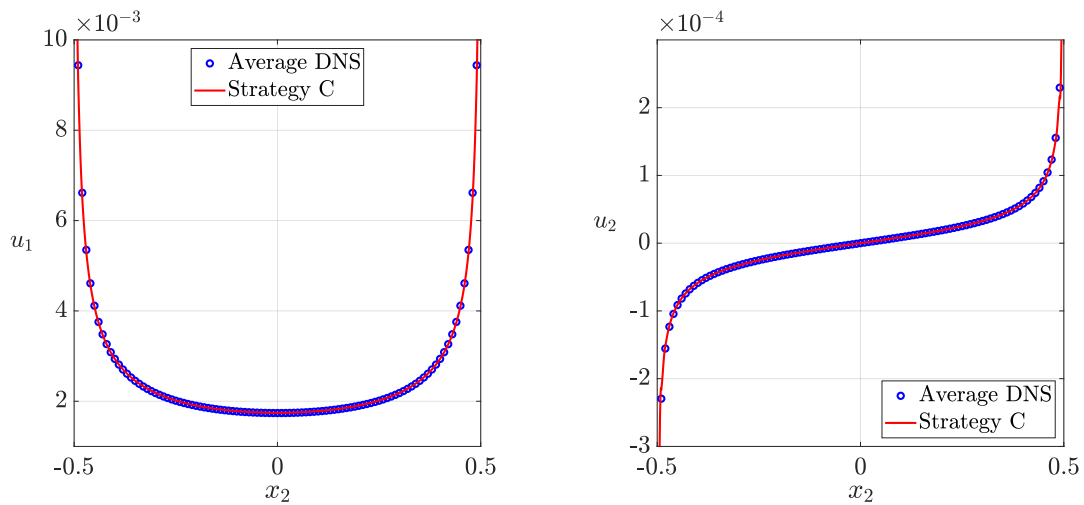


Fig. 3.39: u_1 and u_2 along the membrane \mathbb{C}

Since the values of u_i are small compared to those found for the other ε , it is difficult to obtain large local inner Péclet numbers with the only increase of Pe^\ominus . Alternatively, the Reynolds number is increased in the next section.

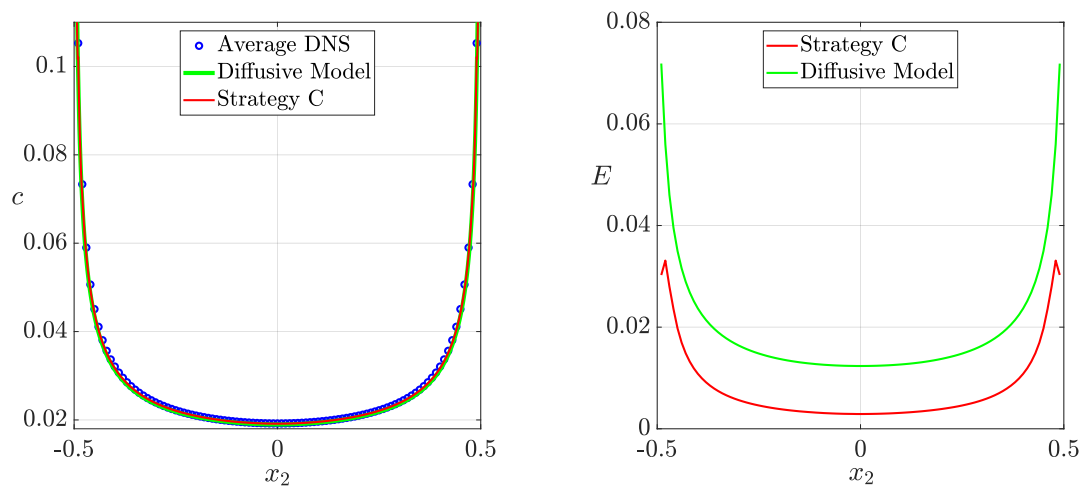


Fig. 3.40: Concentration c (left) and relative error (3.3) (right) along the membrane \mathbb{C} for $Pe^\ominus = 80/\varepsilon$.

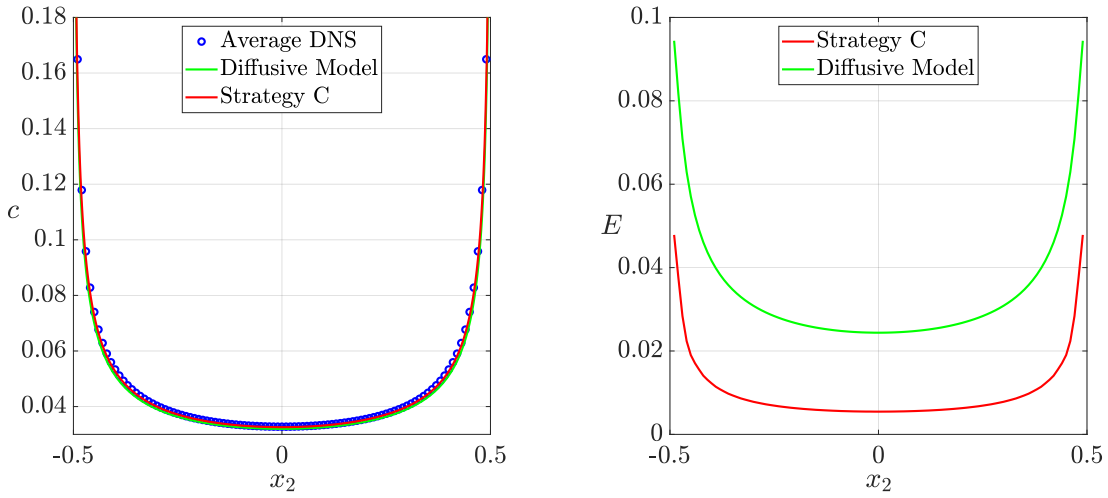


Fig. 3.41: Concentration c (left) and relative error (3.3) (right) along the membrane \mathbb{C} for $Pe^{\text{D}} = 1.6/\varepsilon^2$.

Strategy C well predict the full-scale concentration field and the differences with the diffusive model are quite small, since Pe^{I} is small, as shown in figure 3.42.

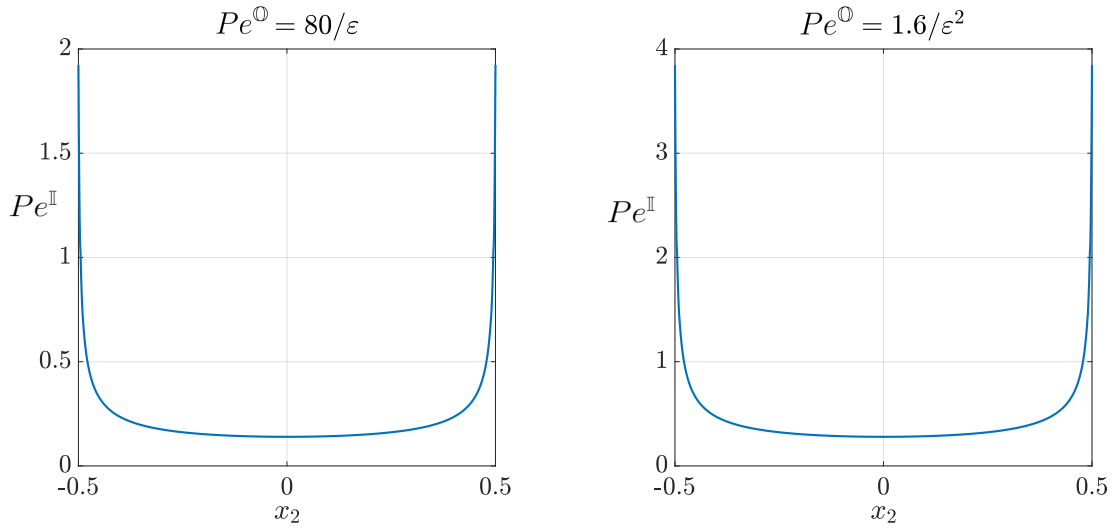


Fig. 3.42: Values of Pe^{I} along the membrane for the Pe^{D} analyzed in the present section

To increase Pe^{I} we increase the Reynolds number in the next section, by observing that $Pe^{\text{I}} = Re^{\text{I}} Sc$, where Sc denotes the Schmidt number, i.e. $Sc = \frac{\mu}{\rho D}$.

3.3.3 Effect of Re° on $Pe^\mathbb{I}$

Until now the inertial term in the Navier-Stokes equations, has been neglected. Here we include inertia to increase the inner Péclet number. We choose four different values of Re° , while in this case Pe° is set to $80/\varepsilon = 8000$.

In figure 3.43 we can see the values of the horizontal velocity u_1 on the membrane for the four cases. An increase of the local membrane velocity implies an increase of $Pe^\mathbb{I}$ at the membrane.

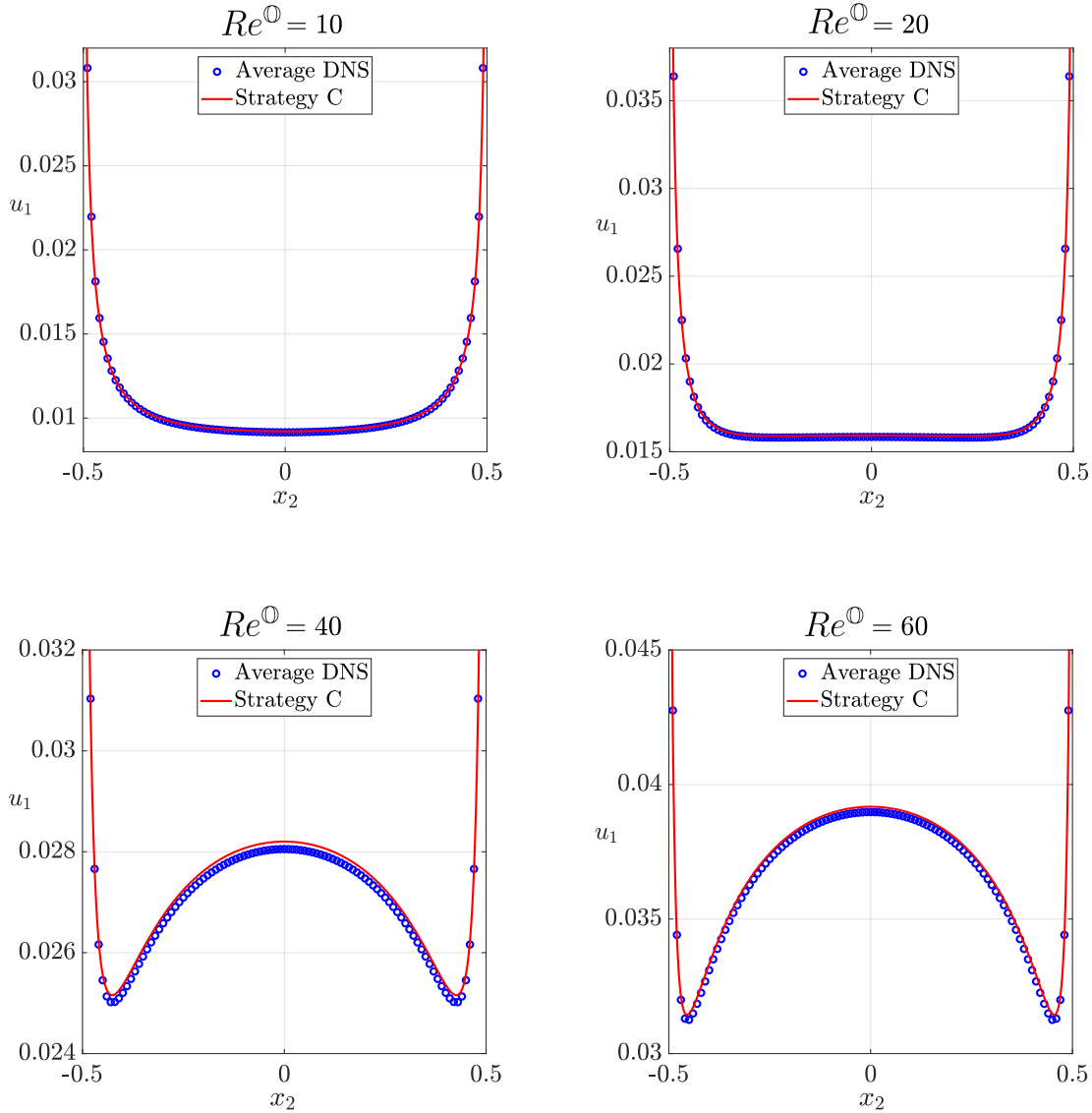


Fig. 3.43: u_1 along the membrane \mathbb{C} for Re° equal to 10, 20, 40 and 60.

The concentration c along the membrane and its relative error is visualized in figures 3.44 to 3.47 for the different Re^{\ominus} considered.

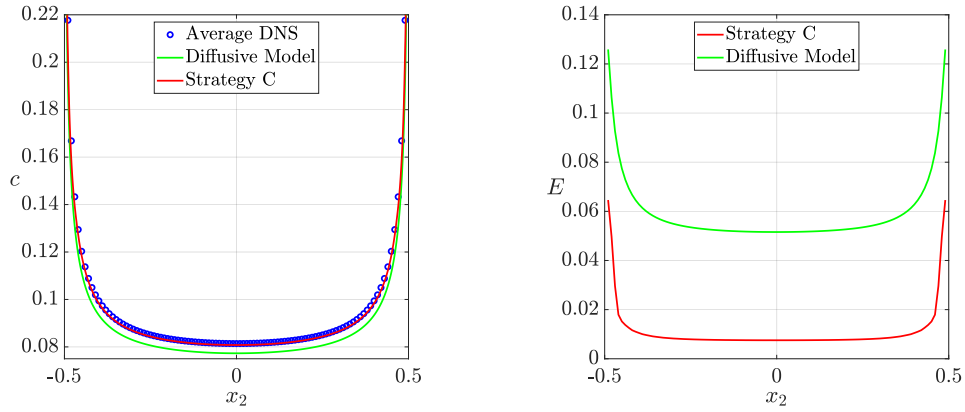


Fig. 3.44: Concentration c (left) and relative error (3.3) (right) along the membrane \mathbb{C} for $Re^{\ominus} = 10$.

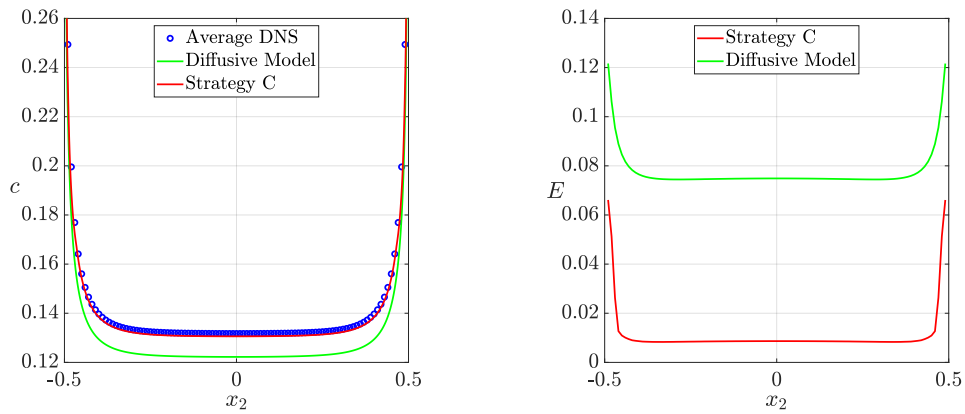


Fig. 3.45: Concentration c (left) and relative error (3.3) (right) along the membrane \mathbb{C} for $Re^{\ominus} = 20$.

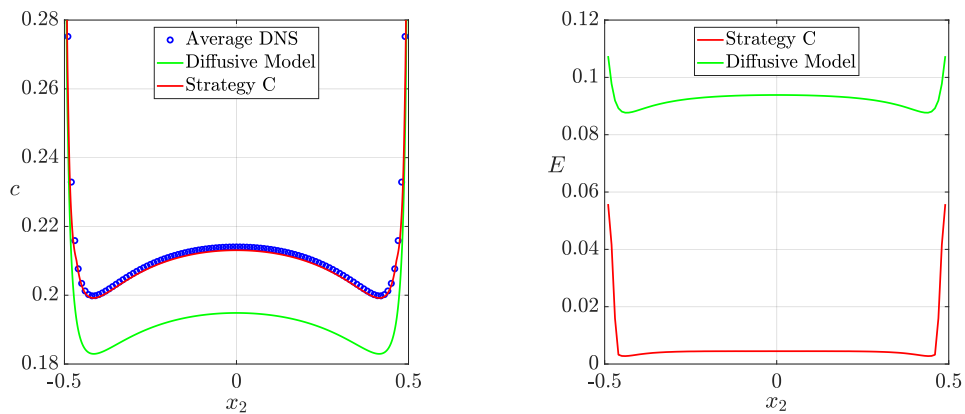


Fig. 3.46: Concentration c (left) and relative error (3.3) (right) along the membrane \mathbb{C} for $Re^{\ominus} = 40$.

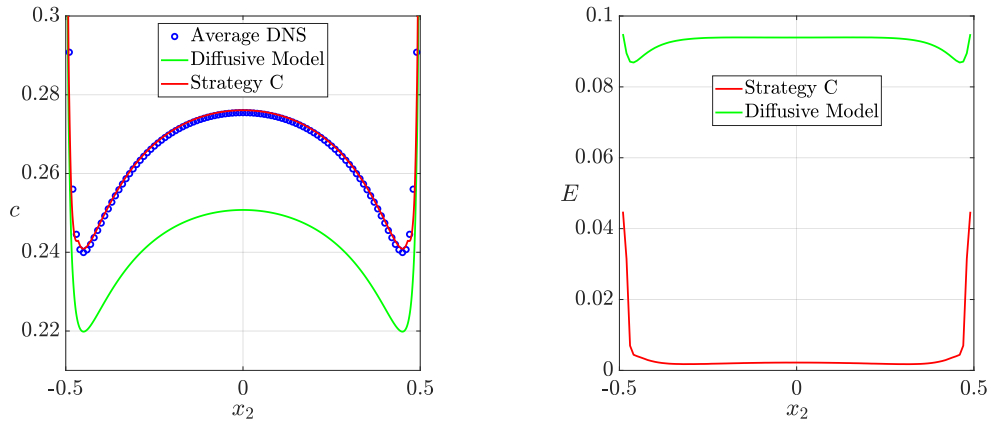


Fig. 3.47: Concentration c (left) and relative error (3.3) (right) along the membrane \mathbb{C} for $Re^{\text{O}} = 60$.

Strategy C correctly predict the values of c for all Re^{O} considered. In figure 3.48 we can see the values of Pe^{I} for the four Re^{O} analyzed.

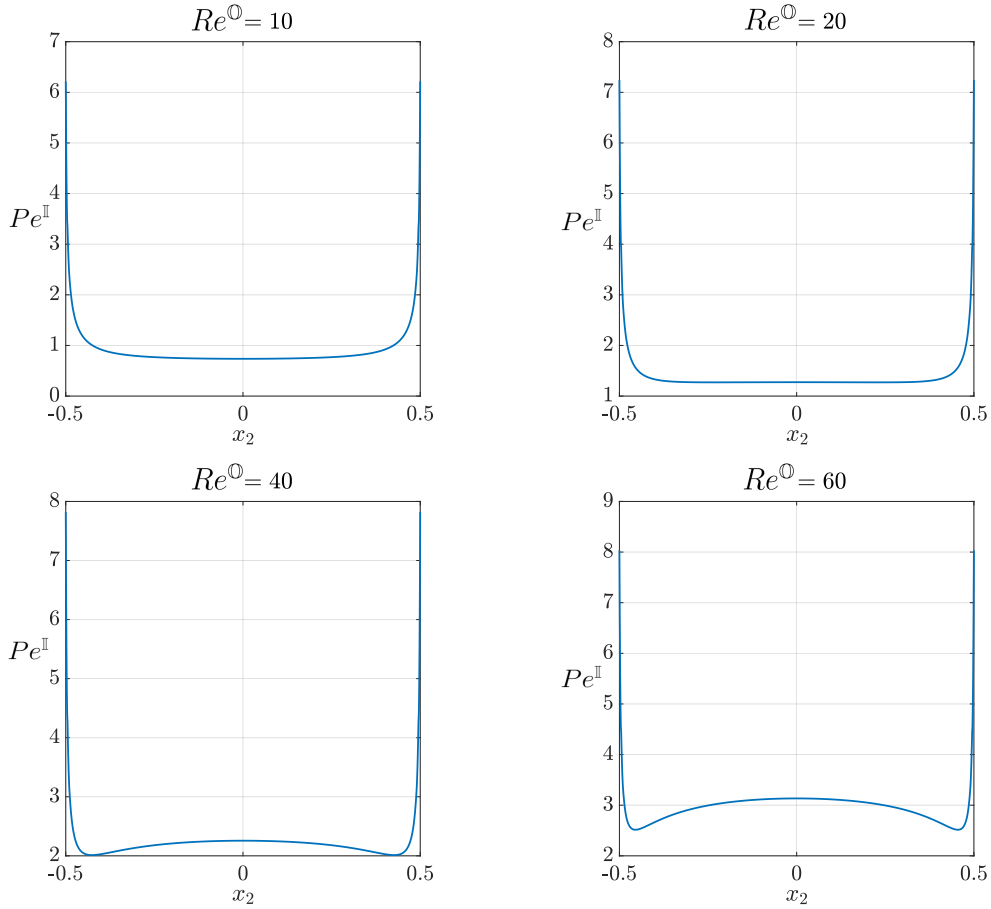


Fig. 3.48: Values of Pe^{I} on the membrane \mathbb{C} for Re^{O} equal to 10, 20, 40 and 60.

As said before, the local inner Péclet number is increased till a value of 3. This shows the robustness of strategy C for finite inner Péclet numbers.

4 Flow past a cylindrical membrane

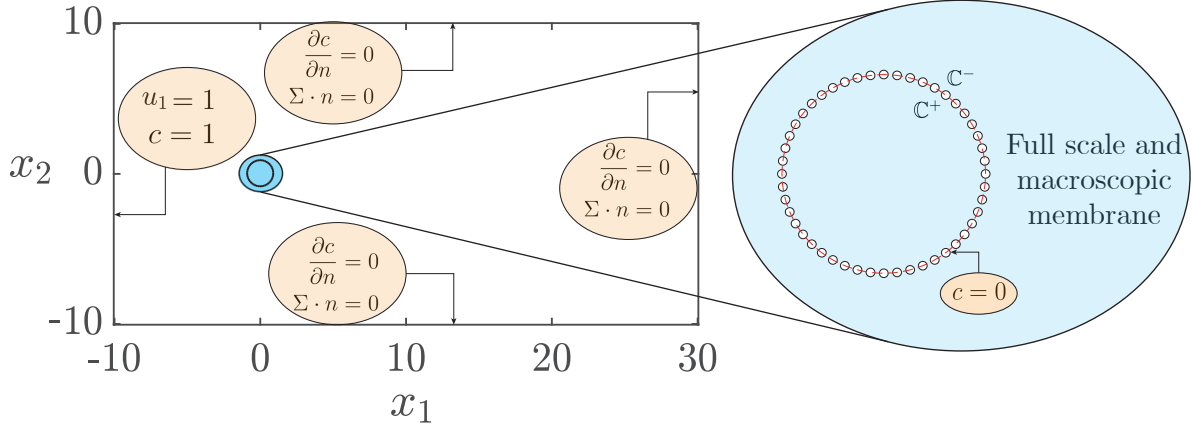


Fig. 4.1: Macroscopic domain and microscopic geometry. Boundary conditions are highlighted in orange. In the right inset the macroscopic equivalent membrane \mathbb{C} is depicted in red and replaces the solid membrane inclusions which are present in the full-scale simulation.

We finally test our approach for a different flow configuration, characterized by a different microscopic and macroscopic geometry. In figure 4.1 the fluid domain is shown with the boundary conditions employed on the boundaries of the computational domain. The membrane is a 2D cylinder containing 48 cylindrical inclusions of radius $0.25l$. The separation of scales parameter ε is equal to 0.13. In the case of the cylindrical membrane, a projection of the local frame on the absolute one is needed. The Navier tensors in Cartesian coordinates are defined as follows,

$$\begin{aligned} M_{ijk} &= \overline{M}_{ttn} \mathbf{t} \wedge \mathbf{t} \wedge \mathbf{n} + \overline{M}_{tnn} \mathbf{t} \wedge \mathbf{n} \wedge \mathbf{n} + \overline{M}_{ntn} \mathbf{n} \wedge \mathbf{t} \wedge \mathbf{n} + \overline{M}_{nnn} \mathbf{n} \wedge \mathbf{n} \wedge \mathbf{n} \\ N_{ijk} &= \overline{N}_{ttn} \mathbf{t} \wedge \mathbf{t} \wedge \mathbf{n} + \overline{N}_{tnn} \mathbf{t} \wedge \mathbf{n} \wedge \mathbf{n} + \overline{N}_{ntn} \mathbf{n} \wedge \mathbf{t} \wedge \mathbf{n} + \overline{N}_{nnn} \mathbf{n} \wedge \mathbf{n} \wedge \mathbf{n}, \end{aligned} \quad (4.1)$$

while the vectors \mathbf{T} and \mathbf{Y} are written as

$$\begin{aligned} T_i &= \overline{T}_n \mathbf{n} \\ Y_i &= \overline{Y}_n \mathbf{n}, \end{aligned} \quad (4.2)$$

where $\mathbf{n} = (0, \cos(\alpha), \sin(\alpha))$, $\mathbf{t} = (0, -\cos(\alpha), \sin(\alpha))$ and $\alpha = \tan^{-1}(y/x)$. The symbol \wedge denotes the inner product $\mathbf{a} \wedge \mathbf{b} := a_i b_j$. This lead to full Navier tensors and effective diffusion vectors.

4.1 Accounting for discontinuities at the membrane

Strategy C is used for the microscopic problems. Two spatial averages are introduced to allow discontinuities across the membrane, replacing the average (2.38) in the upscaling step which lead to the macroscopic model (2.41). The upward and downward averages are computed in the positive and negative far-field, i.e.

$$\cdot^{\mathbb{U}} = \lim_{x'_n \rightarrow +\infty} \frac{1}{\mathbb{U}} \int_{\mathbb{U}} \cdot dx'_s dx'_t - x'_n, \quad \cdot^{\mathbb{D}} = \lim_{x'_n \rightarrow -\infty} \frac{1}{\mathbb{D}} \int_{\mathbb{D}} \cdot dx'_s dx'_t - x'_n, \quad (4.3)$$

The new averages lead to new interface conditions valid on the membrane \mathbb{C}

$$\begin{cases} \overline{u}_i^{\text{U}} = \varepsilon(\overline{M}_{ijk}^{\text{U}} \Sigma_{jk}^{\text{O},\text{C}^-} + \overline{N}_{ijk}^{\text{U}} \Sigma_{jk}^{\text{O},\text{C}^+}) \\ \overline{u}_i^{\text{D}} = \varepsilon(\overline{M}_{ijk}^{\text{D}} \Sigma_{jk}^{\text{O},\text{C}^-} + \overline{N}_{ijk}^{\text{D}} \Sigma_{jk}^{\text{O},\text{C}^+}) \end{cases} \quad (4.4)$$

$$\begin{cases} \overline{c}^{\text{U}} = \varepsilon(\overline{T}_i^{\text{U}} F_i^{\text{O},\text{C}^-} + \overline{Y}_i^{\text{U}} F_i^{\text{O},\text{C}^+}) \\ \overline{c}^{\text{D}} = \varepsilon(\overline{T}_i^{\text{D}} F_i^{\text{O},\text{C}^-} + \overline{Y}_i^{\text{D}} F_i^{\text{O},\text{C}^+}) . \end{cases} \quad (4.5)$$

$\overline{M}_{ijk}^{\text{U}}$ and $\overline{N}_{ijk}^{\text{U}}$ quantifies the effect of the membrane on the solvent in the upwind region due to an upward and downward stress, while $\overline{M}_{ijk}^{\text{D}}$ and $\overline{N}_{ijk}^{\text{D}}$ estimate the same effects for the flow in the downstream. Instead, $\overline{T}_n^{\text{U}}$ and $\overline{Y}_n^{\text{U}}$ measure the effects of the upward and downward diffusive fluxes on the upward concentration, while T_n^{D} and Y_n^{D} measure the same effects on the downward solute concentration. $\overline{M}_{nnn}^{\text{U}} = -\overline{N}_{nnn}^{\text{D}}$ since the microscopic flow rate through the periodic unit cell is conserved.

4.2 Microscopic solution

Problems (2.36) and (2.37) have been solved for the specific microscopic geometry introduced in chapter 4, a cylindrical inclusion of diameter equal to $0.5l$. The non-zero components of the tensors \mathbf{M} and \mathbf{N} are represented in figure 4.2 and figure 4.3. The upward and downward averaged values satisfy the relations $\overline{M}_{ttn}^{\text{U}} = -\overline{N}_{ttn}^{\text{D}}$, $\overline{M}_{ttn}^{\text{D}} = -\overline{N}_{ttn}^{\text{U}}$. For further details about the numerical resolution we refer to appendix B.

The upward and downward averages of the components of \mathbf{M} and \mathbf{N} are shown in table 4.2.

Component	Value
$\overline{M}_{nnn}^{\text{U}}$	0.018926
$\overline{N}_{nnn}^{\text{U}}$	-0.018926
$\overline{M}_{ttn}^{\text{U}}$	0.053823
$\overline{N}_{ttn}^{\text{U}}$	0.00057831
$\overline{M}_{nnn}^{\text{D}}$	0.018926
$\overline{N}_{nnn}^{\text{D}}$	-0.018926
$\overline{M}_{ttn}^{\text{D}}$	-0.00057831
$\overline{N}_{ttn}^{\text{D}}$	-0.053823

Tab. 4.1: Non-zero averaged components of the Navier tensor \mathbf{M} and \mathbf{N} .

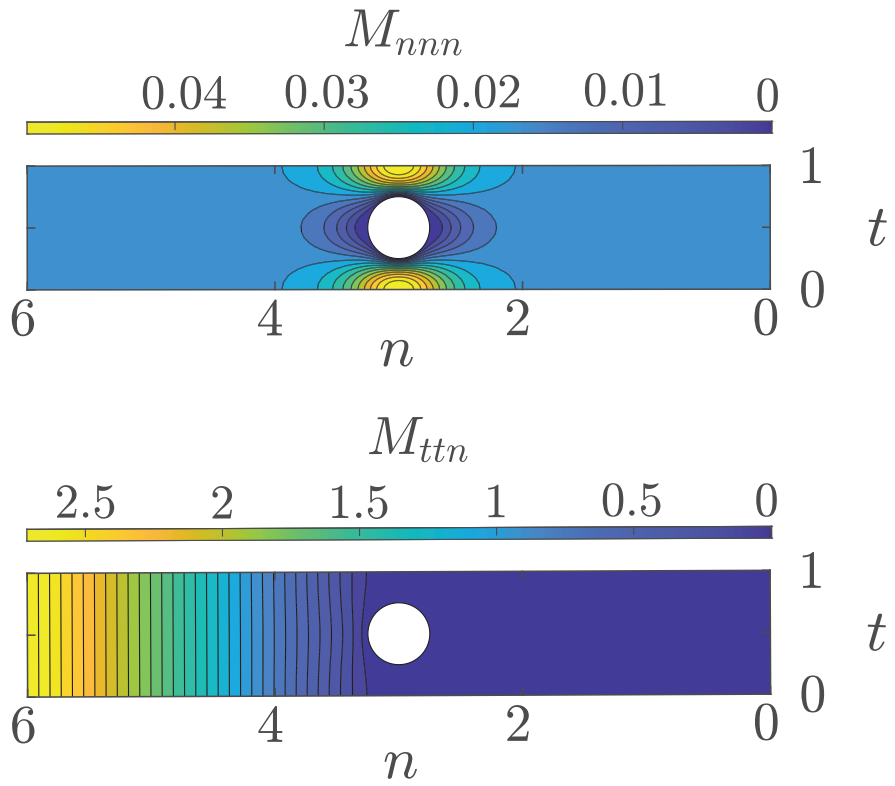


Fig. 4.2: Top frame: isocontours of M_{nnn} . Bottom frame: isocontours of M_{ttn} .

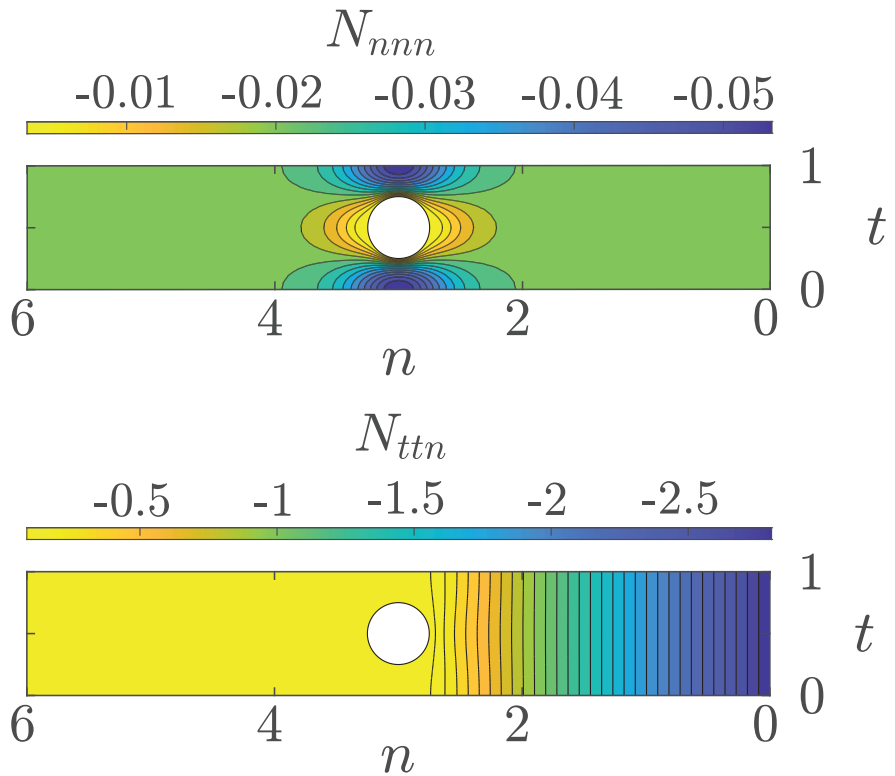


Fig. 4.3: Top frame: isocontours of N_{nnn} . Bottom frame: isocontours of N_{ttn} .

4.2.1 Effective diffusion vectors

The values of the upward and downward averages of T_n and Y_n obtained from the solution of the microscopic problems defined in strategy C (section 2.3.3) are shown in figure 4.4. A monotonic behaviour with S_n for every component is noticed.

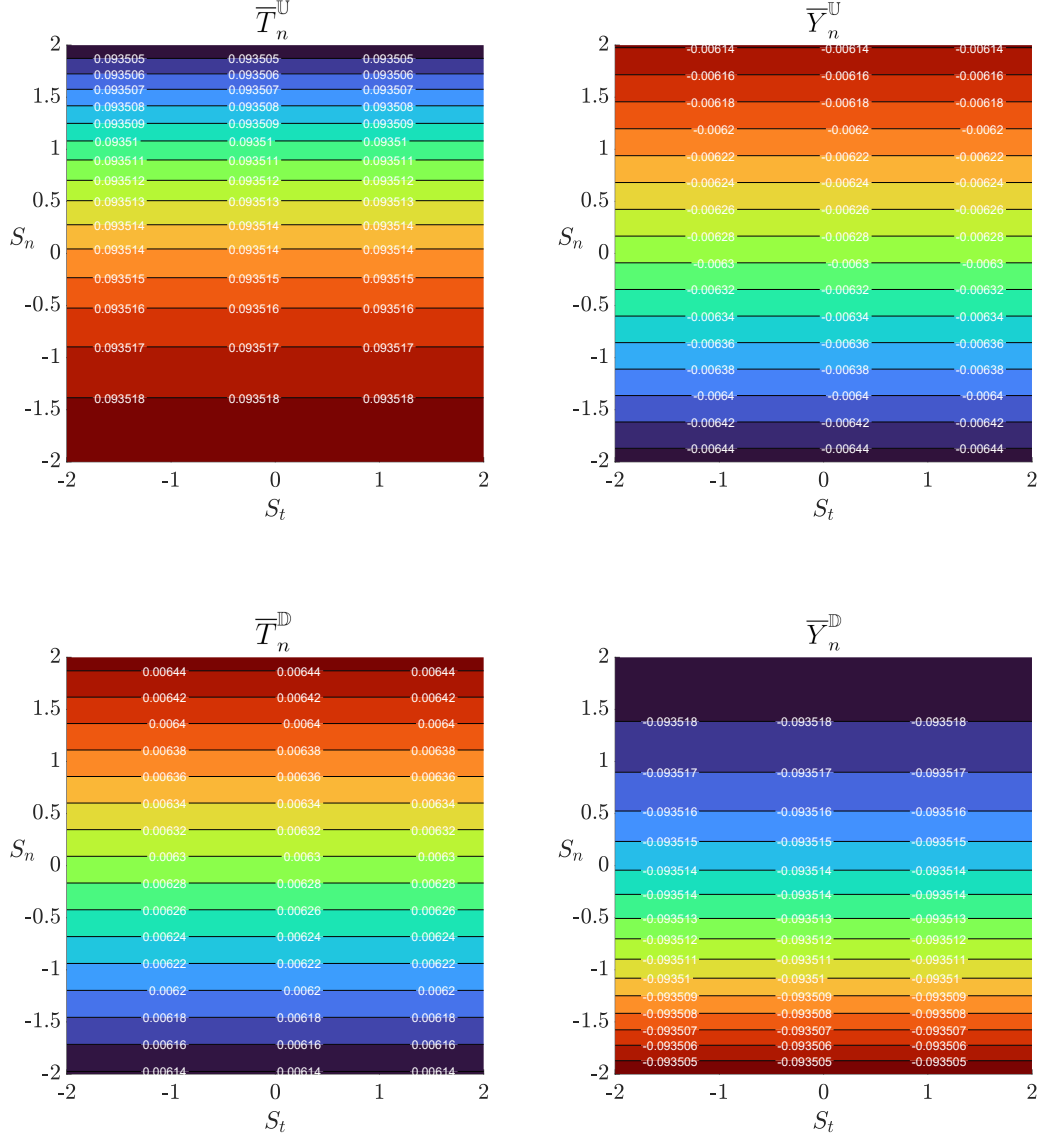


Fig. 4.4: Variations of the upward and downward averages of T_n (left) and Y_n (right) with $(S_t, S_n) \in [-2, 2]$.

Looking at the maps we can correlate \overline{T}_n^U and \overline{Y}_n^D , i.e.

$$\overline{T}_n^U(S_t, S_n) = -\overline{Y}_n^D(-S_t, -S_n). \quad (4.6)$$

4.3 Solution of the Macroscopic Problem

The flow configuration sketched in figure 4.1 is solved in this section.

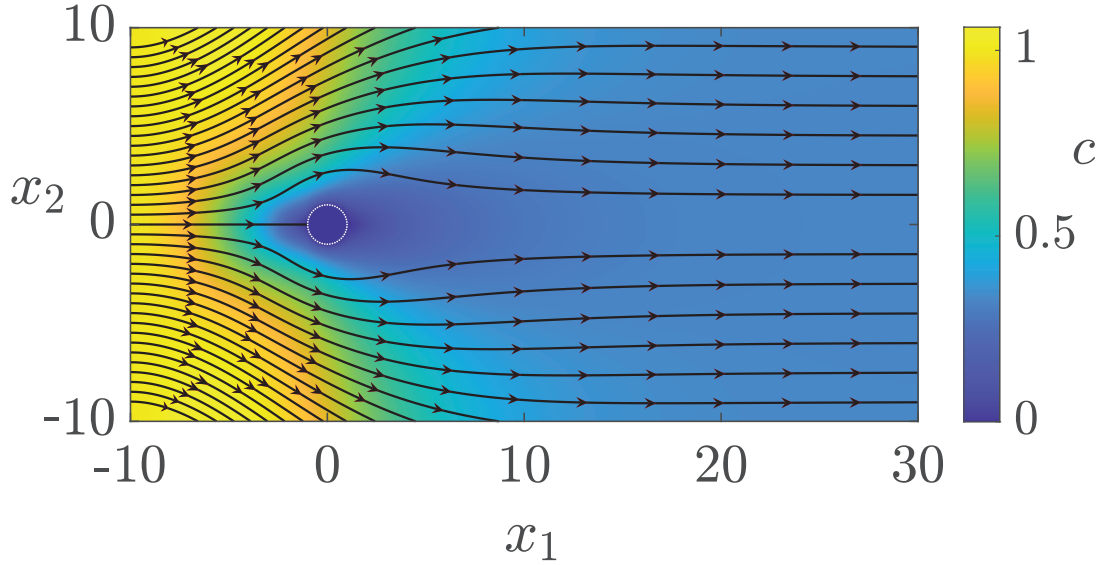


Fig. 4.5: Isocontours of the full-scale concentration c with the flow streamlines (in black).

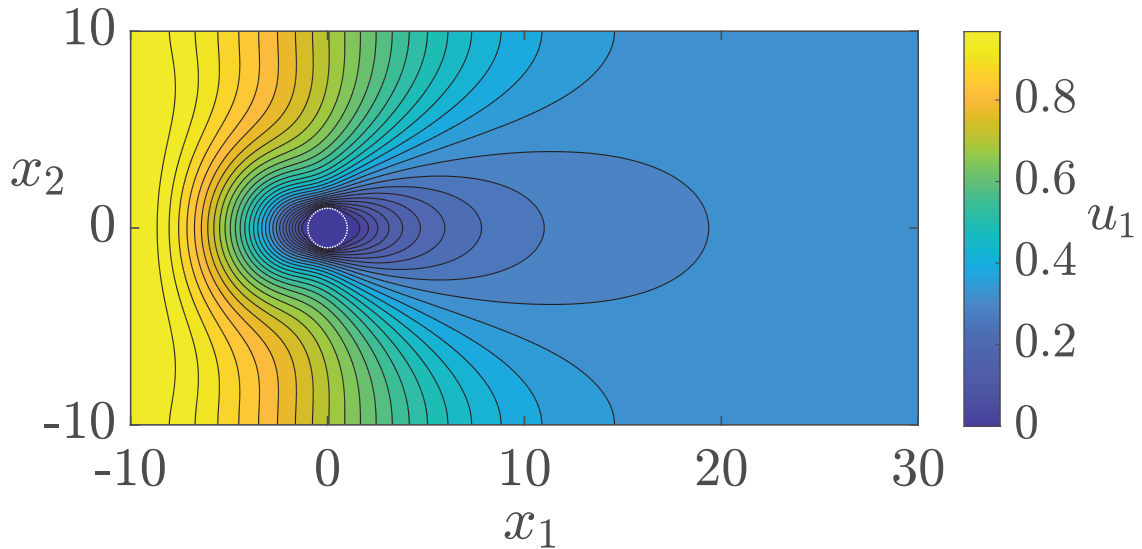


Fig. 4.6: Isocontours of the full-scale horizontal velocity u_1 .

The solution of the macroscopic model is compared with the solution of fully resolved fields. In figure 4.9 the horizontal velocity u_1 and the vertical velocity u_2 are sampled on horizontal and vertical lines passing through the center of the cylindrical membrane.

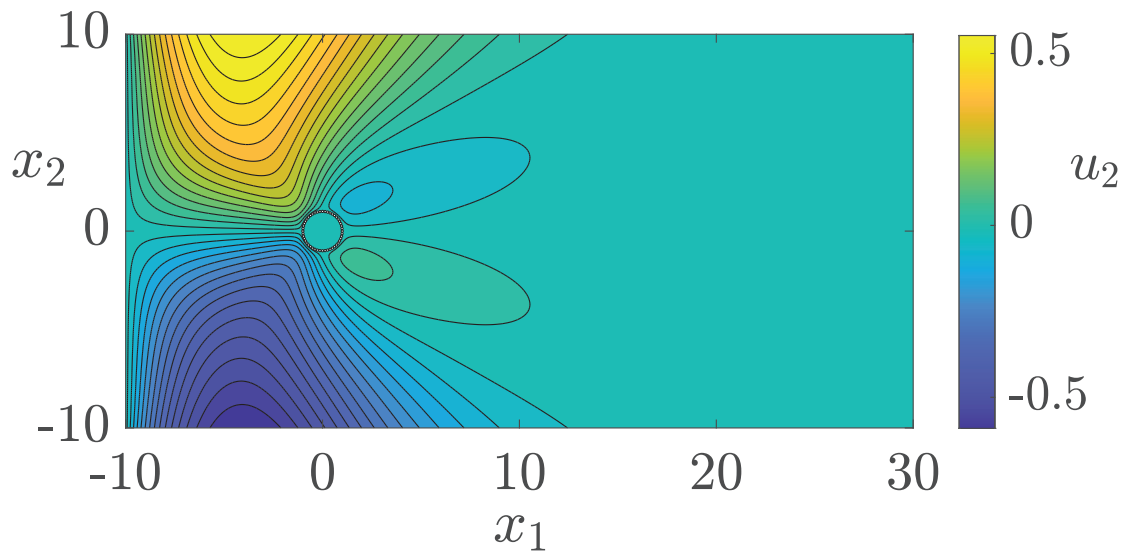


Fig. 4.7: Isocontours of the full-scale vertical velocity u_2 .

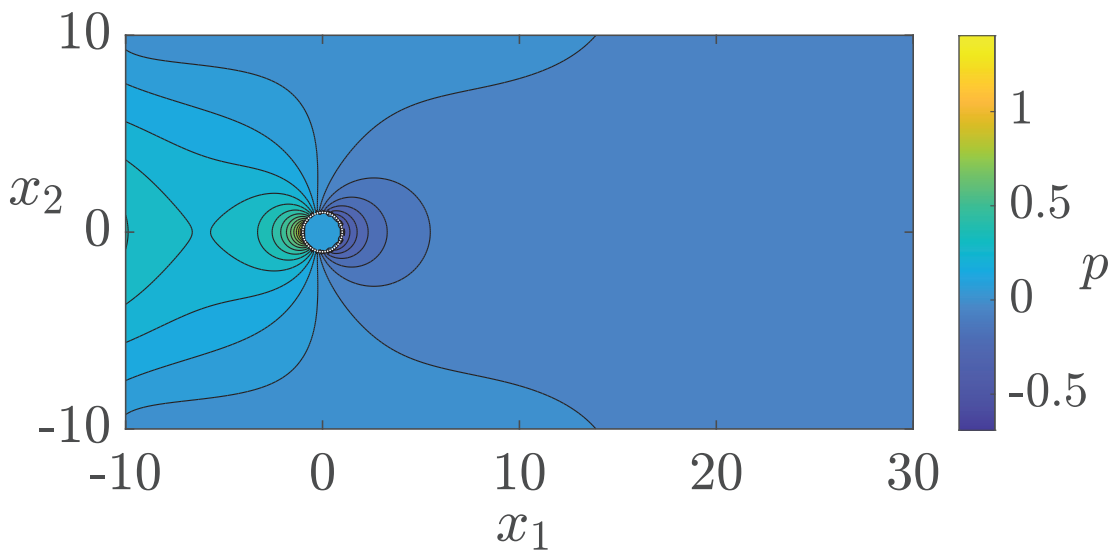


Fig. 4.8: Isocontours of the full-scale pressure p .

The model predicts well the analyzed quantities in the macroscopic domain. In figure 4.10 the pressure p along the horizontal line passing through the center of the cylinder is shown. In figure 4.11 the velocities along the membrane are analyzed. The horizontal axis of figure 4.11 measures the curvilinear coordinate on the cylinder, i.e. $\alpha = \tan^{-1}(y/x)$. The trailing edge of the cylinder corresponds to $\alpha = 0$, while the leading edge to $\alpha = \pi$. We move to the analysis of the concentration c .

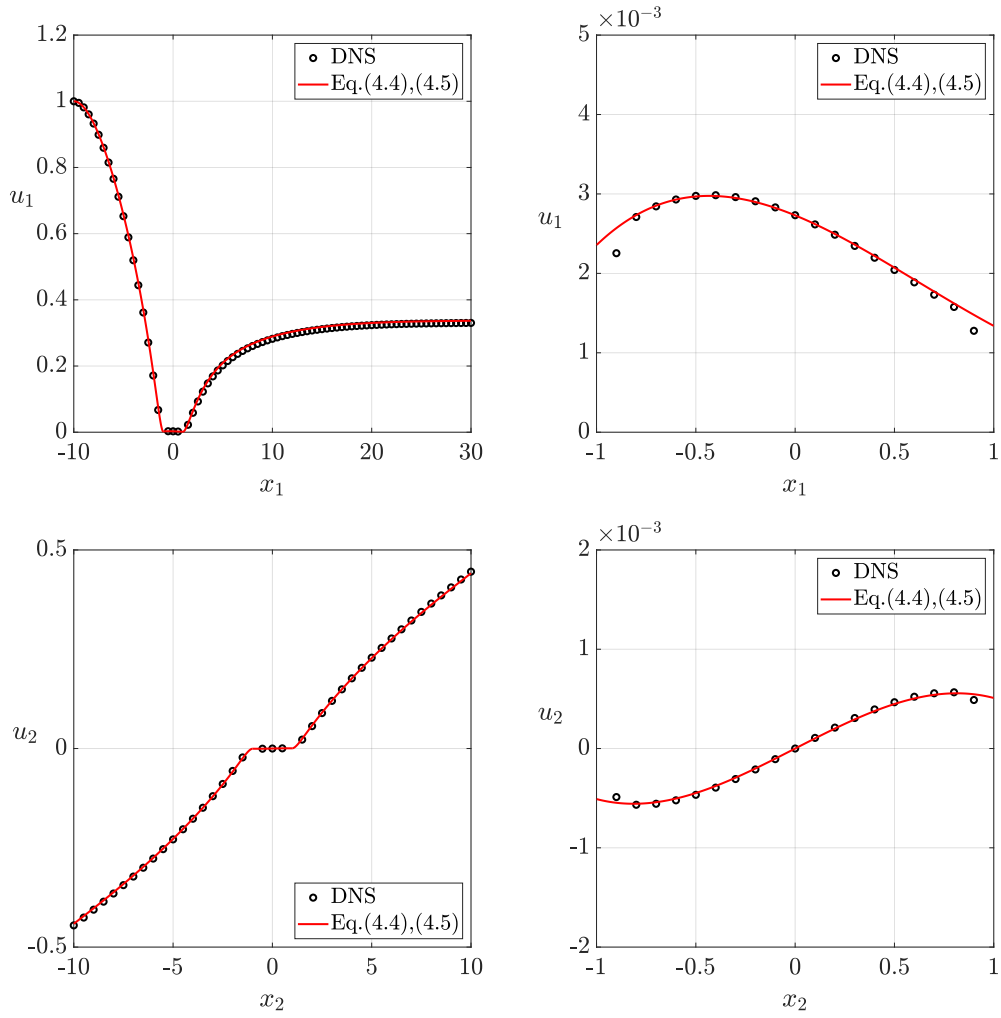


Fig. 4.9: Velocities u_1 (top) and u_2 (bottom) sampled on $x_2 = 0$ (top) and $x_1 = 0$ (bottom). Frames on the right represent a zoom in on the cylindrical membrane diameter.

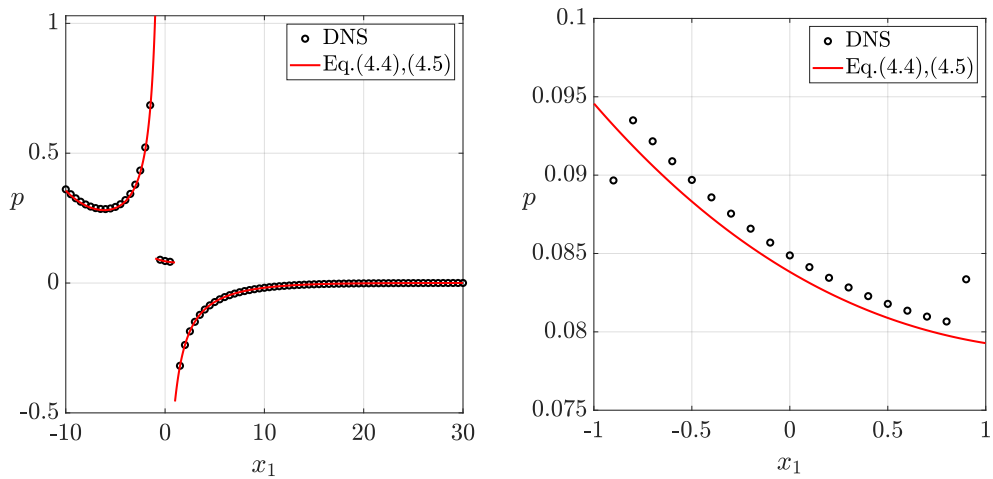


Fig. 4.10: Pressure p over $x_2 = 0$ (left) and zoom in on the cylindrical membrane (right).

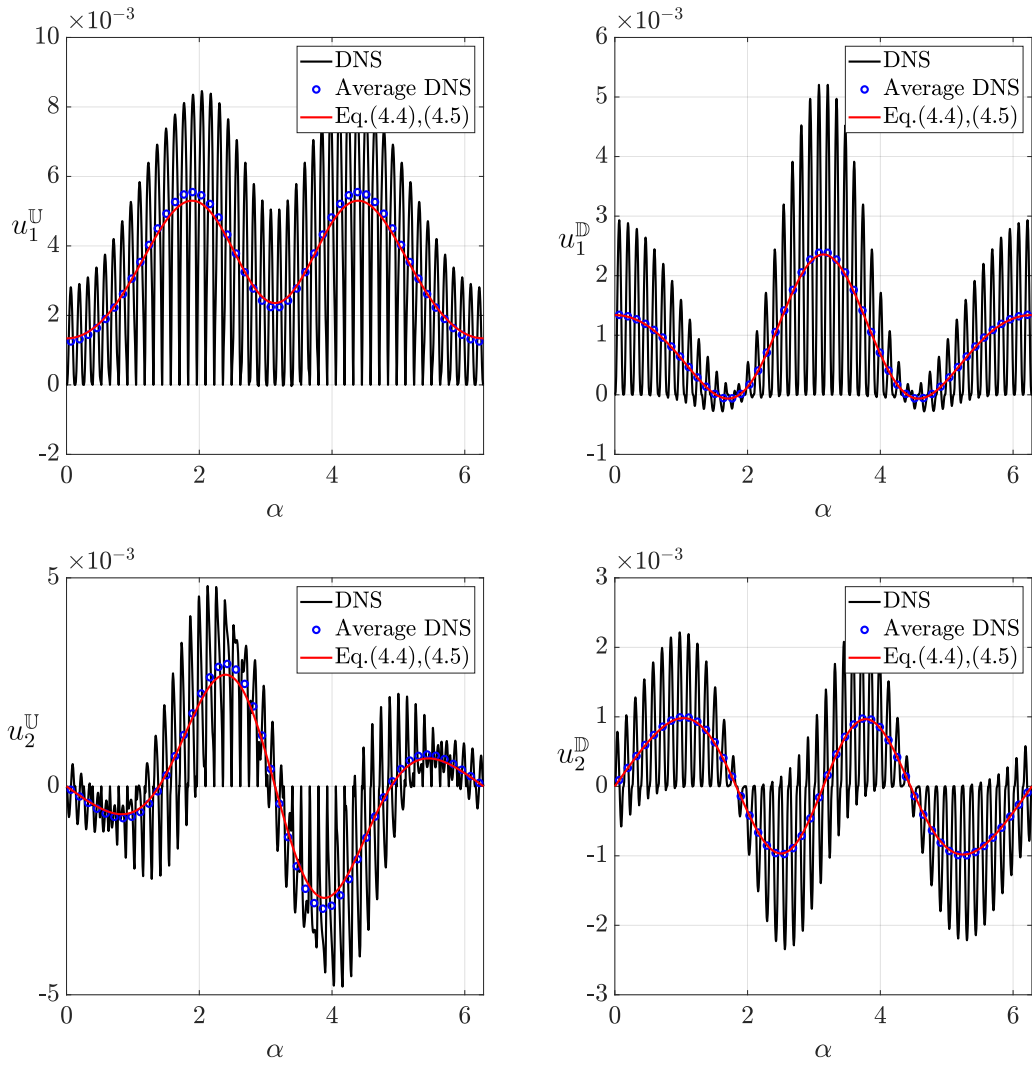


Fig. 4.11: Velocities u_1 (top) and u_2 (bottom) evaluated on the \mathbb{C}^- (left) and \mathbb{C}^+ (right) sides of the membrane.

4.3.1 Diffusive Case

We first analyze the case $Pe^{\mathbb{D}} = 0$. The concentration c on the axis $x_2 = 0$ is shown in figure 4.12, with a closer look in the inner cylinder region.

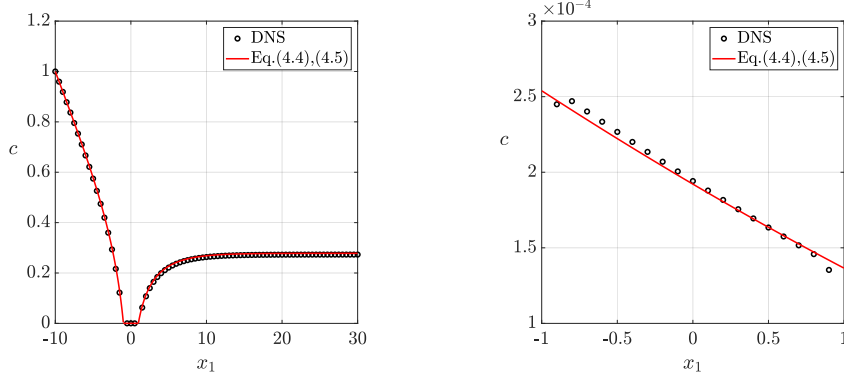


Fig. 4.12: Concentration c sampled on the axis $x_2 = 0$ (left) and zoom in on the membrane (right).

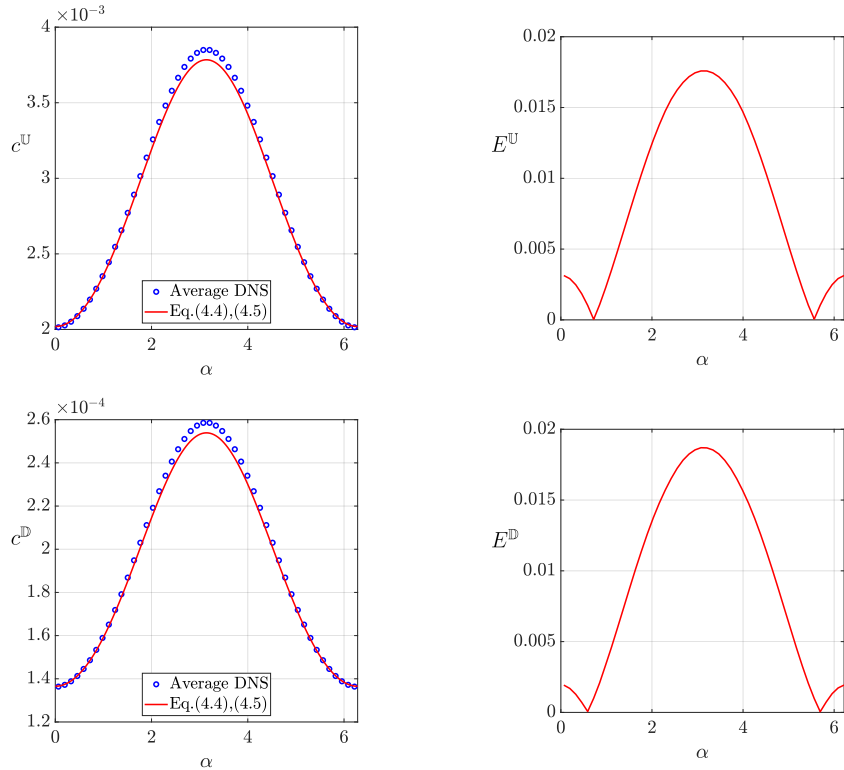


Fig. 4.13: Upward (top) and downward (bottom) concentration c on the membrane (left) and relative error between the macroscopic and full scale solution (right).

The diffusive case is well predicted by the model. We can see that the maximum concentration is at the leading edge of the cylinder, while the minimum on the trailing edge.

4.3.2 Case $Pe^0 = \frac{1}{\varepsilon^2}$

The values of the tensors \mathbf{T} and \mathbf{Y} are obtained using strategy C.

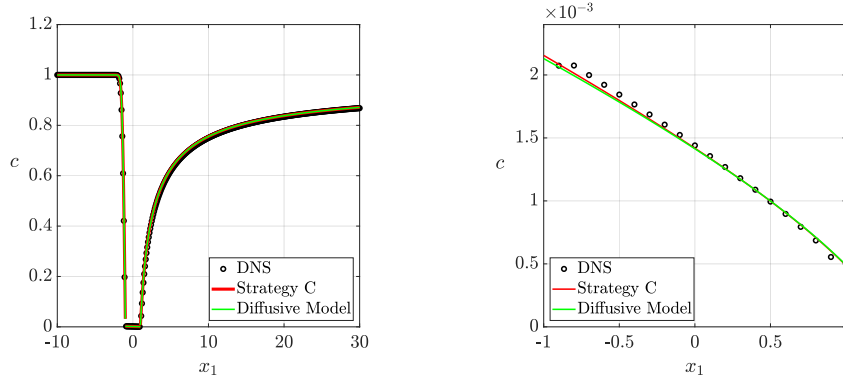


Fig. 4.14: Concentration c sampled on the axis $x_2 = 0$ (left) and zoom in on the membrane (right).

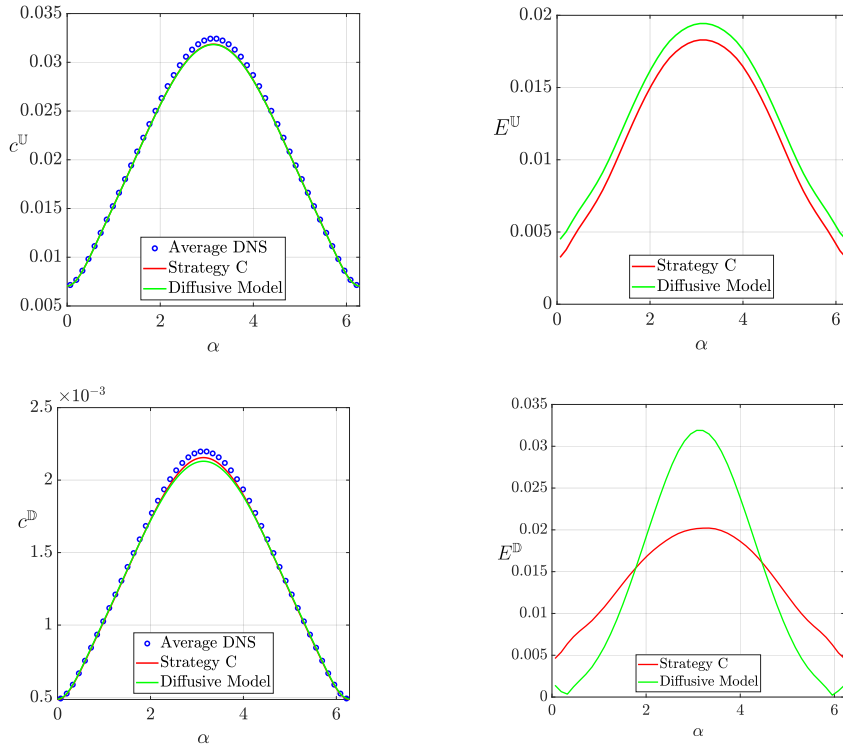


Fig. 4.15: Upward (top) and downward (bottom) concentration c on the membrane (left) and relative error between the macroscopic and full scale solution (right).

The values of $\bar{T}_n^{U,D}$ and $\bar{Y}_n^{U,D}$ obtained along the membrane are similar to those of the diffusive case since Pe^I is small ($Pe^I \approx 0.02$).

4.3.3 Case $Pe^0 = \frac{1}{\varepsilon^3}$

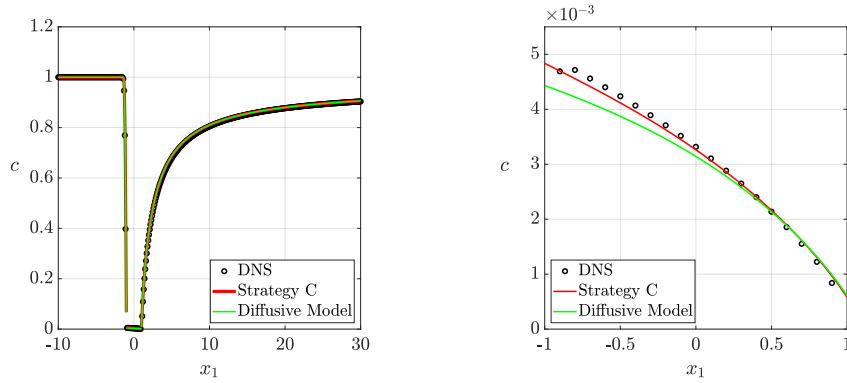


Fig. 4.16: Concentration c sampled on the axis $x_2 = 0$ (left) and zoom in on the membrane (right).

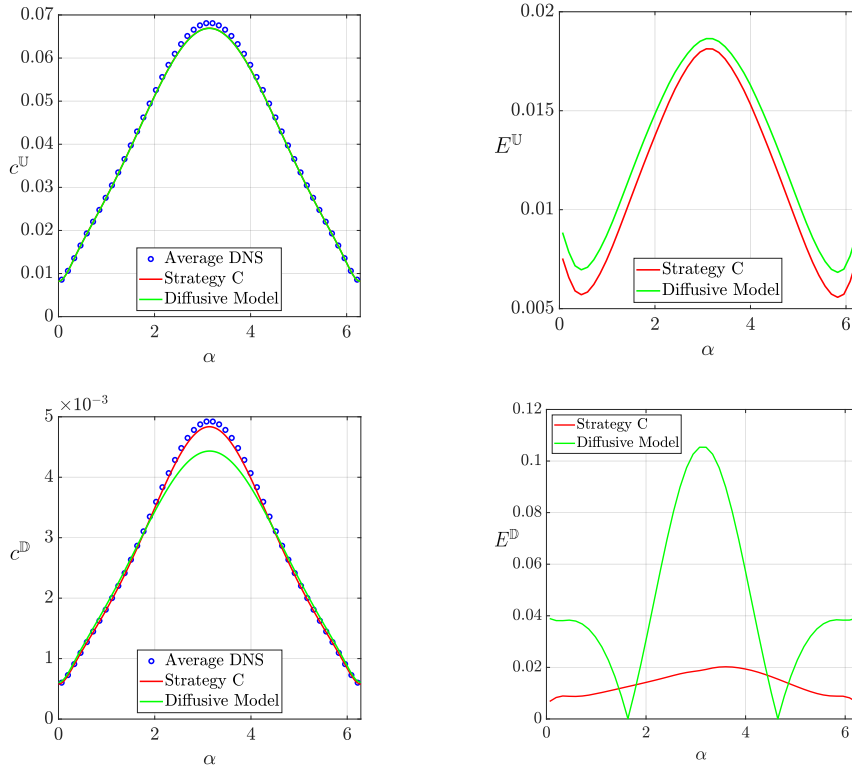


Fig. 4.17: Upward (top) and downward (bottom) concentration c on the membrane (left) and relative error between the macroscopic and full scale solution (right).

A large deviation from the diffusive model on \mathbb{C}^+ is observed, while on \mathbb{C}^- the variations are smaller. Strategy C well predict the solution within the cylinder, while the diffusive case underestimate the solution.

4.3.4 $Pe = 1000$ case

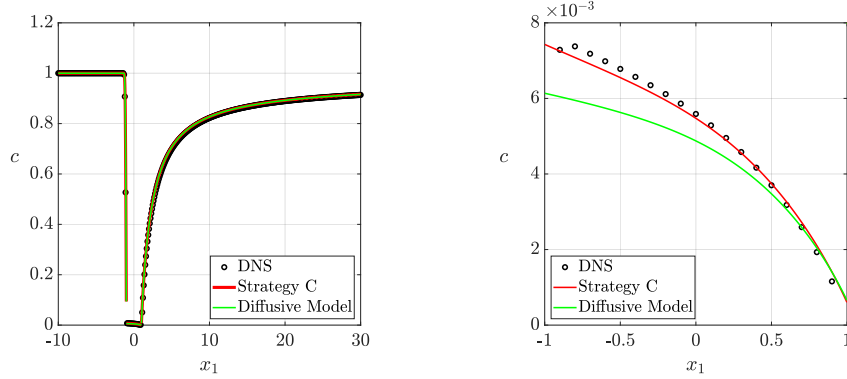


Fig. 4.18: Concentration c sampled on the axis $x_2 = 0$ (left) and zoom in on the membrane (right).

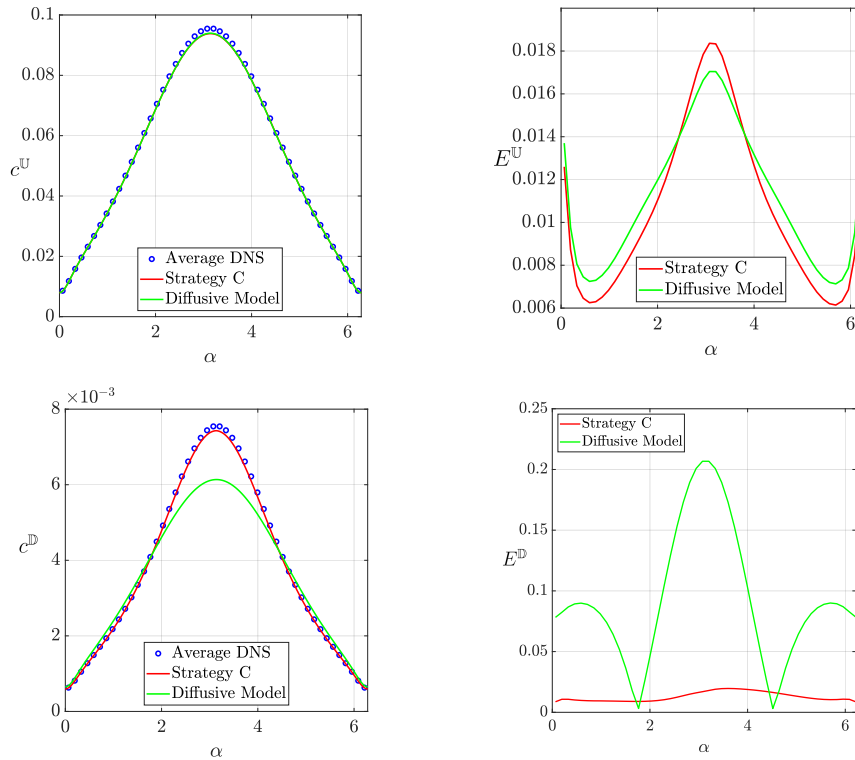


Fig. 4.19: Upward (top) and downward (bottom) concentration c on the membrane (left) and relative error between the macroscopic and full scale solution (right).

The diffusive model fails to predict the concentration inside the cylinder, while strategy C predict well the full-scale solution. The effects of advection on \mathbb{C}^+ are larger than those on \mathbb{C}^- .

4.3.5 Case $Pe^0 = 2000$

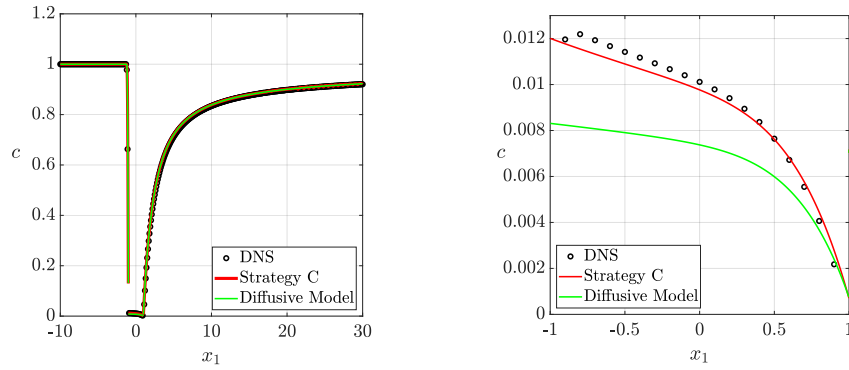


Fig. 4.20: Concentration c sampled on the axis $x_2 = 0$ (left) and zoom in on the membrane (right).

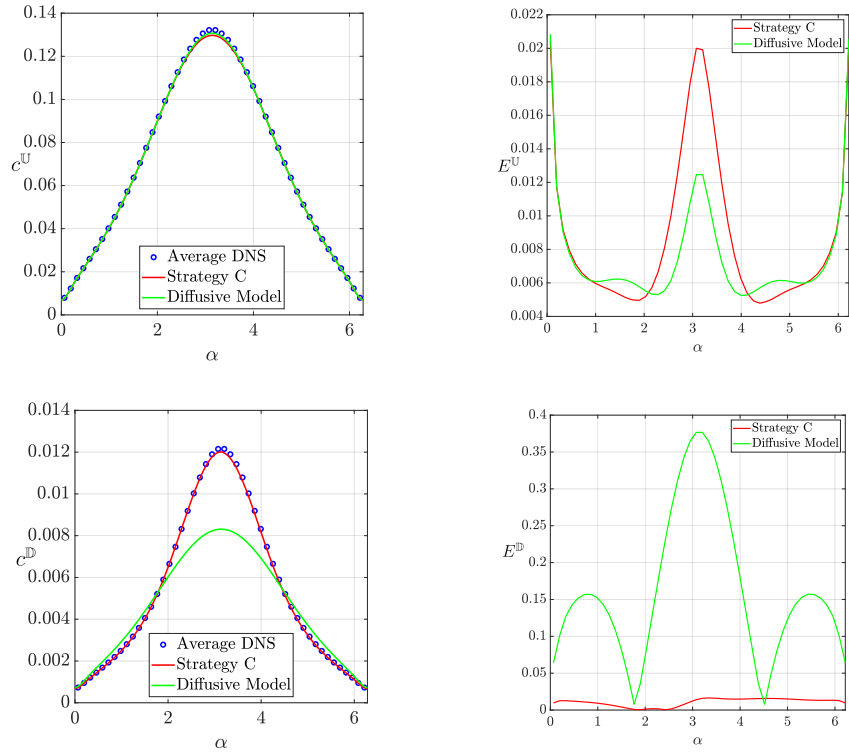


Fig. 4.21: Upward (top) and downward (bottom) concentration c on the membrane (left) and relative error between the macroscopic and full scale solution (right).

The trend described for the previous case is confirmed also for this Péclet number.

4.3.6 Case $Pe^0 = \frac{1}{\varepsilon^4}$

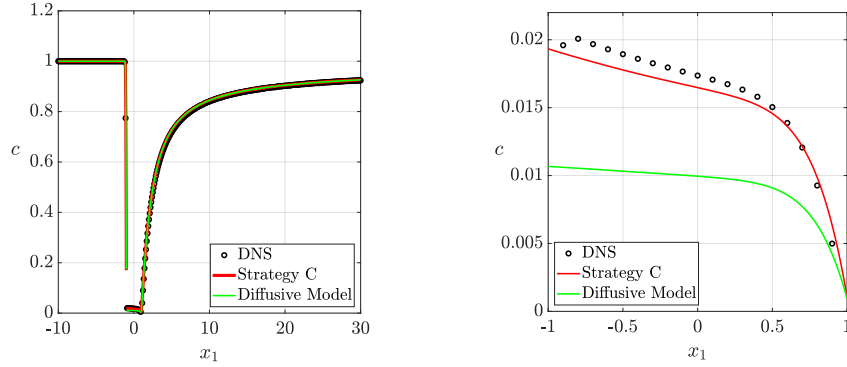


Fig. 4.22: Concentration c sampled on the axis $x_2 = 0$ (left) and zoom in on the membrane (right).

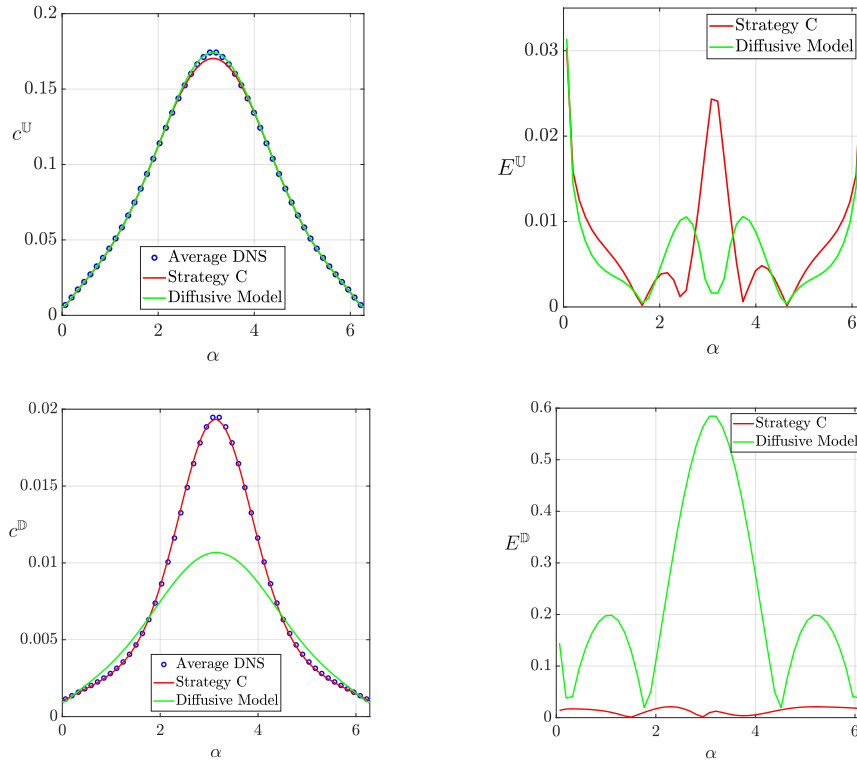


Fig. 4.23: Upward (top) and downward (bottom) concentration c on the membrane (left) and relative error between the macroscopic and full scale solution (right).

This last case shows that even if the error on \mathbb{C}^- is low for all strategies considered, an error higher than 50% is noticed between the diffusive model and the DNS in the inner cylindrical region.

4.3.7 Variations of Pe^{I} with Pe^{O}

In figure 4.24 the local Pe^{I} along the membrane are shown for the Pe^{O} considered in the previous sections.

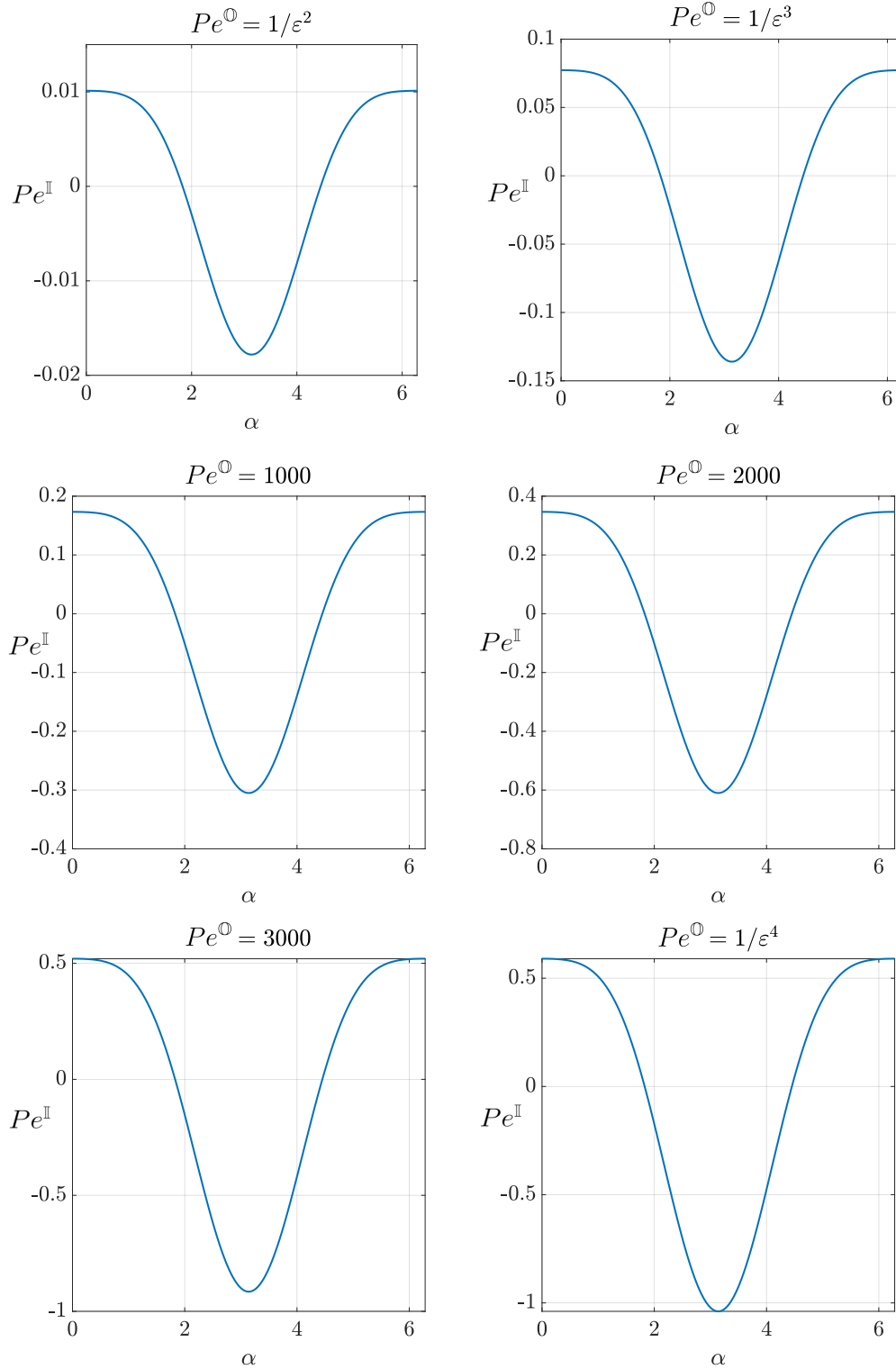


Fig. 4.24: Values of Pe^{I} on the membrane.

5 Conclusions

In this work we developed a macroscopic model for the transport of chemical species diluted in an incompressible Newtonian fluid, at large Péclet numbers. The solute-solvent couple interacts with a thin porous membrane, modeled as an equivalent smooth surface via the macroscopic conditions (2.41), found using a homogenization technique. Equation (2.41) accounts for the microscopic behaviour of the membrane and allows one to correctly predict the averaged full-scale solution. Velocity and concentration are respectively written as the linear combination of the solvent stress tensors and the solute fluxes. The coefficients of the linear combinations mentioned above are obtained from the solution of microscopic problems (2.36) and (2.37). The macroscopic conditions show a jump in the solvent tractions and in the normal-to-the-membrane solute flux.

In the first validation case, the coefficients are averaged on the mean line of the pore, \mathbb{C} , while for the second case on \mathbb{U} and \mathbb{D} . The model is a first order approximation in the separation of scales parameter and its solution is compared to the solution of direct numerical simulations, which solve each length scale present in the problem. The model has a low computational cost allowing a solution faster than that computed via DNS. The model can be used as a tool to design membranes and optimize the transport of mass across them. One could modify the microscopic structure to obtain different values of \mathbf{M} , \mathbf{N} , \mathbf{T} and \mathbf{Y} which satisfy a given objective.

The present work opens several research paths. The macroscopic model is developed assuming that the characteristic size of the pores is much larger than the solute particles diameter. The analysis of comparable pores and particles diameters is still an unresolved issue and can be addressed via the homogenization of multiphase flows [14]. Chemostat-like membranes have been considered in the present work, other kinds of solute-membrane interactions, with partially adsorbing or reactive solid inclusions, deserve an accurate analysis.

The same model should be extended to the case of aperiodic microstructures with three or more characteristic scales, exploiting the strategy developed in [15], and in the case of deformable solid inclusions [16, 17].

The macroscopic condition (2.41) is the leading order approximation in the ε -expansion of the full-scale problem. To increase the precision of the model, the next order approximations need to be computed.

References

- [1] Kaustubha Mohanty and Mihir K Purkait. *Membrane technologies and applications*. CRC press, 2011.
- [2] Menachem Elimelech and William A Phillip. The future of seawater desalination: energy, technology, and the environment. *science*, 333(6043):712–717, 2011.
- [3] Clemens Fritzmann, Jonas Löwenberg, Thomas Wintgens, and Thomas Melin. State-of-the-art of reverse osmosis desalination. *Desalination*, 216(1-3):1–76, 2007.
- [4] Asif Matin, Z Khan, SMJ Zaidi, and MC Boyce. Biofouling in reverse osmosis membranes for seawater desalination: phenomena and prevention. *Desalination*, 281:1–16, 2011.
- [5] Ho Bum Park, Jovan Kamcev, Lloyd M Robeson, Menachem Elimelech, and Benny D Freeman. Maximizing the right stuff: The trade-off between membrane permeability and selectivity. *Science*, 356(6343):eaab0530, 2017.
- [6] David S Sholl and Ryan P Lively. Seven chemical separations to change the world. *Nature*, 532(7600):435–437, 2016.
- [7] Stephen Whitaker. *The method of volume averaging*, volume 13. Springer Science & Business Media, 1998.
- [8] Brian D Wood, Michel Quintard, and Stephen Whitaker. Jump conditions at non-uniform boundaries: the catalytic surface. *Chemical Engineering Science*, 55(22):5231–5245, 2000.
- [9] Ulrich Hornung. *Homogenization and porous media*, volume 6. Springer Science & Business Media, 1996.
- [10] Chiang C Mei and Bogdan Vernescu. *Homogenization methods for multiscale mechanics*. World scientific, 2010.
- [11] Giuseppe A Zampogna, Pier G Ledda, and François Gallaire. Transport across thin membranes: Effective solute flux jump. *Physics of Fluids*, 34(8):083113, 2022.
- [12] Abraham D Stroock, Stephan KW Dertinger, Armand Ajdari, Igor Mezic, Howard A Stone, and George M Whitesides. Chaotic mixer for microchannels. *Science*, 295(5555):647–651, 2002.
- [13] Giacomo Falcucci, Giorgio Amati, Pierluigi Fanelli, Vesselin K Krastev, Giovanni Polverino, Maurizio Porfiri, and Sauro Succi. Extreme flow simulations reveal skeletal adaptations of deep-sea sponges. *Nature*, 595(7868):537–541, 2021.

- [14] Davide Picchi and Ilenia Battiato. The impact of pore-scale flow regimes on up-scaling of immiscible two-phase flow in porous media. *Water resources research*, 54(9):6683–6707, 2018.
- [15] Svyatoslav Korneev and Ilenia Battiato. Sequential homogenization of reactive transport in polydisperse porous media. *Multiscale Modeling & Simulation*, 14(4):1301–1318, 2016.
- [16] Giuseppe A Zampogna, Ugis Lācis, Shervin Bagheri, and Alessandro Bottaro. Modeling waves in fluids flowing over and through poroelastic media. *International Journal of Multiphase Flow*, 110:148–164, 2019.
- [17] Andro Mikelić and Mary F Wheeler. Theory of the dynamic biot-allard equations and their link to the quasi-static biot system. *Journal of mathematical physics*, 53(12):123702, 2012.
- [18] Giuseppe A Zampogna and François Gallaire. Effective stress jump across membranes. *Journal of Fluid Mechanics*, 892:A9, 2020.
- [19] Giuseppe A Zampogna, Kevin Wittkowski, Pier G Ledda, and François Gallaire. Homogenization theory captures macroscopic flow discontinuities across janus membranes. *Journal of Fluid Mechanics*, Under review.
- [20] Pier G Ledda, Edouard Boujo, Simone Camarri, François Gallaire, and Giuseppe A Zampogna. Homogenization-based design of microstructured membranes: wake flows past permeable shells. *Journal of Fluid Mechanics*, 927:A31, 2021.
- [21] Alfio Quarteroni and Alberto Valli. *Domain decomposition methods for partial differential equations*. Oxford University Press, 1999.

A Numerical solution

The governing equations are spatially discretized using the finite element method implemented in the software COMSOL Multiphysics™. This software enables fast implementation of the weak form of the governing equations,

$$\begin{cases} \int_{\mathbb{F}} q \nabla \cdot \mathbf{u} dV = 0 \\ \int_{\mathbb{F}} (\mu \nabla \mathbf{u} \cdot \nabla \mathbf{v} + \rho (\mathbf{u} \cdot \nabla) \mathbf{u} \cdot \mathbf{v} - p \nabla \cdot \mathbf{v}) dV + B.T = 0 \\ \int_{\mathbb{F}} (\mathbf{u} \nabla c w + \nabla w \nabla c) dV + B.T = 0, \end{cases} \quad (\text{A.1})$$

where q, \mathbf{v} and w are test functions and $B.T.$ denotes the boundary terms, which are evaluated using the boundary conditions specified case by case.

The pressure field is discretized using first-order Lagrangian polynomials, while the concentration and the velocity fields are discretized with second-order Lagrangian polynomials. The domain decomposition method [21] is used to solve the equivalent macroscopic problem: the Navier-Stokes and advection-diffusion equations are solved within the two subdomains and coupled using the stress and concentration flux jump conditions (2.41) and continuity of velocities on the fictitious interface \mathbb{C} .

B Numerical convergence

In figure B.1 the convergence of the averaged tensors with the cell size is shown. Only the upward averages are shown since $M_{nnn} = -N_{nnn}$, $M_{ttn} = -N_{ttn}$ and $T_n = -Y_n$. We define a variable k that denotes the dimension of the computational grid. The fluid domain is discretized with a mesh of triangular cells (cf. figure B.3). The denser the mesh, the more accurate the solution is. For a coarse mesh we have huge variations in the values of the tensors, while for a finer one the results converge. The chosen value of k is identified by a red dot in figure B.1.

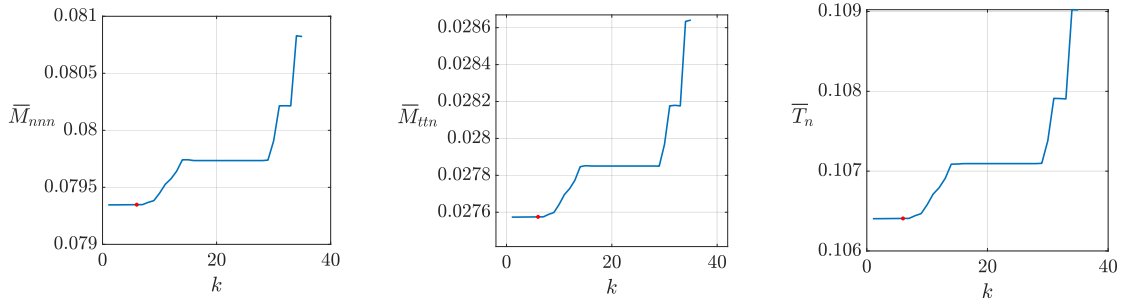


Fig. B.1: Non-zero averaged tensors as a function of k . The red points denote the parameters chosen for the calculations.

In figure B.2 the variations of the same tensors components with the height of the microscopic domain l are evaluated. For large values of this parameter the tensors components reach an asymptotic value. As for the previous case, we set a given

value of l to carry out all microscopic solutions (denoted by red points in figure B.2).

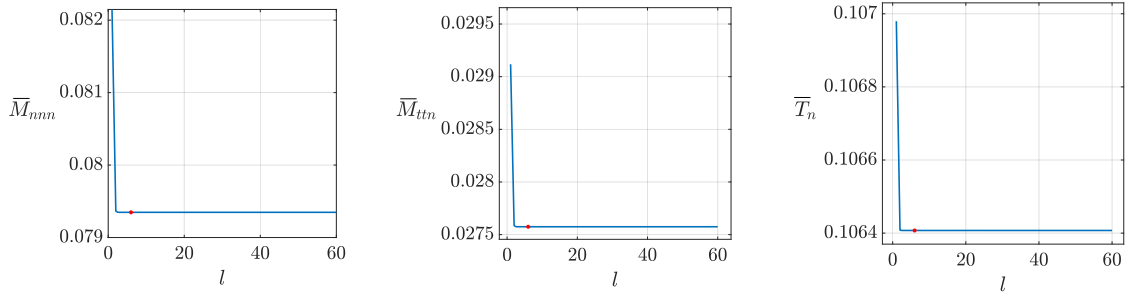


Fig. B.2: Non-zero averaged tensors as a function of l . The red points denote the parameters chosen for the calculations.

For a better understanding on how the two parameters k and l affect the computational domain, a sketch is shown in figure B.3.

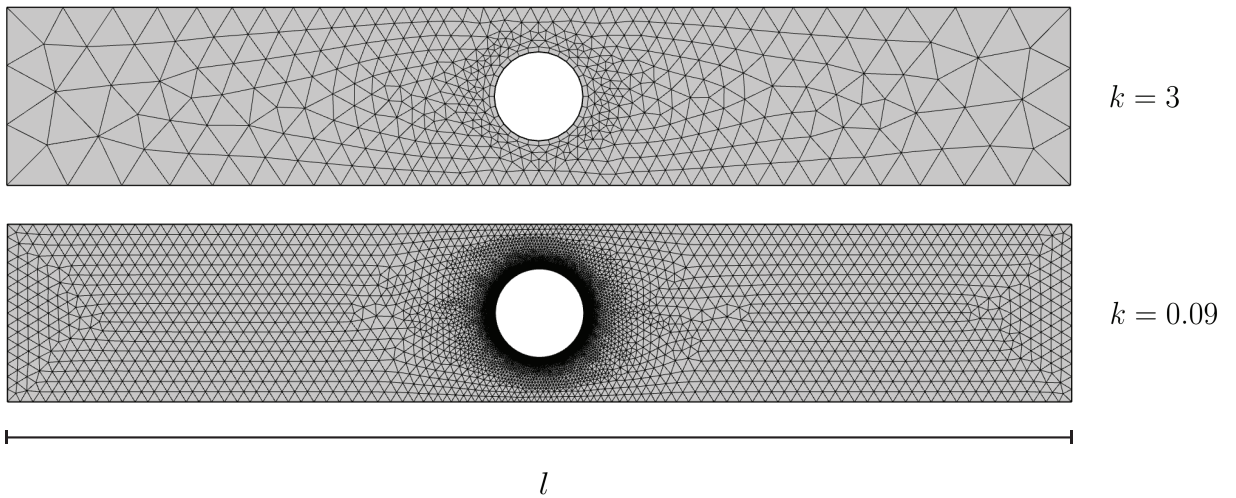


Fig. B.3: Top frame: sketch of the mesh for $k = 3$ Bottom frame: sketch of the mesh for $k = 0.09$.